A TWO-DIAMETER TIMOSHENKO BEAM MODEL FOR HELICAL ENDMILL DYNAMICS PREDICTION WITH APPLICATION TO MILLING

A Dissertation Presented for the

Doctor of Philosophy

Degree

The University of Tennessee, Knoxville

Emma DellaMarie Betters

December 2023

DEDICATION

For Pop.

ACKNOWLEDGEMENTS

First, I would like to thank Dr. Tony Schmitz for his guidance, compassion, tough love (as needed), and, most importantly, patience over the past six years. I am incredibly grateful for the opportunities you have provided for me to learn and build my "toolbox", for constantly challenging me to improve, and for the excellent example of work ethic and curiosity you have set.

Justin West, thank you for going on this adventure with me and reminding me to breathe along the way. I wouldn't have wanted to do this without you.

Mr. Nobrega, you sparked a career with the suggestion that engineering might be a way for me to play for the rest of my life. I can't imagine doing anything else.

Mike Braddock, you shared a passion for design and manufacturing with me. I hope this is a gift I can continue to share with others.

Dr. Scott Smith and Dr. Chris Tyler, I appreciate your continuous support and encouragement.

Sammie, there are few things that motivate more than sibling competition. Thank you for always pushing me to keep up.

Finally, to Mom and Dad, thank you for believing I could do anything and giving me the skills to act on that belief.

I would also like to acknowledge support from Oak Ridge National Laboratory's Manufacturing Demonstration Facility and from the Industrial Base Analysis and Sustainment Program.

ABSTRACT

The aim of this dissertation is to describe the dynamic response of helical endmill geometries to enable the use of receptance coupling substructure analysis (RCSA) for predicting the tool tip vibration response of arbitrary tool-holder-spindle-machine combinations. The tool tip vibration response, or receptance, is a key input for milling stability prediction. Currently, a measurement is required to determine the tool tip receptance for each tool-holder-spindle-machine combination, which may not be possible in production environments. In the RCSA approach, the spindle receptances are measured once and archived, while the tool and holder are modeled. Tool tip receptances are predicted by analytically coupling the tool and holder models, described as equivalent diameter Timoshenko beams, to the archived spindle receptances. In this study, a two-diameter Timoshenko beam model derived, tested, and applied to predict the dynamic response of the fluted portion of the endmill geometry.

TABLE OF CONTENTS

LIST OF TABLES

LIST OF FIGURES

CHAPTER ONE
INTRODUCTION

In milling operations, the pre-process selection of spindle speed-depth of cut combinations which produce stable cutting conditions can be the difference between a profit and a loss in production environments. The pre-process (before making a cut) prediction of stable parameters has received significant attention in the research community. Three common methods used to determine the stability boundary, which separates stable and unstable spindle speed-depth of cut combinations, are: average force method (Tlusty method) [1], Fourier series method (Altintas method) [2], and time domain simulation [3]. The predicted stability boundary varies slightly for each of these models and each offers advantages and disadvantages in different use cases. However, all three predictive methods require knowledge of the tool tip frequency response function (FRF), or receptance.

Traditionally, impact testing is performed using an instrumented hammer and linear transducer (e.g., accelerometer, vibrometer, or capacitance gauge) to measure the tool tip FRF for a specified tool-holder-spindle-machine assembly [3]. The measured FRF is then used to generate a stability map, a diagram that separates spindle speed-axial depth of cut combinations that provide stable machining conditions from those that exhibit chatter, or unstable behavior, for a given radial immersion. The effectiveness of on-machine FRF measurements has been widely demonstrated in the literature and industry. However, each stability map is unique to a specific tool-holder-spindle-machine assembly with the tool inserted in the holder at a given extension length, or stickout length, from the holder [4]–[6]. This assembly-specific relationship makes the collection of the required data expensive and time consuming. Due to the required capital and time investment, many machining facilities rely on prior experience or iterate through combinations when selecting spindle speed-axial depth combinations. This can result in scrapped parts, underutilization of machine capability, and non-optimal cycle times.

The objective of this project is to enable the selection of stable machining parameters without the need for individual measurements of each tool-holder-spindle-machine assembly. Receptance coupling substructure analysis (RCSA) is used to predict the tool tip receptance [7]. Using this approach, a single on-machine artifact measurement is required for each spindle-machine. Inverse receptance coupling is used to isolate the spindle-machine receptances from the artifact-spindle-machine measurement. The resulting spindle-machine receptances can then be coupled to an arbitrary tool and holder model to predict the tool-holder-spindle-machine receptances. Holder models are typically axisymmetric and can be modeled as a series of cylindrical Timoshenko beam elements. The fluted section of the tool is more complicated, however. It has widely been described in the literature by a (single) equivalent diameter beam based on different cross-sectional properties of the tool with varying degrees of success.

This research introduces a new two-diameter equivalent Timoshenko beam model to more accurately predict the dynamic response of the helical, or fluted, portion of the endmill. This model incorporates both mass and stiffness considerations in the Timoshenko beam model based on both the endmill cross-section and helix angle. The proposed solution provides a computationally inexpensive method for the prediction of the tool tip frequency response.

CHAPTER TWO
LITERATURE REVIEW

Tool tip receptance is a key input to milling stability analyses in which stable and unstable combinations of spindle speed and axial depth of cut are predicted to avoid their trial-and-error selection [2], [3], [8], [9]. Typically, a measurement is required for each tool-holder-spindle-machine combination [3]. In facilities with many machines, limited FRF measurement capability, or lack of time and capital, this tool-holder-spindle-machine specific measurement hinders the ability to use stability maps for optimized parameter selection.

Receptance coupling is a technique where component/substructure receptances, or frequency response functions (FRFs), are joined analytically to predict assembly dynamics. It was first introduced in 1960 by Bishop and Johnson [10] and has become a standard tool in structural dynamics modeling. Schmitz and Donaldson first pioneered the use of receptance coupling substructure analysis (RCSA) in 2000 for the prediction of tool tip frequency response functions in milling [7]. This method provided a shift from on-machine measurements to a modeling-based approach for the determination of tool tip receptances.

In the following sections, key elements of the RCSA procedure and algorithm are first described [7]. Next, various modeling approaches are presented. Finally, prior work regarding the dynamic modeling of twisted beams is presented. A comprehensive review of the literature surrounding the prediction of the tool tip frequency response function using receptance coupling is provided in [11] and summarized here.

Receptance Coupling Substructure Analysis

The RCSA model includes: 1) transverse deflections, x_i and X_i, for the components (lower case variables) and assembly (upper case variables) due to internal and external forces, f_j

and F_j; and 2) rotations about lines perpendicular to the beam axis, θ_i and Θ_i, and bending moments (or couples), m_j and M_j, to completely define the transverse dynamic behavior of beams. To describe the procedure, consider the cylinder-prismatic cantilever beam assembly displayed in Figure 2-1. This is representative of a tool (shown as a cylinder) rigidly attached to a holder-spindle-machine (shown as a prismatic cantilever beam).

To calculate the assembly receptances, all four bending receptances are included in the component (i.e., cylinder and prismatic cantilever beam) descriptions. These four bending receptances include displacement-to-force, h_{ij}, displacement-to-couple, l_{ij}, rotation-to-force, n_{ij}, and rotation-to-couple, p_{ij}, where i is the displacement/rotation coordinate location and j is the location where the force/couple is applied. There are three primary steps followed to predict the Figure 2-1 assembly receptances.

1. Define the components and coordinates for the model. In this example, there are two components: a prismatic beam with fixed-free (or cantilever) boundary conditions and a cylinder with free-free (or unsupported) boundary conditions; see Figure 2-2.
2. Determine the component receptances. These can be based on measurements or models. For the models, an analytical choice is closed-form receptances for flexural vibrations of uniform Euler-Bernoulli beams with free, fixed, sliding, and pinned boundary conditions [10], [12]. A numerical option is the Timoshenko beam model [13]. For measurements, tap testing may be applied, where the structure is excited using a modal hammer (impact force) or shaker-stinger combination (sinusoidal, chirp, or other force profile) and the response is measured using a linear transducer, such as a low-mass accelerometer [12].
3. Based on the model from step 1, express the assembly receptances as a function of the component receptances from step 2. Determine the assembly receptances using the component displacements/rotations, compatibility conditions, and equilibrium conditions.

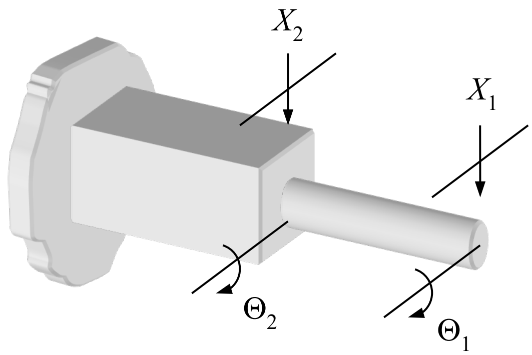

Figure 2-1. RCSA example for a cylinder rigidly coupled to a prismatic cantilever beam to form an assembly.

4.

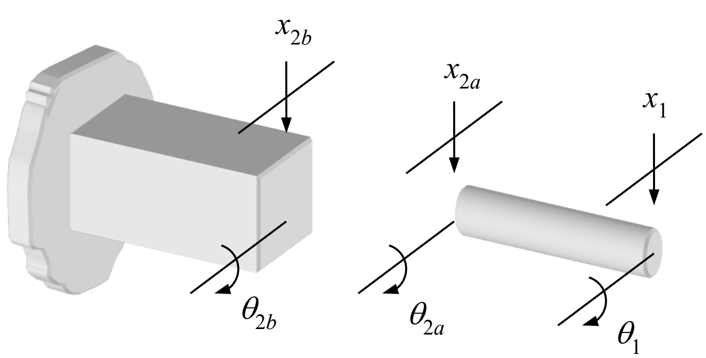

Figure 2-2. Cylinder and prismatic cantilever beam components for RCSA example.

The procedure for coupling the components in Figure 2-2 to form the assembly in Figure 2-1 requires the component receptances. In Figure 2-2, coordinates are placed at the prediction location (1) and coupling locations (2*a* and 2*b*) on the two components. For the cylinder, the direct receptances at the coordinate 1 end are shown in Eq. 2.1.

$$h_{11} = \frac{x_1}{f_1} \qquad l_{11} = \frac{x_1}{m_1} \qquad n_{11} = \frac{\theta_1}{f_1} \qquad p_{11} = \frac{\theta_1}{m_1} \tag{2.1}$$

The cross receptances are given by Eq. 2.2.

$$h_{12a} = \frac{x_1}{f_{2a}} \qquad l_{12a} = \frac{x_1}{m_{2a}} \qquad n_{12a} = \frac{\theta_1}{f_{2a}} \qquad p_{12a} = \frac{\theta_1}{m_{2a}} \tag{2.2}$$

At coordinate 2*a* on the cylinder, the direct and cross receptances are provided in Eqs. 2.3 and 2.4.

$$h_{2a2a} = \frac{x_{2a}}{f_{2a}} \quad l_{2a2a} = \frac{x_{2a}}{m_{2a}} \quad n_{2a2a} = \frac{\theta_{2a}}{f_{2a}} \quad p_{2a2a} = \frac{\theta_{2a}}{m_{2a}} \tag{2.3}$$

$$h_{2a1} = \frac{x_{2a}}{f_1} \qquad l_{2a1} = \frac{x_{2a}}{m_1} \qquad n_{2a1} = \frac{\theta_{2a}}{f_1} \qquad p_{2a1} = \frac{\theta_{2a}}{m_1} \tag{2.4}$$

Similarly, for the prismatic cantilever beam, the direct receptances at the coupling location 2*b* are given by Eq. 2.5.

$$h_{2b2b} = \frac{x_{2b}}{f_{2b}} \quad l_{2b2b} = \frac{x_{2b}}{m_{2b}} \quad n_{2b2b} = \frac{\theta_{2b}}{f_{2b}} \quad p_{2b2b} = \frac{\theta_{2b}}{m_{2b}} \tag{2.5}$$

To simplify notation, the component receptances may be represented in matrix form as shown in Eqs. 2.6 through 2.9 for the cylinder and Eq. 10 for the prismatic cantilever beam. In Eqs. 2.6-2.10 R_{ij} is the generalized receptance matrix that describes both translational and rotational component behavior [14] and u_i and q_j are the corresponding generalized displacement/rotation and force/couple vectors.

$$\begin{Bmatrix} x_1 \\ \theta_1 \end{Bmatrix} = \begin{bmatrix} h_{11} & l_{11} \\ n_{11} & p_{11} \end{bmatrix} \begin{Bmatrix} f_1 \\ m_1 \end{Bmatrix} \text{ or } \{\boldsymbol{u_1}\} = [\boldsymbol{R_{11}}]\{\boldsymbol{q_1}\} \tag{2.6}$$

$$\begin{Bmatrix} x_{2a} \\ \theta_{2a} \end{Bmatrix} = \begin{bmatrix} h_{2a2a} & l_{2a2a} \\ n_{2a2a} & p_{2a2a} \end{bmatrix} \begin{Bmatrix} f_{2a} \\ m_{2a} \end{Bmatrix} \text{ or } \{\boldsymbol{u_{2a}}\} = [\boldsymbol{R_{2a2a}}]\{\boldsymbol{q_{2a}}\} \tag{2.7}$$

$$\begin{Bmatrix} x_1 \\ \theta_1 \end{Bmatrix} = \begin{bmatrix} h_{12a} & l_{12a} \\ n_{12a} & p_{12a} \end{bmatrix} \begin{Bmatrix} f_{2a} \\ m_{2a} \end{Bmatrix} \text{ or } \{\boldsymbol{u_1}\} = [\boldsymbol{R_{12a}}]\{\boldsymbol{q_{2a}}\} \tag{2.8}$$

$$\begin{Bmatrix} x_{2a} \\ \theta_{2a} \end{Bmatrix} = \begin{bmatrix} h_{2a1} & l_{2a1} \\ n_{2a1} & p_{2a1} \end{bmatrix} \begin{Bmatrix} f_1 \\ m_1 \end{Bmatrix} \text{ or } \{\boldsymbol{u_{2a}}\} = [\boldsymbol{R_{2a1}}]\{\boldsymbol{q_1}\} \tag{2.9}$$

$$\begin{Bmatrix} x_{2b} \\ \theta_{2b} \end{Bmatrix} = \begin{bmatrix} h_{2b2b} & l_{2b2b} \\ n_{2b2b} & p_{2b2b} \end{bmatrix} \begin{Bmatrix} f_{2b} \\ m_{2b} \end{Bmatrix} \text{ or } \{\boldsymbol{u_{2b}}\} = [\boldsymbol{R_{2b2b}}]\{\boldsymbol{q_{2b}}\} \tag{2.10}$$

The component receptances are written using the generalized notation: $\boldsymbol{u_1} = \boldsymbol{R_{11}q_1} + \boldsymbol{R_{12a}q_{2a}}$ and $\boldsymbol{u_{2a}} = \boldsymbol{R_{2a1}q_1} + \boldsymbol{R_{2a2a}q_{2a}}$ for the cylinder and $\boldsymbol{u_{2b}} = \boldsymbol{R_{2b2b}q_{2b}}$ for the prismatic cantilever beam. For a rigid connection between the two components, the compatibility condition is $\boldsymbol{u_{2b}} - \boldsymbol{u_{2a}} = 0$. This indicates there is no relative motion at the coupling location. Additionally, if the component and assembly coordinates are at the same physical locations, then $\boldsymbol{u_1} = \boldsymbol{U_1}$ and $\boldsymbol{u_{2a}} = \boldsymbol{u_{2b}} = \boldsymbol{U_2}$ (due to the rigid coupling). The assembly receptances are written as shown in Eq. 2.11, which again incorporates the generalized notation.

$$\begin{Bmatrix} \boldsymbol{U_1} \\ \boldsymbol{U_2} \end{Bmatrix} = \begin{bmatrix} \boldsymbol{G_{11}} & \boldsymbol{G_{12}} \\ \boldsymbol{G_{21}} & \boldsymbol{G_{22}} \end{bmatrix} \begin{Bmatrix} \boldsymbol{Q_1} \\ \boldsymbol{Q_2} \end{Bmatrix}, \text{ where } \boldsymbol{U_i} = \begin{Bmatrix} X_i \\ \Theta_i \end{Bmatrix}, \boldsymbol{G_{ij}} = \begin{bmatrix} H_{ij} & L_{ij} \\ N_{ij} & P_{ij} \end{bmatrix}, \text{ and } \boldsymbol{Q_j} = \begin{Bmatrix} F_j \\ M_j \end{Bmatrix} \tag{2.11}$$

To determine the four assembly receptances at the free end of the cylinder, $\boldsymbol{G_{11}}$, the generalized force $\boldsymbol{Q_1}$ is applied to assembly coordinate $\boldsymbol{U_1}$ as shown in Figure 2-3, where the generalized U_i and u_i vectors are shown schematically as "displacements", although they describe both transverse deflection and rotation. The associated equilibrium conditions are $\boldsymbol{q_{2a}} + \boldsymbol{q_{2b}} = 0$ (i.e., the internal forces/couples are balanced) and $\boldsymbol{q_1} = \boldsymbol{Q_1}$ (because the component and assembly generalized forces are located at the same spatial location).

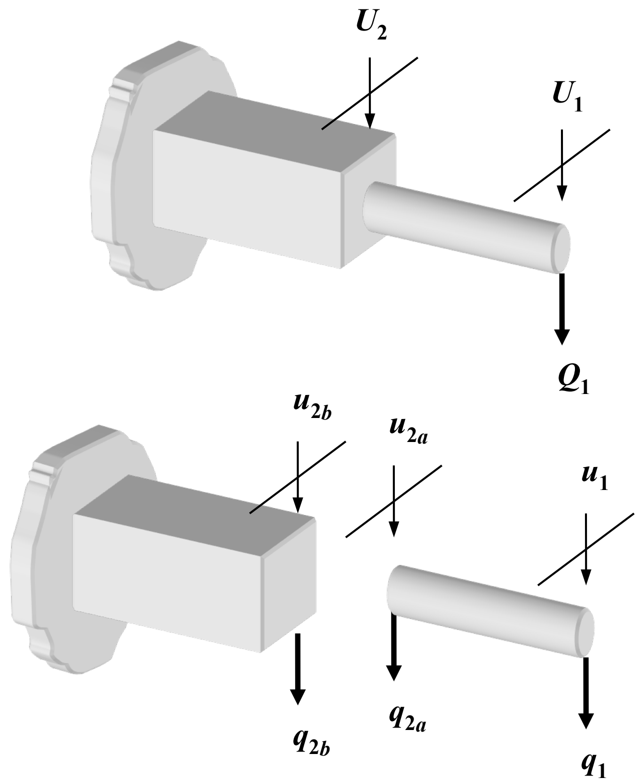

Figure 2-3. Receptance coupling model for determining $\boldsymbol{G}_{11}$ using a rigid connection. (Top) assembly. (Bottom) components.

By substituting the component displacements/rotations and equilibrium conditions into the compatibility condition, the expression for $\boldsymbol{q}_{2b}$ shown in Eq. 2.12 is obtained. The component force $\boldsymbol{q}_{2a}$ is then determined from the equilibrium condition $\boldsymbol{q}_{2a} = -\boldsymbol{q}_{2b}$.

$$\begin{aligned}
&\boldsymbol{u}_{2b} - \boldsymbol{u}_{2a} = 0 \\
&\boldsymbol{R}_{2b2b}\boldsymbol{q}_{2b} - \boldsymbol{R}_{2a1}\boldsymbol{q}_{1} - \boldsymbol{R}_{2a2a}\boldsymbol{q}_{2a} = 0 \\
&(\boldsymbol{R}_{2a2a} + \boldsymbol{R}_{2b2b})\boldsymbol{q}_{2b} - \boldsymbol{R}_{2a1}\boldsymbol{Q}_{1} = 0 \\
&\boldsymbol{q}_{2b} = (\boldsymbol{R}_{2a2a} + \boldsymbol{R}_{2b2b})^{-1}\boldsymbol{R}_{2a1}\boldsymbol{Q}_{1}
\end{aligned} \tag{2.12}$$

The expression for $\boldsymbol{G}_{11}$ is given by Eq. 2.13. The (1, 1) location, H_{11}, in the 2×2 matrix, $\boldsymbol{G}_{11}$, is the displacement-to-force receptance required for milling stability prediction.

$$\begin{aligned}
\boldsymbol{G}_{11} = \frac{\boldsymbol{U}_1}{\boldsymbol{Q}_1} = \frac{\boldsymbol{u}_1}{\boldsymbol{Q}_1} &= \frac{\boldsymbol{R}_{11}\boldsymbol{q}_1 + \boldsymbol{R}_{12a}\boldsymbol{q}_{2a}}{\boldsymbol{Q}_1} \\
&= \frac{\boldsymbol{R}_{11}\boldsymbol{Q}_1 - \boldsymbol{R}_{12a}(\boldsymbol{R}_{2a2a} + \boldsymbol{R}_{2b2b})^{-1}\boldsymbol{R}_{2a1}\boldsymbol{Q}_1}{\boldsymbol{Q}_1} \\
\boldsymbol{G}_{11} = \boldsymbol{R}_{11} - \boldsymbol{R}_{12a}(\boldsymbol{R}_{2a2a} + \boldsymbol{R}_{2b2b})^{-1}\boldsymbol{R}_{2a1} &= \begin{bmatrix} H_{11} & L_{11} \\ N_{11} & P_{11} \end{bmatrix}
\end{aligned} \tag{2.13}$$

For a non-rigid coupling with energy dissipation (damping) between the tool and holder, Eq. 2.13 is modified to include a connection stiffness matrix, [$\boldsymbol{K}$], as shown in Eq. 2.14.

$$\boldsymbol{G}_{11} = \boldsymbol{R}_{11} - \boldsymbol{R}_{12a}(\boldsymbol{R}_{2a2a} + \boldsymbol{R}_{2b2b} + \boldsymbol{K}^{-1})^{-1}\boldsymbol{R}_{2a1} = \begin{bmatrix} H_{11} & L_{11} \\ N_{11} & P_{11} \end{bmatrix} \tag{2.14}$$

The complex-valued, frequency-dependent connection stiffness matrix is defined in Eq. 2.15, where k indicates stiffness, c represents viscous damping, and ω is frequency. The subscripts for the 2×2 stiffness matrix entries identify their function. For example, $k_{\theta f}$ represents resistance to rotation due to an applied force.

$$[\boldsymbol{K}] = \begin{bmatrix} k_{xf} + i\omega c_{xf} & k_{\theta f} + i\omega c_{\theta f} \\ k_{xm} + i\omega c_{xm} & k_{\theta m} + i\omega c_{\theta m} \end{bmatrix} \tag{2.15}$$

In 2005, Duncan and Schmitz [15] expanded the RCSA model, and applied a three-component model. The spindle-machine receptances were identified by impact testing of a standard artifact; see Figure 2-4, where the tool is component I, the holder is component II, and the spindle-machine is component III, which contains the machine, spindle, portion of the holder inside the spindle (i.e., the taper), and the holder flange. This is a convenient separation point for the holder because the flange geometry is consistent for any spindle-holder interface, such as HSK-63A or CAT40. This is required for automatic tool changers to have a uniform geometry to grip.

As shown, the tool (component I) and holder (II) receptances can be modeled using beam theory. This dissertation highlights the limitations of previously studied methods for modeling of the fluted portion of the tool. Once evaluated, the generalized receptance matrices, R_{ij}, can be populated. For the spindle-machine (III), however, measurements are necessary because the required information is not generally available to accurately model this complex component. To enable identification of both the displacement and rotation receptances, a standard artifact is inserted in the spindle. The artifact-spindle-machine model is displayed in Figure 2-5. It is composed of the portion of the artifact beyond the spindle flange (component II) and the spindle-machine (component III), where the spindle-machine receptances are required to predict the tool tip receptances for arbitrary combinations of tools and holders inserted in the selected spindle-machine.

The artifact-spindle-machine receptances are written by modifying Eq. 2.13. By replacing coordinate 1 with 2, coordinate 2a with 3a, and coordinate 2b with 3b, the assembly receptances in Eq. 2.16 are obtained.

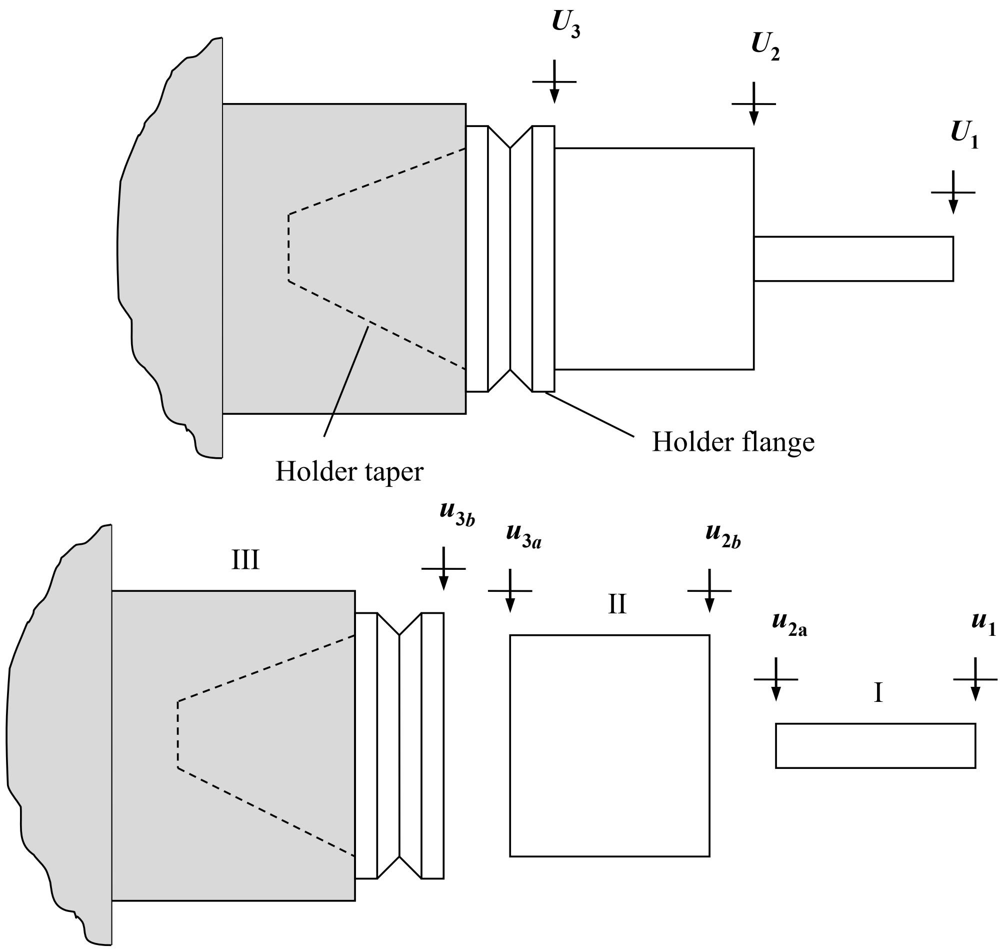

Figure 2-4. Three-component RCSA model with the spindle-machine identified as component III. (Top) assembly. (Bottom) components.

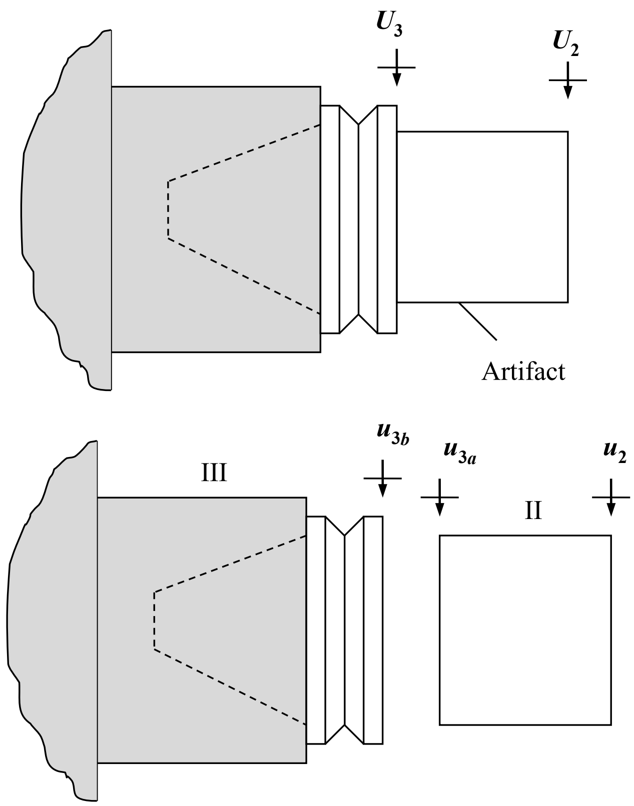

Figure 2-5. Artifact-spindle-machine model. (Top) assembly. (Bottom) components.

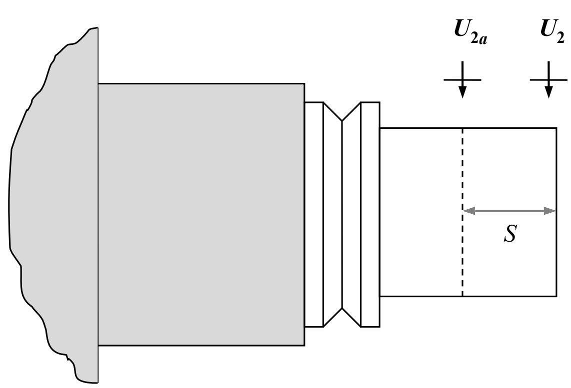

Figure 2-6. Direct and cross artifact-spindle-machine assembly measurement locations used to determine assembly rotation-to-force receptance $\boldsymbol{N}_{22}$.

$$G_{22} = R_{22} - R_{23a}(R_{3a3a} + R_{3b3b})^{-1}R_{3a2} = \begin{bmatrix} H_{22} & L_{22} \\ N_{22} & P_{22} \end{bmatrix} \tag{2.16}$$

Unlike the tool-holder-spindle-machine model, where the desired prediction outcome is the tool tip assembly receptances contained in the generalized matrix $\boldsymbol{G_{11}}$ (Eq. 2.13), the intent in this case is to determine the component receptances $\boldsymbol{R_{3b3b}}$. This generalized receptance matrix contains the receptances for the spindle-machine, which are not conveniently modeled or measured. To determine $\boldsymbol{R_{3b3b}}$, an inverse RCSA approach is applied where Eq. 2.16 is rewritten to solve for $\boldsymbol{R_{3b3b}}$. See Eq. 2.17.

$$R_{3b3b} = R_{3a2}(R_{22} - G_{22})^{-1}R_{23a} - R_{3a3a} = \begin{bmatrix} h_{3b3b} & l_{3b3b} \\ n_{3b3b} & p_{3b3b} \end{bmatrix} \tag{2.17}$$

Here, the $\boldsymbol{G_{22}}$ assembly receptances are measured, while the $\boldsymbol{R_{22}}$, $\boldsymbol{R_{23a}}$, $\boldsymbol{R_{3a2}}$, and $\boldsymbol{R_{3a3a}}$ component receptances are modeled. As before, either Euler-Bernoulli or Timoshenko beam models may be applied to describe the component receptances. To determine the four $\boldsymbol{G_{22}}$ receptances, the displacement-to-force direct receptance $H_{22} = \frac{X_2}{F_2}$ may be measured by tap testing, where an impact hammer is used to excite the artifact-spindle-machine assembly at coordinate 2 and the response is measured at the same location using a low-mass accelerometer or other linear sensor. To find the rotation-to-force receptance $N_{22} = \frac{\Theta_2}{F_2}$, a first-order finite difference approach may be implemented [16]. By measuring both the direct receptance H_{22} and the cross receptance $H_{2a2} = \frac{X_{2a}}{F_2}$, N_{22} may be calculated using Eq. 2.18. The displacement-to-force cross receptance H_{2a2} is obtained by exciting the assembly at $\boldsymbol{U_2}$ and measuring the response at coordinate $\boldsymbol{U_{2a}}$, located a distance S from the artifact's free end, as shown in Figure 2-6. Equivalently, H_{22a} could be measured, where the linear transducer is placed at $\boldsymbol{U_2}$ and the force is applied at $\boldsymbol{U_{2a}}$.

$$H_{22} = \frac{H_{22} - H_{2a2}}{S} = \frac{H_{22} - H_{22a}}{S} \tag{2.18}$$

The other off-diagonal term in the Eq. 2.16 $\boldsymbol{G_{22}}$ matrix term is assigned by reciprocity, $L_{22} = N_{22}$. Finally, P_{22} may be determined by synthesis using Eq. 2.19 [17]. Given a fully populated assembly matrix, $\boldsymbol{G_{22}}$, Eq. 2.17 may be used to determine the spindle-machine receptances and this result may be archived and used to predict the tool tip receptance for any tool-holder combination.

$$P_{22} = \frac{\Theta_2}{M_2} = \frac{F_2}{X_2}\frac{X_2}{M_2}\frac{\Theta_2}{F_2} = \frac{1}{H_{22}}L_{22}N_{22} = \frac{{N_{22}}^2}{H_{22}} \tag{2.19}$$

Following the initial paper [7], contributions have been made by numerous authors to expand on the RCSA model. Efforts have included: tool-holder receptance modeling, connection modeling, spindle-machine receptance, and applications of RCSA.

Modeling

In the first RCSA study [7], the tool was modeled as an Euler-Bernoulli (EB) beam. This analytical approximation of transverse bending modes is sufficient for long, slender beams, but loses accuracy for short, non-slender beams [10], [12], [13]. Additional work using closed-form receptances of Euler-Bernoulli [10] beam to describe the tool tip FRF were presented in [7], [10], [12]–[14], [18]–[20]. Models of the tool and holder, and additional applications, using Timoshenko [8] beam theory were presented in [15], [21], [30]–[36], [22]–[29].

Initially [7], the holder-spindle-machine was treated as one structure. This segmentation does not take full advantage of the capability for the RCSA method to predict the resulting tool tip receptance for assemblies with variations in the holder as well as the cutting tool. In [3], [12], [15], [37]–[39] the authors present a three-component model: tool, holder, and spindle-machine. This allowed for a more general solution for modeling any tool-holder combination. Schmitz et al. [40], [41] described the tool, holder, and spindle-machine as "genes" in the “Machine Tool Genome Project” and used RCSA to predict the assembly FRFs (analogous to physical traits in the human genome) for pre-process parameter selection. Wen et al. also modeled the assembly as three substructures: machine-spindle-holder, holder-tool shank, and extended portion of the tool [42], [43].

Due to the difficulty in measurement, Schmitz and Donaldson assumed the rotational receptances to be zero [7]. Despite this simplification, accurate tooltip receptances were made for three different tools in the same holder-spindle-machine substructure using a single connection parameter matrix. Follow-on papers by Schmitz and colleagues [9-11] extended the experimental validation using new tool-holder-spindle-machine combinations with the same simplifications. In 2003, Park et al. [44] extended the RCSA approach to include rotational receptances. Burns and Schmitz [45] followed this work by incorporating rotational receptances in the holder-spindle-machine model to study the tool-holder connection parameters.

Several authors have presented methods for measuring or deriving rotational receptances. Kumar and Schmitz [46], [47] used a single, direct FRF measurement of an artifact mounted in a selected spindle to identify displacement and rotational spindle-machine receptances. Each mode in the direct FRF was fit as a fixed-free beam using a close-form Euler-Bernoulli model [10]. The rotational receptances were then obtained from the same beam models. Additional methods for determining rotational receptances or deriving them from translational receptances have been presented in [21], [48], [57], [58], [49]–[56].

An accurate model of the tool and holder are required for an accurate tool tip receptance prediction. Methods for simplifying the tool and holder geometry have been addressed. Several authors describe an equivalent diameter beam for the fluted portion of the endmill [59]–[64]. Özşahin and Altintas [65] predicted tool tip FRFs using RCSA with helix angle and lag angle considered when defining the fluted section of the endmill. Other authors used spectral- Tchebychev techniques [22], [66]. Zhang et al. coupled Timoshenko beam models of the holder and shank to receptances of the fluted portion of the tool found by FEA [23]. Tunc [64] implemented an STL slicing algorithm to determine the cross-sectional properties of the fluted section of the endmill and used the slices to develop an improved beam model for RCSA.

In general, no connection interface is rigid. The complex-valued, frequency-dependent connection stiffness matrix defined in Eq. 2.15, which accommodates a finite stiffness connection between the tool and holder, has been evaluated, and modified, by several authors. Researchers have identified a dependence of the connection parameters on holder type (e.g., thermal shrink fit vs. collet), tool diameter, tool extension length from the holder, and spindle speed [27], [28], [75]–[79], [67]–[74]. In addition, the spindle-holder connection stiffness and damping have also been studied for the taper interface and spindle design (e.g., HSK or CAT) [24], [25], [68], [71], [80]–[85] Impact testing [28], [71], [92], [74], [80], [86]–[91] , finite element analysis [43], [67], [98]–[100], [71], [72], [80], [93]–[97] and optimization algorithms and machine learning methods [73], [86], [87], [101]–[107] have all been implemented in connection parameter studies.

Given the predictive capability afforded by RCSA, many research groups have applied the method to assembly dynamics prediction in a wide variety of scenarios including:

- Milling stability prediction [5], [31], [116]–[120], [108]–[115]
- Machine tool design, characterization, and evaluation of pose dependent dynamics [33], [121], [130]–[135], [122]–[129]
- Tool and tool holder design [136], [137], [146], [138]–[145]
- Sensor filtering and compensation [147], [148], [157], [149]–[156]
- Micro-milling [30], [36], [124], [158]–[160]
- Turning (tool and workpiece modeling) [161]–[163]

- Workpiece dynamics [34], [164]–[167]
- Drilling [168], [169]

and others [4], [6], [177], [178], [126], [170]–[176].

Helical Structures

In milling, the rotating cutting tool (or endmill) typically has a helical profile. This helix angle has implications on cutting force and stability [3], surface finish [179], and chip evacuation [180]. The dynamic response of twisted cantilever beams has been studied in other fields, however there is little in the literature to describe the effect of the helix angle on the free-free receptance of the fluted portion of an endmill.

In 1953, Rosard demonstrated that for cantilevered components such as aircraft propellers or turbine blades, the natural frequency changes considerably with twist angle and width-to-thickness ratio [181]. This was described mathematically and demonstrated through impact testing of blade specimen welded to a large steel plate. DiPrima and Handelman define a vector representation of the natural frequency of a pre-twisted cantilever beam [182]. Dawson et al. described the effect of the slenderness ratio on the natural frequency of a twisted rectangular cross section with a fixed-free boundary condition [183].

Similarly, Carnegie and Thomas evaluated the bending vibration of pre-twisted and tapered cantilever blades [184]. Building on this work, Chen and Ho used a differential transform to describe the vibration of a twisted beam under axial load [185]. Banerjee evaluated the natural frequency of a twisted cantilever beam with a high aspect ratio using the Wittrick-Williams algorithm, and concludes that finite element analysis with sufficiently small segments may be used to describe a twisted beam. [186]. Additional work has been completed to evaluate the frequency response of rotating pre-twisted geometries with turbomachinery applications [187], [188].

While previous work in twisted cantilever beams illustrates a connection between angle of twist and a reduced natural frequency, these works do not report on structures under free-free boundary conditions. The free-free receptance of the fluted portion of the tool is required to predict milling stability using RCSA. Additionally, there are substantial differences in the modeling of an endmill when compared to a propeller. Endmills are typically shorter and less flexible, and the helix angle of a cutting tool is typically between 30 and 45 degrees. The two-diameter Timoshenko beam model with an applied helix factor proposed in this dissertation allows the free-free receptance of the fluted section of the endmill to be predicted with low computational cost.

CHAPTER THREE
MATERIALS AND METHODS

Milling

Milling is defined by a rotating tool with discrete cutting edges where the teeth enter and exit the cut each tool revolution. This produces a periodic forcing function [3] as the teeth enter and exit. This periodic force acts on the flexible tool-holder-spindle-machine assembly and produces tool vibration. As the tool vibrates, its displacement results in a variation in chip thickness as shown in Figure 3-1. The result is that the instantaneous chip thickness is a function of both the commanded chip thickness and tool vibration.

As the teeth rotate past the surface, the tool vibration leaves a wavy surface on the workpiece surface. As the next tooth removes material, the instantaneous chip thickness depends on the commanded chip thickness, the current tool vibration, and the surface left behind by the previous tooth. This can result in chip thickness variation depending on the vibration phase between the current tooth and previous tooth. The instantaneous chip thickness, h, can be written as a function of time:

$$h(t) = f_t \sin(\phi) + n(t - \tau) - n(t) \tag{3.1}$$

where $n(t - \tau)$ and $n(t)$ describe the vibration along the surface normal of the previous tooth and the current tooth respectively, f_t is the feed per tooth, τ is the tooth passing period (i.e., time for one tooth passage), and ϕ is the time-dependent angle of the rotating tool.

This dependence of the current chip thickness on the previous tool deflections introduces a time delay into the milling equations of motion. The time delay differential equations of motion can exhibit chatter, a self-excited vibration. The mechanism for chatter is the variation of chip thickness with the current and previous tooth vibrations and the

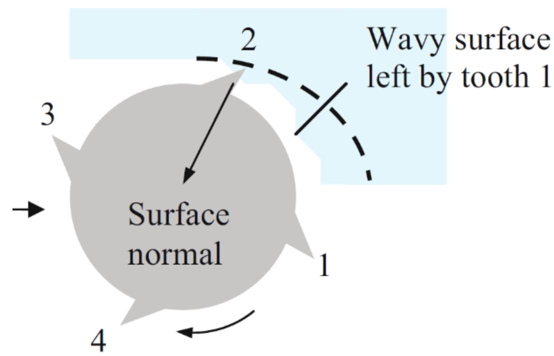

Figure 3-1. In milling, the instantaneous chip thickness is a function of the commanded chip thickness, the current tool vibration, and the vibration of the previous tooth (which is imprinted on the workpiece surface)[3].

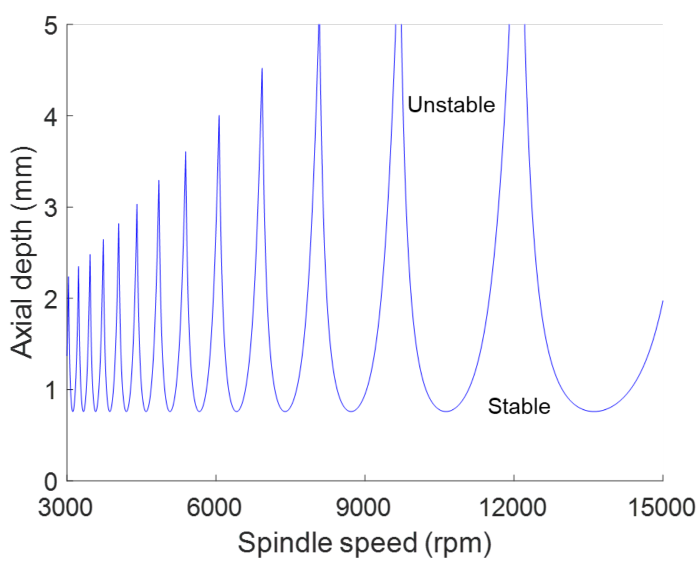

Figure 3-2. Stability map defining regions of stable and unstable machining parameters.

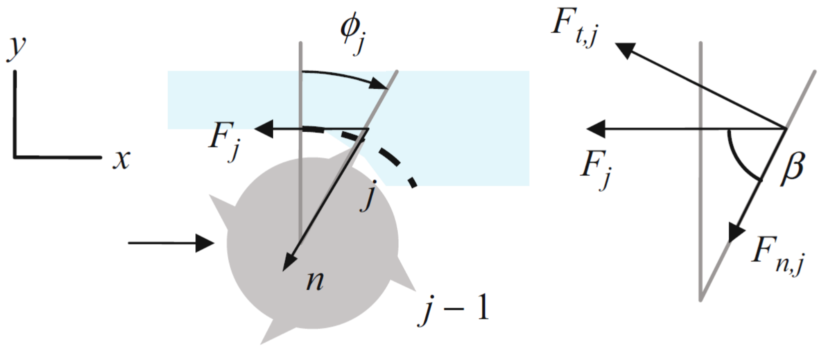

Figure 3-3. Notation for Fourier series stability analysis [3].

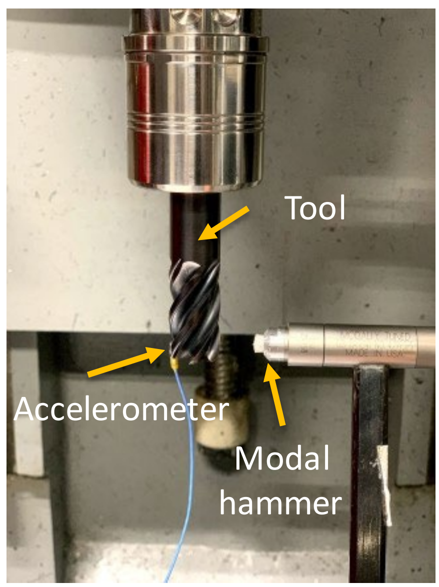

Figure 3-4. The tool tip FRF can be measured by impact testing using a modal hammer and accelerometer.

corresponding cutting force variation. It is referred to as regeneration (of waviness) in the literature [3]. The large forces and displacements that occur during chatter can lead to scrapped workpieces, broken tools, and potential damage to the spindle and machine.

Stability Maps

Stability maps define a boundary which separates stable and unstable spindle speed-depth of cut pairs for a given radial depth of cut. An example of a stability map is shown in Figure 3-2, where the area above the curve denotes unstable machining parameter combinations, and the area under the curve denotes stable machining parameter combinations. A frequency domain solution for the stability boundary is described in the following paragraphs. To validate the proposed two-diameter Timoshenko beam model, the tool tip FRF predicted by RCSA was used to generate a stability map using the frequency domain approach for a 15.875 mm diameter, four flute endmill.

Frequency domain stability boundary model

The Fourier series approach described by Altintas and Budak [2] is one method used to predict the stability boundary for milling operations. In this approach, the dynamic milling equations are transformed into a time invariant form by expanding the time varying coefficients into a Fourier series which is then truncated to only the average component. The model notation is shown in Figure 3-3.

The projection of the x (feed direction) and y vibration into the surface normal, n, or radial [2], direction is:

$$n = -x\sin(\phi) - y\cos(\phi) \tag{3.2}$$

where ϕ is the tooth angle. The instantaneous chip thickness of tooth j as a function of cutter angle is:

$$h(\phi_j) = \left(f_t \sin(\phi_j) + n_{j-1} - n_j\right) \cdot g(\phi_j) \tag{3.3}$$

where f_t is the feed per tooth and $g(\phi_j)$ is a switching function equal to one when the tooth is engaged in the cut and zero otherwise.

The tangential and normal force components, F_t and F_n, can be written as:

$$F_{t,j} = K_t b h(\phi_j) \tag{3.4}$$

$$F_{n,j} = K_n F_{t,j} = K_n K_t b h(\phi_j) \tag{3.5}$$

where b is the axial depth of cut, and K_t and K_n are cutting force coefficients in the tangential and normal directions. The tangential and normal force components can be projected into the x and y directions by:

$$F_{x,j} = -F_{t,j} \cos(\phi_j) - F_{n,j} \sin(\phi_j) \tag{3.6}$$

$$F_{y,j} = F_{t,j} \sin(\phi_j) - F_{n,j} \cos(\phi_j) \tag{3.7}$$

To account for multiple teeth in the cut, the forces are summed over the number of teeth N_t in the x and y directions.

$$F_x = \sum_{j=1}^{N_t} F_{x,j} \quad F_y = \sum_{j=1}^{N_t} F_{y,j} \tag{3.8}$$

The x and y forces can then be arranged in matrix form:

$$\begin{pmatrix} F_x \\ F_y \end{pmatrix} = \frac{1}{2} b K_t \begin{bmatrix} a_{xx} & a_{xy} \\ a_{yx} & a_{yy} \end{bmatrix} \begin{pmatrix} \Delta \mathrm{x} \\ \Delta \mathrm{y} \end{pmatrix} = \frac{1}{2} b K_t [A](\Delta) \tag{3.9}$$

where the components of the A matrix are the time varying directional dynamic force coefficients [2], each of which is a function of time. To remove the time dependence, $[A(\mathrm{t})]$ is expanded into a Fourier series:

$$[A(t)] = \sum_{r=-\infty}^{\infty} [A_r] e^{ir\omega_{tooth}t} \tag{3.10}$$

where ω_{tooth} is the tooth passing frequency. Setting $r = 0$ leads to the desired time invariance but reduces accuracy for small radial depths of cut where time in the cut is small. For the cutting tests used to evaluate the RCSA model, a radial depth of cut equal to the tool radius (i.e., 50% radial immersion) was used so the Fourier stability analysis method would be sufficiently accurate.

To analyze stability, frequency-domain vibrations are calculated using the product of the FRF matrix and frequency-domain force components.

$$\begin{pmatrix} X_j \\ Y_j \end{pmatrix} = \begin{bmatrix} FRF_{xx} & FRF_{xy} \\ FRF_{yx} & FRF_{yy} \end{bmatrix} \begin{pmatrix} F_x \\ F_y \end{pmatrix} e^{i\omega_c t} = \begin{bmatrix} FRF_{xx} & 0 \\ 0 & FRF_{yy} \end{bmatrix} \begin{pmatrix} F_x \\ F_y \end{pmatrix} e^{i\omega_c t} \tag{3.11}$$

The off-diagonal terms are set to zero in (3.11) because the x (feed) and y measurement directions are assumed orthogonal with zero-cross talk. The vibrations from the previous tooth period can be written as:

$$\begin{pmatrix} X_{j-1} \\ Y_{j-1} \end{pmatrix} = \begin{bmatrix} FRF_{xx} & 0 \\ 0 & FRF_{yy} \end{bmatrix} \begin{pmatrix} F_x \\ F_y \end{pmatrix} e^{i\omega_c t} \cdot e^{-i\omega_c \tau} \tag{3.12}$$

Taking the difference in vibrations between the current and previous vibrations yields:

$$\begin{pmatrix} X_j \\ Y_j \end{pmatrix} - \begin{pmatrix} X_{j-1} \\ Y_{j-1} \end{pmatrix} = (1 - e^{-i\omega_c \tau}) \begin{bmatrix} FRF_{xx} & 0 \\ 0 & FRF_{yy} \end{bmatrix} \begin{pmatrix} F_x \\ F_y \end{pmatrix} e^{i\omega_c t} = \begin{pmatrix} \Delta X \\ \Delta Y \end{pmatrix} \tag{3.13}$$

The form on the right-hand side allows substitution into the frequency-domain representation of Eq. 3.9, which can be rearranged to:

$$\begin{pmatrix} F_x \\ F_y \end{pmatrix} e^{i\omega_c t}\left([I] - \frac{1}{2} b K_t (1 - e^{i\omega_c \tau})[A_0]\begin{bmatrix} FRF_{xx} & 0 \\ 0 & FRF_{yy} \end{bmatrix}\right) = 0 \quad (3.14)$$

which has a non-trivial solution only if:

$$det\left([I] - \frac{1}{2} b K_t (1 - e^{i\omega_c \tau})[A_0]\begin{bmatrix} FRF_{xx} & 0 \\ 0 & FRF_{yy} \end{bmatrix}\right) = 0 \quad (3.15)$$

This is the characteristic equation of the dynamic milling system [2]. After substituting and expanding:

$$[A_0]\begin{bmatrix} FRF_{xx} & 0 \\ 0 & FRF_{yy} \end{bmatrix} = \frac{N_t}{2\pi}\begin{bmatrix} a_{xx} & a_{xy} \\ a_{yx} & a_{yy} \end{bmatrix}\begin{bmatrix} FRF_{xx} & 0 \\ 0 & FRF_{yy} \end{bmatrix} = \frac{N_t}{2\pi}\begin{bmatrix} a_{xx}FRF_{xx} & a_{xy}FRF_{yy} \\ a_{yx}FRF_{xx} & a_{yy}FRF_{yy} \end{bmatrix} = \frac{N_t}{2\pi}[FRF_{or}] \quad (3.16)$$

If Λ is defined as:

$$\Lambda = \frac{N_t}{2\pi}\left(-\frac{1}{2} b K_t (1 - e^{i\omega_c \tau})\right) \quad (3.17)$$

then the characteristic equation can be re-written as:

$$det([I] - \Lambda[FRF_{or}]) = 0 \quad (3.18)$$

Solving Eq. 3.18 results in a quadratic equation in Λ. Solving for $\Lambda_{1,2}$ using the quadratic formula yields two complex eigenvalues which are a function of ω_c, the chatter frequency should it occur.

Finally, the simplified expression for the stability limit b_{lim} can be written as:

$$b_{lim} = \frac{-2\pi}{N_t K_t}\Lambda_{Re}\left(1 + \left(\frac{\sin(\omega_c \tau)}{1 - \cos(\omega_c \tau)}\right)^2\right) = \frac{-2\pi}{N_t K_t}\Lambda_{Re}\left(1 + \left(\frac{\Lambda_{Im}}{\Lambda_{Re}}\right)^2\right) = \frac{-2\pi}{N_t K_t}\Lambda_{Re}(1 + \kappa^2) \quad (3.19)$$

The frequency-dependent spindle speeds are:

$$\Omega = \frac{60}{N_t \tau} \tag{3.20}$$

where the tooth passing period, τ, is defined by Eq. (3.21) where j is an integer, and ε is the phase shift in the surface undulations between subsequent tooth passages, see Eq. 3.22. Finally, b_{lim} and Ω are plotted against one another to predict the stability boundary.

$$\tau = \frac{1}{\omega_c}(\varepsilon + 2\pi \cdot j) \tag{3.21}$$

$$\varepsilon = \pi - 2\tan^{-1}(\kappa) \tag{3.22}$$

Cutting Force Coefficients

To predict the stability map, both the tool tip receptances and cutting force model are required. The cutting force coefficients required for a complete force model are tool-workpiece specific. Normal, tangential, and axial cutting force coefficients as well as the respective edge coefficients can be determined experimentally. To do so, cutting tests are completed at a single spindle speed over a range of feedrates on a workpiece fixed to a dynamometer, which measures the cutting force components in the x (feed), y, and z directions.

To identify the cutting force coefficients, the average of the force component in each direction is calculated over the range of selected feedrates. A linear regression is then applied to determine the six coefficients k_n, k_t, k_a, k_{ne}, k_{te}, and k_{ae} from the mean of the measured values using the three slope and three intercept values from the best fit lines. In this notation, the coefficient with a single-letter subscript identifies shearing, or cutting, coefficients. Coefficients with two-letter subscripts identify edge, or rubbing, effects. Given the coefficients, the force components in each direction can be calculated using Eq. 3.23 through Eq. 3.25.

$$F_x = k_t b f_t \sin(\phi)\cos(\phi) + k_{te} b \cos(\phi) + k_n b f_t \sin^2(\phi) + k_{ne} b \sin(\phi) \tag{3.23}$$

$$F_y = k_t b f_t \sin^2(\phi) + k_{te} b \sin(\phi) - k_n b f_t \sin(\phi)\cos(\phi) - k_{ne} b \cos(\phi) \tag{3.24}$$

$$F_z = -k_a b f_t \sin(\phi) - k_{ae} b \tag{3.25}$$

To calculate the mean force per revolution, all teeth on the cutter must be considered, and a switching function, $g(\phi_j)$, is incorporated which is non-zero between the cut start (ϕ_s) and exit (ϕ_e) angles only [3]. The total force can be calculated by Eq. 3.26 through Eq. 3.28.

$$F_x = \sum_{j=1}^{N_t} \left(k_t b f_t \frac{\sin(2\phi_j)}{2} + k_{te} b \cos(\phi_j) + k_n b f_t \frac{(1 - \cos(2\phi_j))}{2} + k_{ne} b \sin(\phi_j) \right) g(\phi_j) \tag{3.26}$$

$$F_y = \sum_{j=1}^{N_t} \left(k_t b f_t \frac{1 - \cos(2\phi_j)}{2} + k_{te} b \sin(\phi_j) - k_n b f_t \frac{\sin 2\phi_j}{2} - k_{ne} b \cos(\phi_j) \right) g(\phi_j) \tag{3.27}$$

$$F_z = \textstyle\sum_{j=1}^{N_t} (k_a b f_t \sin(\phi_j) - k_{ae} b) \times g(\phi_j) \tag{3.28}$$

The mean force can then be determined by integrating between the start and exit angles as shown in Eq. 3.29 for the *x* direction. The mean force in the *x* (feed), *y*, and *z* directions can be described by Eq. 3.30 to Eq. 3.32.

$$\bar{F}_x = \frac{1}{2\pi} \int_{\phi_s}^{\phi_e} F_x \, d\phi \tag{3.29}$$

$$\bar{F}_x = \left[\frac{N_t b f_t}{8\pi} (-k_t \cos(2\phi) + k_n (2\phi - \sin(2\phi))) + \frac{N_t b}{2\pi} (k_{te} \sin(\phi) - k_{ne} \cos(\phi)) \right]_{\phi_s}^{\phi_e} \tag{3.30}$$

$$\bar{F}_y = \left[\frac{N_t b f_t}{8\pi} (k_t (2\phi - \sin(2\phi)) + k_n \cos(2\phi)) - \frac{N_t b}{2\pi} (k_{te} \cos(\phi) + k_{ne} \sin(\phi)) \right]_{\phi_s}^{\phi_e} \tag{3.31}$$

$$\bar{F}_z = \left[\frac{N_t b}{2\pi} (k_a f_t \cos(\phi) - k_{ae} \phi) \right]_{\phi_s}^{\phi_e} \tag{3.32}$$

The best fit line from the linear regression for the *x* direction is represented by:

$$\bar{F}_{x,i} = a_{0x} + a_{1x} f_{t,i} + E_i \tag{3.33}$$

where $f_{t,i}$ and $\bar{F}_{x,i}$ are the commanded feed per tooth and resulting average force pairs, a_{0x} is the intercept of the line, a_{1x} is the slope, and E_i is the error between the measurement points and the best fit line. A 50% radial immersion down milling (climb milling) cut was used in this work to measure the cutting force coefficients. For this case, the start angle, ϕ_s, is 90° and the exit angle, ϕ_e, is 180° . Eq. 3.30 to Eq. 3.32 can be expanded and simplified to solve for the cutting force coefficients k_n, k_t, k_a and edge coefficients k_{ne}, k_{te}, k_{ae}. The expressions for the cutting force coefficients for a 50% radial immersion cut are given by Eq 3.34 through Eq. 3.39, where N_t is the number of teeth, *b* is the axial depth of cut, and a_1 and a_o are the slope and intercept determine by linear regression of the average force in the *x, y,* and *z* directions as shown in Eq. 3.33 for the *x* component.

$$k_n = \frac{8\pi}{N_t b(4+\pi^2)} \left(\pi a_{1x} + 2a_{1y}\right) \tag{3.34}$$

$$k_t = \frac{-8\pi}{N_t b(4+\pi^2)} \left(2a_{1x} - \pi a_{1y}\right) \tag{3.35}$$

$$k_a = \frac{-2\pi}{N_t b} (a_{1z}) \tag{3.36}$$

$$k_{ne} = \frac{\pi}{N_t b} \left(a_{0x} + a_{0y}\right) \tag{3.37}$$

$$k_{te} = \frac{\pi}{N_t b} \left(-a_{0x} + a_{0y}\right) \tag{3.38}$$

$$k_{ae} = \frac{-4}{N_t b} (a_{0z}) \tag{3.39}$$

Tool Tip Receptance

As shown in the previous section, the tool tip receptances in the x and y directions are required to generate a stability map using the Fourier series approach. Impact testing is an experimental method used to measure the dynamics of structures. This method is widely used to measure the tool tip FRF directly. In impact testing, a modal hammer, as shown in Figure 3-4, containing a force sensor in the tip, is used to generate a short duration impact on the object of interest. The impact excites a wide range of frequencies. This test is typically repeated multiple times and the results are averaged to improve the correlation between input force and measured vibration across the range of measured frequencies [3]. The vibration response is simultaneously measured by a transducer which may record displacement (to define the receptance), velocity (mobility), or acceleration (accelerance). The receptance is used for stability analysis. Any additional use of the term frequency response function (FRF) in this dissertation will refer to the receptance.

Receptance Coupling

In this study, receptance coupling substructure analysis (RCSA) is used to predict the tool tip FRF. The RCSA algorithm was presented in Chapter 2 and will not be repeated here. However, an update has been made to Eq. 2.15. By reciprocity (i.e., $\frac{X}{M} = \frac{\theta}{F}$), the connection parameter matrix can be re-written from 2.15 as:

$$[\boldsymbol{K}] = \begin{bmatrix} k_{xf} + i\omega c_{xf} & k_{\theta f} + i\omega c_{\theta f} \\ k_{xm} + i\omega c_{xm} & k_{\theta m} + i\omega c_{\theta m} \end{bmatrix} = \begin{bmatrix} k_{xf} + i\omega c_{xf} & k_{\theta f} + i\omega c_{\theta f} \\ k_{\theta f} + i\omega c_{\theta f} & k_{\theta m} + i\omega c_{\theta m} \end{bmatrix} \tag{3.40}$$

where the rotational stiffness and damping due to an applied force ($k_{\theta f}$ and $c_{\theta f}$) and the displacement to moment stiffness and damping (k_{xm} and c_{xm}) are equal. For the tool-holder receptance, it can be assumed that because lateral force at the end of the tool causes a rotation at the tool-holder location, the off-diagonal parameters have a greater contribution than the on-diagonal terms. In this case, the displacement to force (*xf* subscripts) and rotation to moment (θm subscripts) stiffness and damping terms are set to zero (Eq. 3.41).

$$[\boldsymbol{K}] = \begin{bmatrix} 0 & k_{\theta f} + i\omega c_{\theta f} \\ k_{\theta f} + i\omega c_{\theta f} & 0 \end{bmatrix} \qquad (3.41)$$

This method was developed to reduce the need for on-machine measurements of individual tools. As noted in Chapter 2, several key inputs are required to predict the tool tip receptance including: an artifact measurement of the spindle-machine, models of the tool and holder, and coupling parameters to define the flexible tool-holder joint. Both the tool and holder are modeled as a series of cylindrical beams as shown in cross-section in Figure 3-5, where the steel toolholder body is depicted in grey, and the carbide tool is shown in red. The free-free receptances of each are calculated using a Timoshenko beam model, described in the next section, and coupled as described in Chapter 2. A flow chart defining the required inputs to the RCSA algorithm is given in Figure 3-6.

Timoshenko Beam Theory

Previous work identifying the tool and holder dynamic response can be grouped into two main categories: finite element analysis and two-dimensional beam dynamics. In the former, the tool and holder are modeled as three-dimensional components which are discretized into volumetric elements. The natural frequencies, mode shapes, and corresponding frequency response function can be calculated. This is computationally expensive, and determining the receptance for a single model may take several hours.

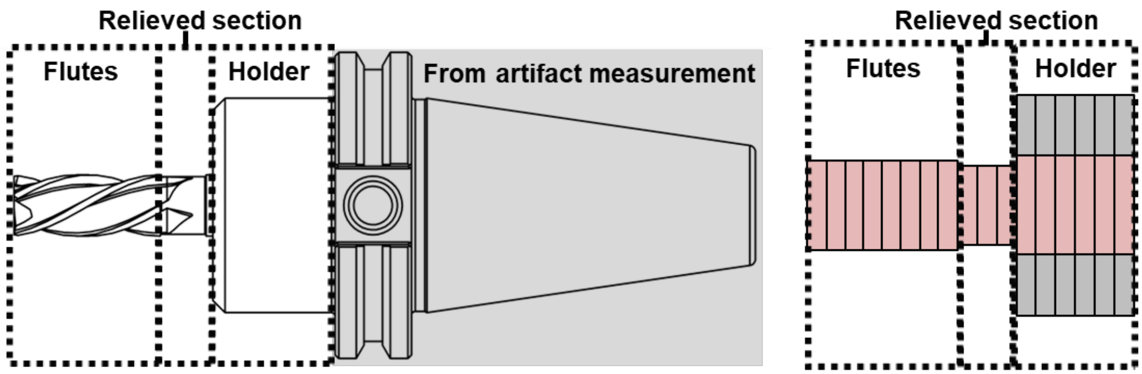

Figure 3-5. The tool and holder are modeled as a series of cylindrical elements.

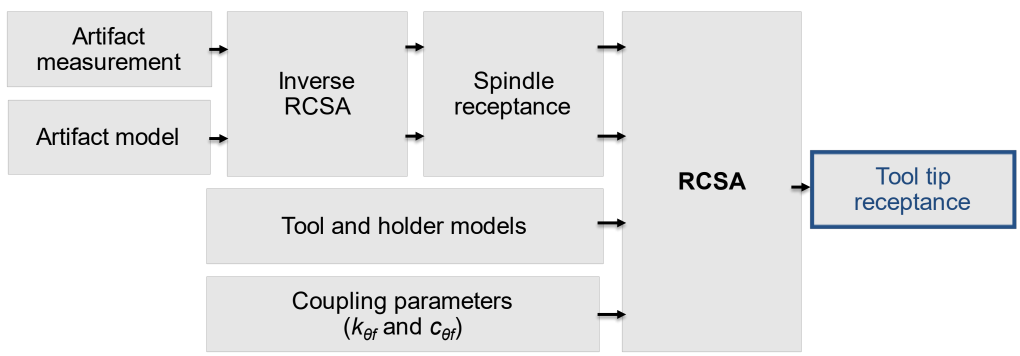

Figure 3-6. Inputs required for predicting tool tip receptance using RCSA.

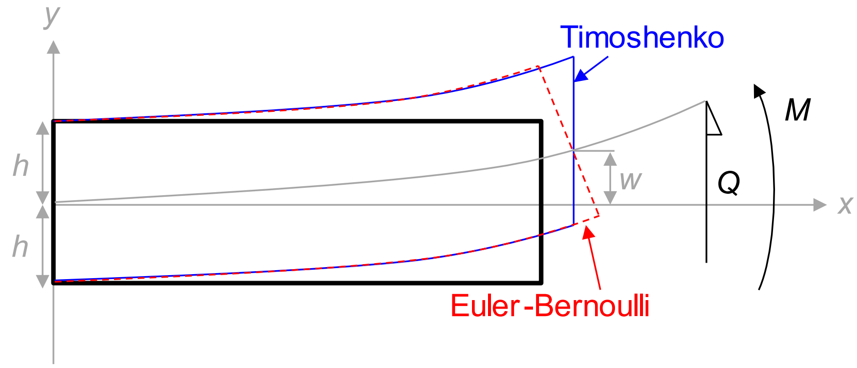

Figure 3-7. The Timoshenko model considers the shear deformation associated with bending.

Both Euler-Bernoulli and Timoshenko beam theory have been used to describe the tool and holder components as two-dimensional beam elements. The Euler-Bernoulli closed-form solution provides an analytical method for calculating receptance, but this model does not capture the effects of shear or rotary inertia. The accuracy is limited to beams with high length-to-diameter aspect ratios (approximately 10 to 1 or higher) [12].

The Timoshenko beam method considers shear deformation of the beam as shown in Figure 3-7. This model is better suited to beams with reduced length-to-diameter ratios (shorter, stiffer beams), and effectively introduces additional flexibility versus the Euler-Bernoulli method. The differential equation of motion is given in Eq. 3.42, where the second and third parenthetical term describe the shear deformation and rotary inertia effects. The addition of the inertial and shear effects improves the accuracy; however, the solution does not have a closed form and must be calculated numerically.

$$\left(\frac{d^2y}{dt^2}+\frac{EI}{\rho A}\frac{d^4y}{dx^4}\right)+\left(\frac{\rho I}{\hat{k}AG}\frac{d^4y}{dt^4}+\frac{EI}{\hat{k}AG}\frac{d^4y}{dx^2dt^2}\right)-\left(\frac{I}{A}\frac{d^4y}{dx^2dt^2}\right)=0 \tag{3.42}$$

The shape factor, $\hat{k}$, is defined in Eq. 3.43 for a cylindrical cross-section, where ν is Poisson's ratio, a mechanical property relating strain in orthogonal directions [189]. The shear modulus, *G,* is defined by Eq. 3.44, where *E* is the elastic modulus (Young's modulus). The second moment of area, *I*, and the area, *A*, for a circular cross section are given in Eq. 3.45 and 3.46 respectively, where *d* is the diameter. The material density is denoted as ρ. The material properties attributed to the tool and holder components are given in Table 3-1.

$$\hat{k}=\frac{6+12\nu+6\nu^2}{7+12\nu+4\nu^2} \tag{3.43}$$

$$G=\frac{E}{2(1+\nu)} \tag{3.44}$$

$$I_{circle,x} = I_{circle,y} = \frac{\pi}{4} r^4 = \frac{\pi}{64} d^4 \tag{3.45}$$

$$A_{circle} = \pi r^2 = \frac{\pi}{4} d^2 \tag{3.46}$$

To implement the Timoshenko beam model, free-free elements are described using mass, *M*, and stiffness, *K*, matrices [15] for each of the four degrees of freedom (rotation and translation at each end of the element):

$$M = \frac{\rho A l}{(1+\phi)^2} \begin{bmatrix} \frac{13}{35} + \frac{7\phi}{10} + \frac{\phi^2}{3} & \left(\frac{11}{210} + \frac{11\phi}{120} + \frac{\phi^2}{24}\right) l & \frac{9}{70} + \frac{3\phi}{10} + \frac{\phi^2}{6} & -\left(\frac{13}{420} + \frac{3\phi}{40} + \frac{\phi^2}{24}\right) l \\ & \left(\frac{1}{105} + \frac{\phi}{60} + \frac{\phi^2}{120}\right) l^2 & \left(\frac{13}{420} + \frac{3\phi}{40} + \frac{\phi^2}{24}\right) l & -\left(\frac{1}{140} + \frac{\phi}{60} + \frac{\phi^2}{120}\right) l^2 \\ & & \frac{13}{35} + \frac{7\phi}{10} + \frac{\phi^2}{3} & -\left(\frac{11}{210} + \frac{11\phi}{120} + \frac{\phi^2}{24}\right) l \\ Symmetric & & & -\left(\frac{1}{105} + \frac{\phi}{60} + \frac{\phi^2}{120}\right) l^2 \end{bmatrix}$$
$$+ \frac{\rho A l}{(1+\phi)^2} \left(\frac{r_g}{l}\right)^2 \begin{bmatrix} \frac{6}{5} & \left(\frac{1}{10} + \frac{\phi}{2}\right) l & -\frac{6}{5} & \left(\frac{1}{10} - \frac{\phi}{2}\right) l \\ & \left(\frac{2}{15} + \frac{\phi}{6} + \frac{\phi^2}{3}\right) l^2 & -\left(\frac{1}{10} + \frac{\phi}{2}\right) l & -\left(\frac{1}{30} + \frac{\phi}{6} + \frac{\phi^2}{6}\right) l^2 \\ & & \frac{6}{5} & -\left(\frac{1}{10} - \frac{\phi}{2}\right) l \\ Symmetric & & & \left(\frac{2}{15} + \frac{\phi}{6} + \frac{\phi^2}{3}\right) l^2 \end{bmatrix} \tag{3.47}$$

$$K = \frac{EI(1+i\eta)}{l^3(1+\phi)^2} \begin{bmatrix} 12 & 6l & -12 & 6l \\ & (4+2\phi+\phi^2) l^2 & -6l & (2-2\phi-\phi^2) l^2 \\ & & 12 & -6l \\ Symmetric & & & (4+2\phi+\phi^2) l^2 \end{bmatrix}$$
$$+ \frac{\hat{k} A G \phi^2}{4l(1+\phi)^2} \begin{bmatrix} 4 & 2l & -4 & 2l \\ & l^2 & -2l & l^2 \\ & & 4 & -2l \\ Symmetric & & & l^2 \end{bmatrix} \tag{3.48}$$

where l is the section length, r_g is the radius of gyration described by Eq. 3.49, and ϕ is a shear deformation parameter defined by Eq 3.50.

$$r_g = \sqrt{\frac{I}{A}} \tag{3.49}$$

$$\phi = \frac{12EI(1+\eta)}{\hat{k}GAl^2} \tag{3.50}$$

As discussed in Chapter 2, previous works have described the fluted section of the cutting tool by a single equivalent diameter. The equivalent diameter based on second moment of area, d_I, and cross sectional area, d_A, can be calculated by equating the second moment of area and cross sectional area of the actual cross section to the expression for a circular cross section given in Eq. 3.45 and Eq. 3.46. The corresponding diameter is the equivalent diameter for the selected cross section as shown in Figure 3-8.

First, simple cross sections (square, triangular, and rectangular) were evaluated using the equivalent diameter calculated using the area and second moment of area. These were then compared to a finite element result. Second, the receptance was predicted using the new two-diameter approach, where d_A is used to calculate the mass matrix such that Eq. 3.47 can be expanded as:

$$M = \frac{\frac{\pi}{4}{d_A}^2\rho l}{(1+\phi)^2}[\cdots] + \frac{\frac{\pi}{4}{d_A}^2\rho l}{(1+\phi)^2}\left(\frac{r_g}{l}\right)^2[\cdots] \tag{3.51}$$

and d_I is used to calculate the stiffness matrix, such that Eq. 3.48 becomes:

$$K = \frac{\frac{\pi}{64}{d_I}^4E(1+i\eta)}{l^3(1+\phi)^2}[\cdots] + \frac{\frac{\pi}{4}{d_A}^2\hat{k}G\phi^2}{4l(1+\phi)^2}[\cdots] \tag{3.52}$$

The radius of gyration and shear deformation parameter can also be updated as:

$$r_g = \sqrt{\frac{1}{16}\frac{{d_I}^4}{{d_A}^2}} \tag{3.53}$$

$$\phi = \frac{3}{4}\frac{{d_I}^4 E(1+\eta)}{{d_A}^2 \hat{k} G l^2} \tag{3.54}$$

This method was then applied to a variety of endmill cross sections. The profile of a single flute was approximated by line segments with a 0.05 mm point spacing in the *x* direction for 2 to 7 flute tools. As shown in Figure 3-9, a single flute profile (shown in red) was constructed, and the set of points was copied to form the tool profile. The geometry and resulting receptance for the Figure 3-9 tool cross section was later compared to points from a scanned cross section.

For each endmill geometry, the cross sectional properties must be calculated by point-to-point summation. The expressions for calculating the second moment of area and cross section area for an arbitrary polygon are given in Eq. 3.55 through Eq. 3.57, where the subscripts *i* and *i+1* denote the *x* or *y* coordinate of the current and following point respectively. It should be noted that for all regular polygons, $I_x = I_y$. For endmills with more than two evenly spaced cutting flutes, the cross-sectional area is a regular polygon. In these cases, the model is axisymmetric, and there is no preferential bending direction. For two flute tools, $I_x \neq I_y$, and the response is asymmetric. Two flute tools will be treated as a special case, where the directionally dependent receptances will be calculated separately.

$$I_{endmill,x} = \frac{1}{12}\sum_{i=1}^{n}\left((x_i y_{i+1} - x_{i+1} y_i)(y_i^2 + y_i y_{i+1} + y_{i+1}^2)\right) \tag{3.55}$$

$$I_{endmill,y} = \frac{1}{12}\sum_{i=1}^{n}\left((y_i x_{i+1} - y_{i+1} x_i)(x_i^2 + x_i x_{i+1} + x_{i+1}^2)\right) \tag{3.56}$$

$$A_{endmill} = \frac{1}{2}\sum_{i=1}^{n}\left((y_i + y_{i+1})(x_i - x_{i+1})\right) \tag{3.57}$$

An equivalent diameter based on second moment of area, d_I, can be calculated by equating Eqs. 3.45 and 3.55 to form Eq. 3.58. An equivalent diameter based on cross-sectional area, d_A, can be calculated by equating Eq. 3.46 and 3.57 as shown in Eq. 3.59. In both cases, only the positive root of the expression yields a valid equivalent diameter.

$$d_I = \sqrt[4]{\frac{16}{3\pi}\sum_{i=1}^{n}\left((x_i y_{i+1} - x_{i+1} y_i)(y_i^2 + y_i y_{i+1} + y_{i+1}^2)\right)} \tag{3.58}$$

$$d_A = \sqrt{\frac{2}{\pi}\sum_{i=1}^{n}\left((y_i + y_{i+1})(x_i - x_{i+1})\right)} \tag{3.59}$$

A significant limitation of the Timoshenko beam model as presented is the inability to evaluate the variation in receptance as a function of the helix angle of the tool (i.e., it is based on a cross section that does not vary along the beam length). As the helix angle increases from zero, the mass of the structure does not change, but the natural frequency and stiffness decrease as a function of the twist/helix angle. To capture this effect in the two-diameter Timoshenko model, a helix factor was applied to the flexural stiffness, *EI,* term in the stiffness matrix. The helix factor was determined as a function of number of teeth, length to diameter ratio (L:D) of the flutes, tool diameter, and helix angle.

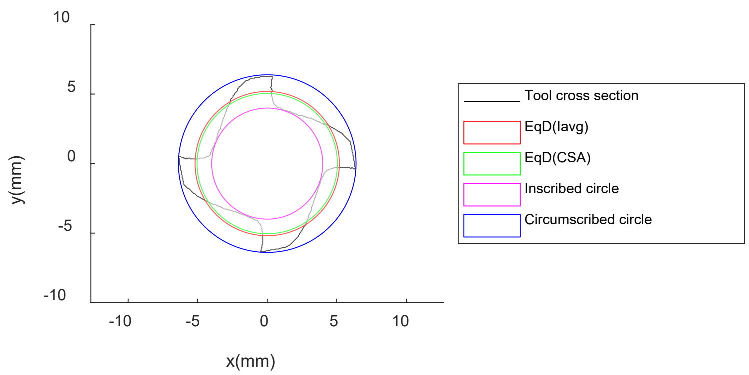

Figure 3-8. Equivalent diameter based on second moment of area and cross sectional area.

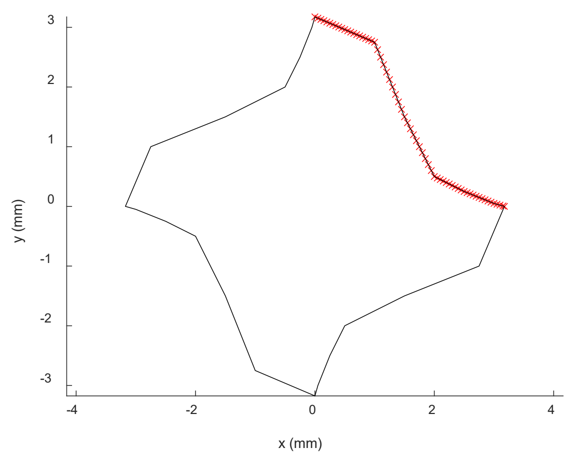

Figure 3-9. Linear approximation of a four flute endmill cross-section. The distance between points defining the profile is 0.05 mm in the *X* direction.

Table 3-1. Tool holder and endmill material properties.

Material	**Component**	**Elastic modulus (GPa)**	**Density (kg/m^3)**	**Poisson's ratio (-)**
Steel	Holder	200	7800	0.29
Carbide	Endmill	611	15100	0.22

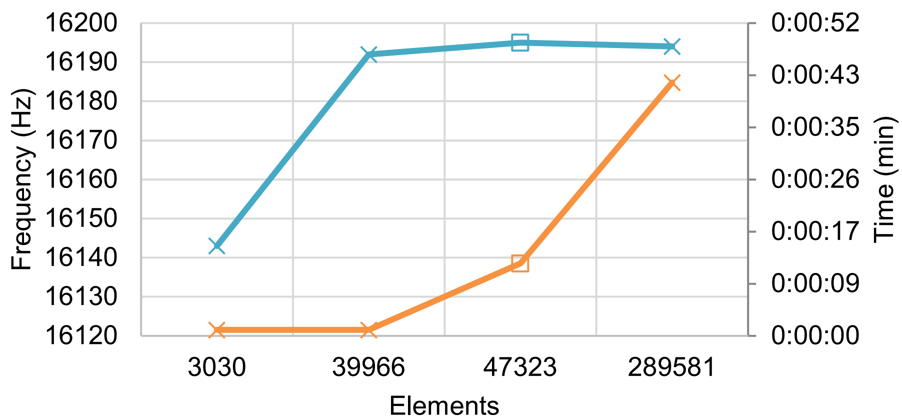

Figure 3-10. A convergence study was completed by successively halving the element size. The selected element size is noted with a square marker.

Finite Element Analysis

The Timoshenko beam model does not account for the effect of helix angle on the resulting tool tip receptances. The helix effect is captured in three-dimensional finite element analysis, however. Finite element analysis therefore provides a numerical approach for determining the helix factor to compensate the constant cross section Timoshenko beam model.

A grid of 576 total tool geometry combinations were evaluated to develop a helix angle dependent two-diameter Timoshenko beam model to predict the tool tip receptance of helical endmills. Six diameters [6.35, 9.53, 12.7, 15.88, 19.05, and 25.4] mm were evaluated over six flute counts [2, 3, 4, 5, 6, and 7] per diameter, D, with four different length to diameter ratios [2, 3, 4, 6] and four helix angles [0, 30, 38, 45] degrees per flute count. These parameters were selected to include the most commonly available endmill geometries [190].

Dassault Systemes SolidWorks frequency and linear dynamic analysis packages were used to evaluate the natural frequency of each modeled tool geometry. For all endmill models, a blended curvature-based mesh element was selected. This mesh type “adapts the element size to the local curvature of the geometry to create a smooth mesh pattern” [191]. A convergence study for the frequency study as shown in Figure 3-10 was completed, and a maximum element size of 0.5mm and minimum element size of 0.25mm were used for all models.

CHAPTER FOUR
RESULTS AND DISCUSSION

Test Sequence

This section describes the evaluation of the two-diameter Timoshenko beam model for basic cross sections and its application to endmill geometries, the addition of a helix factor and length to diameter ratio dependence for the two-diameter Timoshenko beam model, validation of the new two-diameter model for the fluted portion of a helical endmill, and comparison of the tool-holder-spindle-machine receptance predicted by RCSA to measurement. Finally, the predicted tool tip receptance is used together with the cutting force model to predict the stability limit.

Basic Geometry

To test the new two-diameter Timoshenko beam model, basic polygon shapes were first selected for analysis. The dynamic responses of beams with square, triangular, and rectangular cross sections shown in Figure 4-1 were evaluated. The dimensions for each beam are given in Table 4-1. The carbide material properties are listed in Table 3-1.

The equivalent diameter based on area (*CSA*) and second moment of area (*Ix*) was calculated for each cross section. These equivalent diameters are shown in relation to the cross section profile for all three shapes in Figure 4-2 through Figure 4-4. For the rectangular cross section, which exhibits asymmetry about x and y, the equivalent diameter is shown for the second moment of area about both the x and y axes.

Each beam was modeled using the FEA approach outlined in Chapter 3. The finite element analysis solution for the first bending natural frequency was compared to the single-

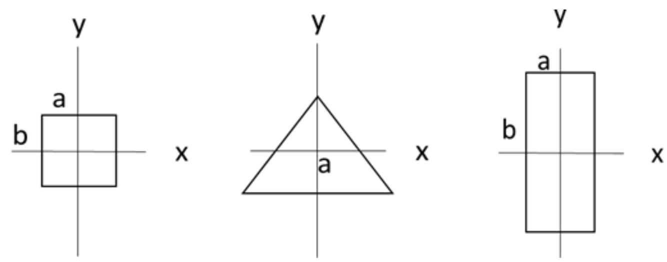

Figure 4-1. Simple beam cross sections.

Table 4-1. Dimensions for beams with simple cross sections.

Cross section	**Square**	**Triangle**	**Rectangle**
Side length a (mm)	10	10	5
Side length b (mm)	10	-	10
Length (mm)	100	100	100

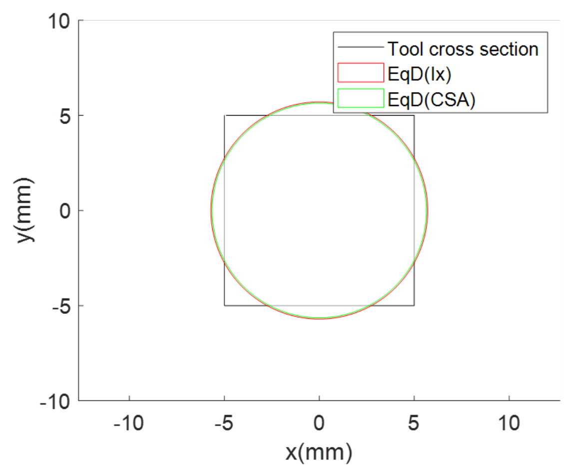

Figure 4-2. Equivalent diameters based on second moment of area, EqD(Ix), and cross sectional area, EqD(CSA), for a square cross section.

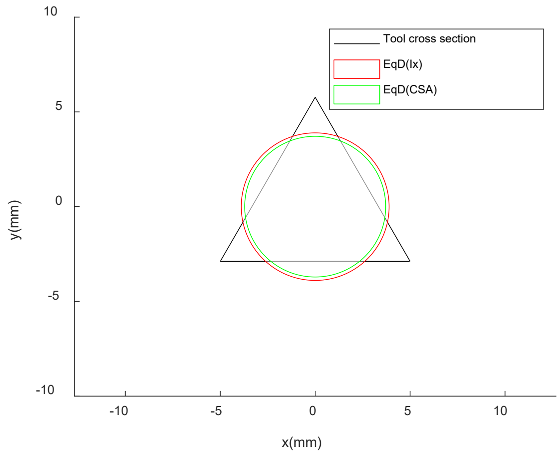

Figure 4-3. Equivalent diameters based on second moment of area and cross sectional area for a triangular cross section.

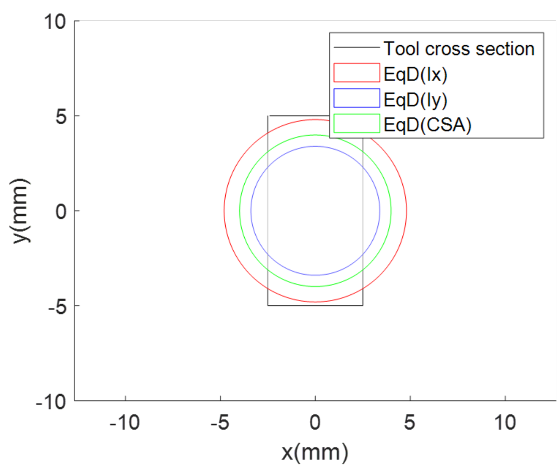

Figure 4-4. Equivalent diameters based on second moment of area and cross sectional area for a rectangular cross section. Both x and y equivalent diameters are shown for the second moment of area approximation.

Table 4-2. The comparison of natural frequency predicted by FEA, single-diameter Timoshenko beam model, and a two-diameter Timoshenko beam model. The percent difference from FEA is reported.

Cross section		**FEA**	**Single-diameter d_I**	**Single-diameter d_A**	**Two-diameter**
Square	**Frequency (Hz)**	6322.9	6257.2	6189.8	6325.1
	% difference	-	1.04%	2.11%	-0.03%
Triangle	**Frequency (Hz)**	4540.2	4341.3	4145.6	4545.3
	% difference	-	4.38%	8.69%	-0.11%
Rectangle (about y)	**Frequency (Hz)**	3241.4	3798.1	4445.3	3241.3
	% difference	-	-17.17%	-37.14%	0.00%
Rectangle (about x)	**Frequency (Hz)**	6323.2	5310.3	4445.3	6325.1
	% difference	-	16.02%	29.70%	-0.03%

diameter Timoshenko beam solution for both the area and second moment of area equivalent diameters. These results were then compared to the new two-diameter solution.

For the rectangular beam, the natural frequencies for bending about the x and y directions were calculated using FEA. In the single-diameter approach, the diameter calculated from the cross-sectional area performs poorly as there is no directional dependence for the area calculation. The equivalent diameter for the second moment of area about y, I_y, was used to predict the first (less stiff) natural frequency. The second moment about x, I_x, was used to predict the second natural frequency. In the two-diameter Timoshenko beam model, the I_x and I_y terms were likewise used to predict the first and second natural frequencies.

The results in Table 4-2 show significant improvement in agreement with FEA for the two-diameter Timoshenko beam model for all three cross sections versus the single-diameter approach.

Endmill Geometry

Endmill geometries were selected based on commonly available diameters, flute counts, helix angles, and length to diameter ratios. First, a zero helix (or straight flute) cutter model was evaluated using the two-diameter Timoshenko beam model. Second, a helix angle factor was incorporated to account for stiffness changes due to non-zero helix angles and length to diameter ratio effects were observed. Third, the two-diameter Timoshenko model with helix factor was used to predict the receptance of the fluted portion of an endmill (tool) and compared to measurement.

Zero Helix Angle

The two-diameter Timoshenko beam model was evaluated for fluted cross sections with zero helix (or straight flute) models. The equivalent diameter based on area and second moment of area was calculated for each cross section. These equivalent diameters are shown in relation to the cross section profile for a 12.7 mm diameter, three flute endmill in Figure 4-5.

These predictions were made for 12.7mm diameter tool profiles with [3, 4, 5, 6, and 7] flutes and a length to diameter ratio of 4:1. The results shown in Table 4-2 demonstrate significant improvement in agreement with FEA for the two-diameter Timoshenko beam model versus the single-diameter approach using the equivalent diameter from cross sectional area or second moment of area.

Helix Angle and Length to Diameter Ratio

As discussed in Chapter 2, it has been observed that twisted structures exhibit a reduction in natural frequency and stiffness versus their untwisted counterparts. In most machining applications, endmills with a defined helix angle are used, Figure 4-8.

Finite element analysis was used as the basis for evaluating the effects of the helix angle on endmill models of various diameters and flute counts as discussed in Chapter 3. To establish confidence in the finite element analysis approach, a 19.05 mm diameter, 100 mm long, four flute tool model was evaluated for helix angles ranging from 0 to 60 degrees. A high-density polymer which could be printed using fused deposition modeling was selected so that physical models could be tested. The material properties for ULTEM are given in Table 4-4. The free-free receptance of the printed flute geometries were measured by impact testing as shown in Figure 4-6. The resulting measured and simulated natural frequencies are given in Table 4-5.

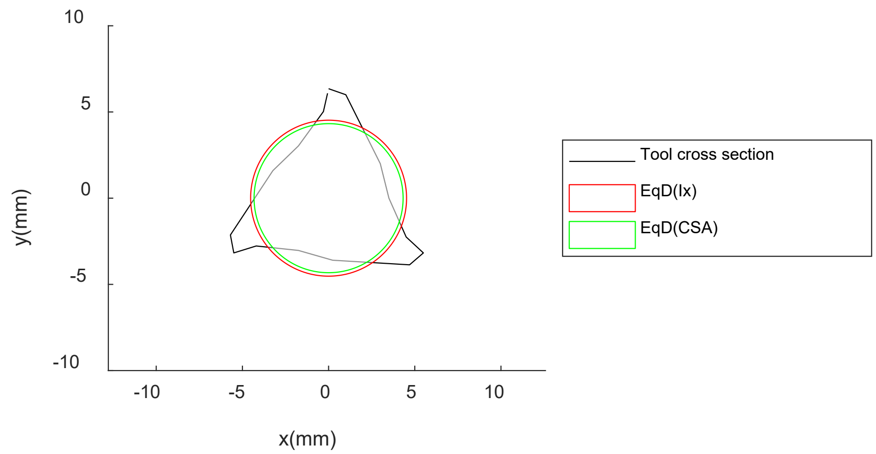

Figure 4-5. Equivalent diameters based on second moment of area, EqD(Ix), and cross sectional area, EqD(CSA), for the cross section of a 12.7 mm diameter three flute tool.

Table 4-3. The comparison of natural frequency predicted by FEA, single-diameter Timoshenko beam model, and a two-diameter Timoshenko beam model. The percent difference from FEA is reported.

Flutes		**FEA**	**Single-diameter d_I**	**Single-diameter d_A**	**Two-diameter**
3	**Frequency (Hz)**	19064	18444	17730.5	19178.5
	% difference	-	-3.3	-7.0	0.6
4	**Frequency (Hz)**	20692	20335	19893.5	20783.5
	% difference	-	-1.7	-3.9	0.4
5	**Frequency (Hz)**	21012	20810	20561.5	21060.5
	% difference	-	-1.0	-2.1	0.2
6	**Frequency (Hz)**	21583	21403.5	21166.5	21641.5
	% difference	-	-0.8	-1.9	0.3
7	**Frequency (Hz)**	21477	21305	21080	21531.5
	% difference	-	-0.8	-1.8	0.3

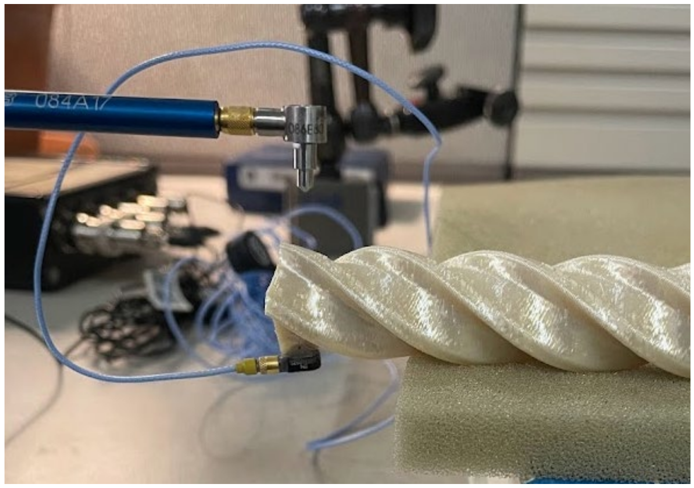

Figure 4-6. Free-free impact testing of an additively manufactured tool flute geometry.

Table 4-4. ULTEM material properties.

Material	Elastic modulus (GPa)	Density (kg/m^3)	Poisson's ratio (-)
ULTEM	2.54	1340	0.25

Table 4-5. The measured and simulated frequency response for ULTEM tool geometries with different helix angles.

Helix angle (deg)	Measured frequency (Hz)	FEA frequency (Hz)	Two-diameter Timoshenko frequency (Hz)
0	1816	1763.8	1769.1
10	-	1747.5	-
20	1753	1699.4	-
30	-	1623.0	-
40	1573	1526.0	-
45	-	1473.9	-
50	-	1422.3	-
60	1371	1328.6	-

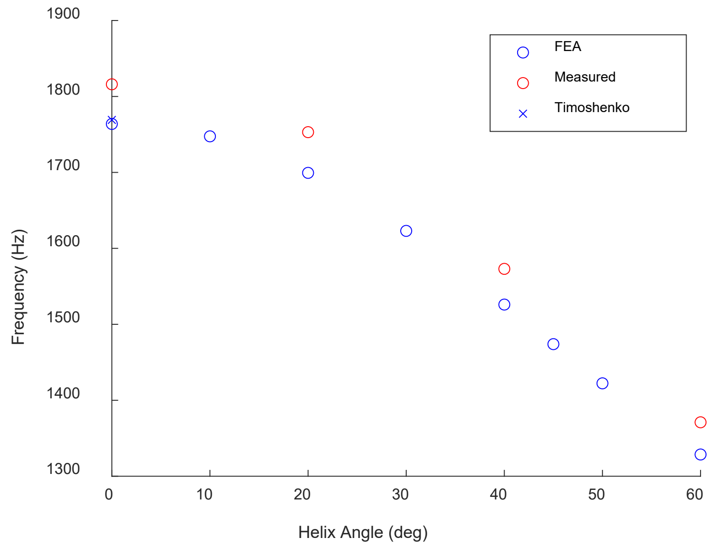

Figure 4-7. Natural frequency versus helix angle for measured and simulated ULTEM tool geometries.

The two-diameter Timoshenko beam model was used to predict the tool receptance. However, because the Timoshenko beam model did not have a dependence on helix angle, this approach could only be used to determine receptance for the zero degree helix model. The results for the natural frequencies obtained by measurement, FEA, and the two-diameter Timoshenko beam model are shown in Figure 4-7. The quadratic trend of the measured test points closely matches that of the finite element analysis. The constant offset is assumed to be due to variation in the bulk material properties assigned to the simulations versus the as-printed properties.

Three-dimensional finite element models were generated for 576 diameter, flute count, helix angle, and length to diameter ratio combinations. A surface map relating the FEA computed natural frequencies, f_n, to their respective helix angle, γ, and length to diameter ratio, LD was generated for each tool diameter-flute count combination. An example map for a 12.7 mm diameter endmill with five teeth is shown for helix angles [0 30 38 45]° and [2 3 4 6] length to diameter ratios in Figure 4-9.

The equation for the best fit surface relating the helix angle, γ, and length to diameter ratio, *LD*, to the corresponding natural frequency is given by Eq. 4.1. The coefficients, $C_{0\text{-}5}$, are given in Table A-0-1 for each tool diameter- flute count pair.

$$f_n = C_0 + C_1\gamma + C_2 LD + C_3\gamma^2 + C_4\gamma LD + C_5 LD^2 \tag{4.1}$$

To account for the change in natural frequency and stiffness in the two-diameter Timoshenko model due to the helix angle, a helix factor, *F*, was applied to the flexural rigidity term, *EI*, during the construction of the stiffness matrix. Equations 3.48 and 3.54 can be updated to include the helix factor; see Eq. 4.2 and Eq. 4.3.

$$K = \frac{FEI(1+i\eta)}{l^3(1+\phi)^2}\begin{bmatrix} 12 & 6l & -12 & 6l \\ & (4+2\phi+\phi^2)l^2 & -6l & (2-2\phi-\phi^2)l^2 \\ & & 12 & -6l \\ Symmetric & & & (4+2\phi+\phi^2)l^2 \end{bmatrix} + \frac{\hat{k}AG\phi^2}{4l(1+\phi)^2}\begin{bmatrix} 4 & 2l & -4 & 2l \\ & l^2 & -2l & l^2 \\ & & 4 & -2l \\ Symmetric & & & l^2 \end{bmatrix} \tag{4.2}$$

$$\phi = \frac{3}{4}\frac{{d_I}^4 E(1+\eta)}{{d_A}^2 \hat{k} G l^2} \tag{4.3}$$

For each diameter- flute count- length combination, a series of receptances was calculated using the two-diameter Timoshenko model with helix factors ranging from 0.5 to 1 in increments of 0.025, where *F=1* corresponds to a zero degree helix angle.

The results for a 12.7 mm diameter four flute tool are shown in Figure 4-10. The frequency change with helix factor was shown to be quadratic. Natural frequencies predicted by FEA for each of the tool geometries were then used to relate the helix angle to the helix factor.

A surface plot is shown in Figure 4-11 relating the helix factor to the natural frequency and length to diameter ratio. The general form of the equation is given in Eq. 4.4, where *F* is the helix factor. The fitting coefficients, $H_{0\text{-}5}$, are given in Table A-0-2.

$$F = H_0 + H_1 f_n + H_2 LD + H_3 {f_n}^2 + H_4 f_n LD + H_5 LD^2 \tag{4.4}$$

To validate the coefficients, a tool was selected with a helix angle and length to diameter ratio that were not in the original set of test geometries. A 12.7 mm diameter, three flute tool with a length to diameter ratio of 2.5:1 and a helix angle of 40 degrees was evaluated. The predicted natural frequency, f_n, was calculated by Eq. 4.1 using the calculated coefficients provided in Table A-0-1. The predicted natural frequency was 20793.3 Hz. The helix factor was then calculated using Eq. 4.4 and the corresponding coefficients from Table A-0-2 to be 0.712. This helix factor was then used in the two-diameter Timoshenko beam model to predict the receptance for the tool geometry. Figure 4-12 shows the resulting

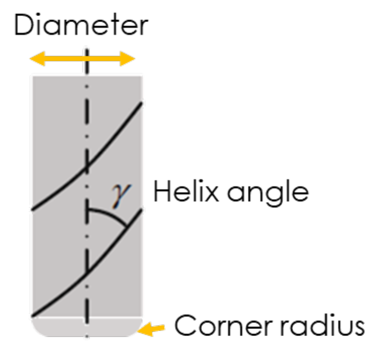

Figure 4-8. The helix angle of the endmill is defined as the angle of the flute from the tool centerline.

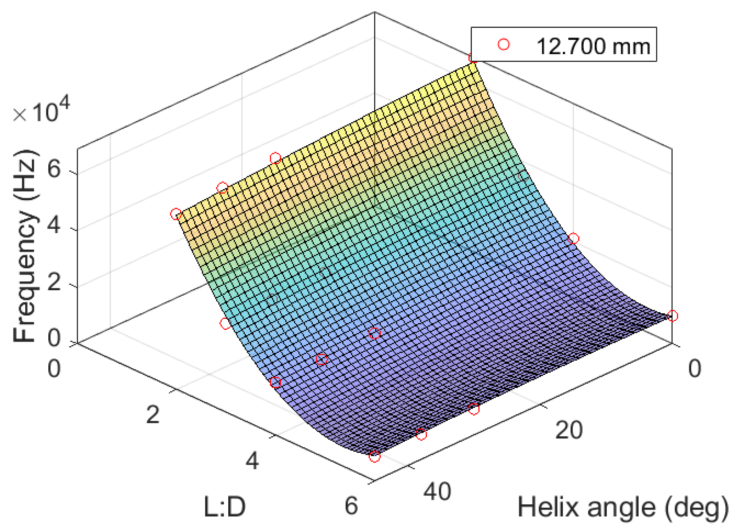

Figure 4-9. The surface map relating helix angle and length to diameter (L:D) ratio to corresponding natural frequency for a 12.7 mm diameter endmill with five teeth. The circles identify FEA results and the surface represents the fit.

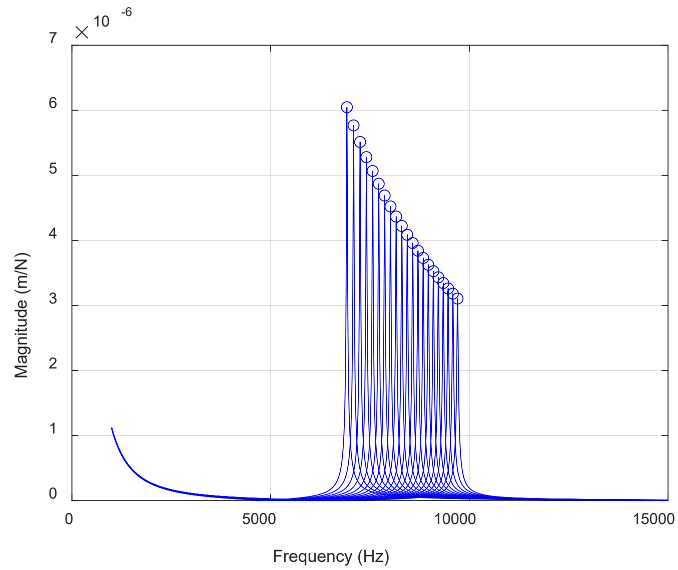

Figure 4-10. A series of receptances were calculated using the two-diameter Timoshenko beam model for a 12.7 mm diameter tool. Each peak in the magnitude plot represents a different helix factor from 0.5 to 1.

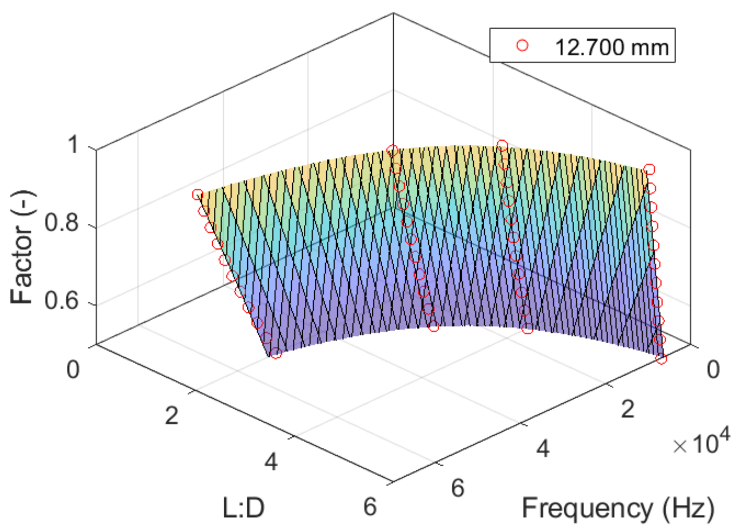

Figure 4-11. The surface map relating length to diameter ratio and natural frequency to corresponding helix factor for a 12.7 mm diameter endmill with five teeth.

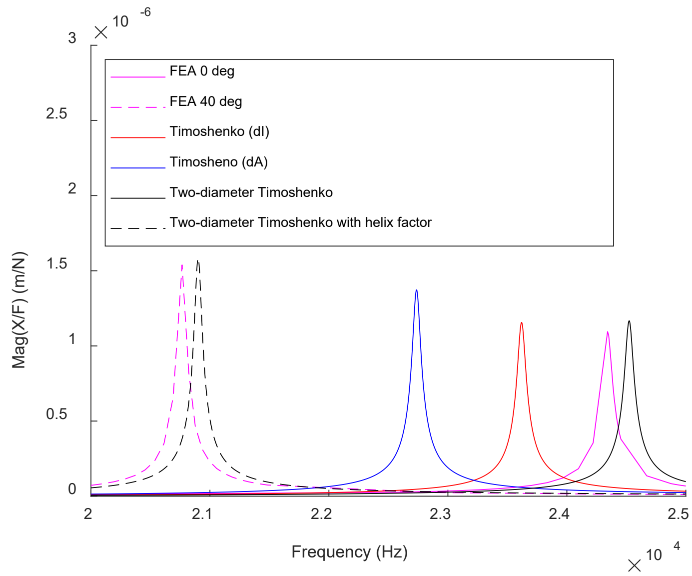

Figure 4-12. The receptances for a 12.7 mm diameter three flute tool with a 40 degree helix angle and 2.5:1 length to diameter ratio.

receptances from FEA for a zero helix (straight tooth) tool, the FEA result for the 40 degree helix, the single-diameter Timoshenko beam model results, and the two-diameter Timoshenko beam model result with and without the helix factor applied. The two-diameter Timoshenko beam model significantly outperforms the single-diameter method for the tool model with and without a helix.

Fluted Receptance Validation

A 12.7 mm diameter, four flute endmill was selected to compare the FEA simulation, single-diameter Timoshenko beam model, and new two-diameter Timoshenko beam model with and without the helix factor. The endmill was sectioned by electrical discharge machining (EDM) to separate the fully cylindrical shank and fluted portion. Dimensions of both components are given in Table 4-6. The solid shank was used to identify material properties, and the fluted section was used to evaluate the two-diameter Timoshenko beam model.

In the previously studies reported in this document, literature values for the material properties of carbide were used; see Table 3-1. For this test, the tool shank was used to determine the material properties of the tool to minimize their effects on discrepancies in the measured and simulated results. Density, Poisson's ratio, and elastic modulus are required material property inputs to the Timoshenko beam model.

The density was calculated using the measured mass (Figure 4-13) and volume calculated from the shank dimensions (Figure 4-14). The calculated density was 14357.6 kg/m^3.

The effect of Poisson's ratio on receptance was evaluated over a range of possible values found in the literature. The receptance was predicted for values ranging from 0.18 to 0.28 in 0.01 increment steps. Sensitivity to Poisson's ratio was found to be low as shown in Figure 4-15. The typical value of 0.22 was used.

Figure 4-13. The mass of the tool shank was measured and used to calculate the carbide shank density.

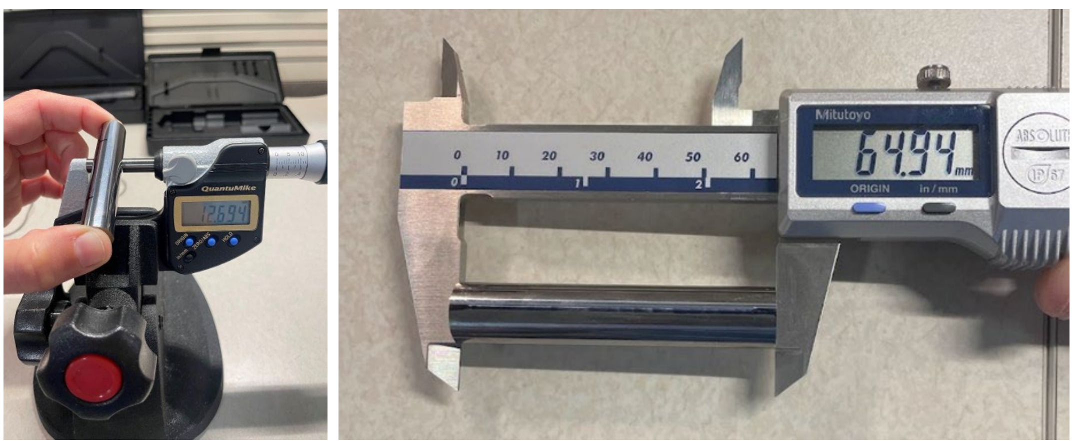

Figure 4-14. The shank diameter was measured using micrometers (left) and the length was measured using calipers (right) to calculate the volume and the carbide shank density.

Table 4-6. Dimensions of the tool shank and fluted portions of the sectioned endmill.

	Shank	Flutes
Diameter (mm)	12.7	12.7
Length (mm)	64.94	76.32

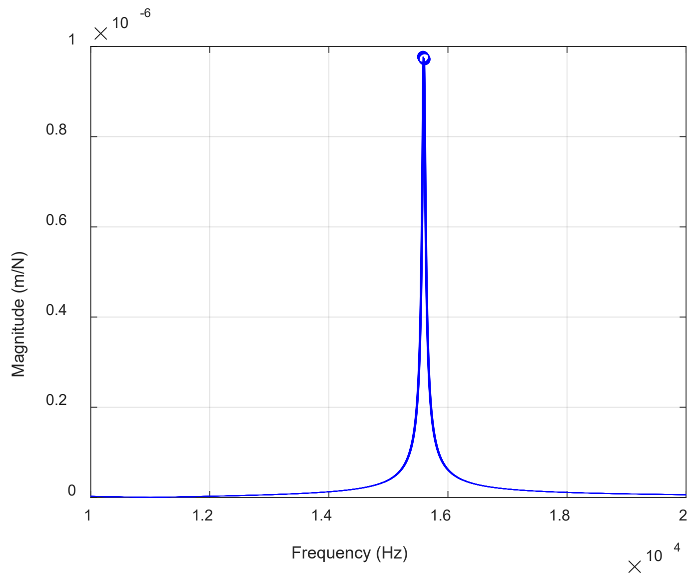

Figure 4-15. Receptances were calculated for a range of Poisson's ratio values.

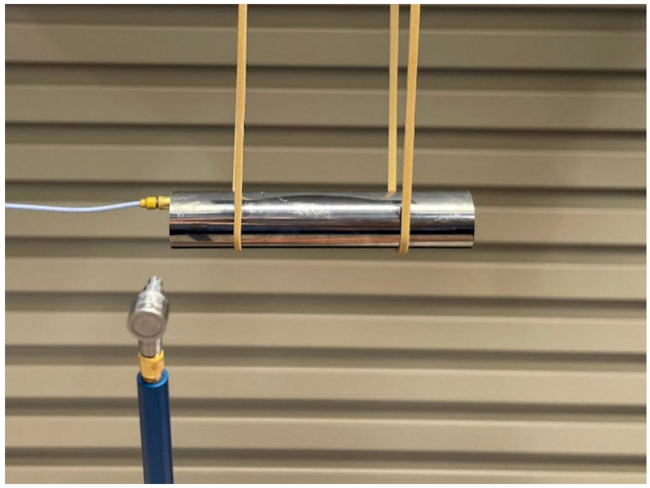

Figure 4-16. The tool shank was suspended using soft elastic supports to approximate a free-free boundary condition.

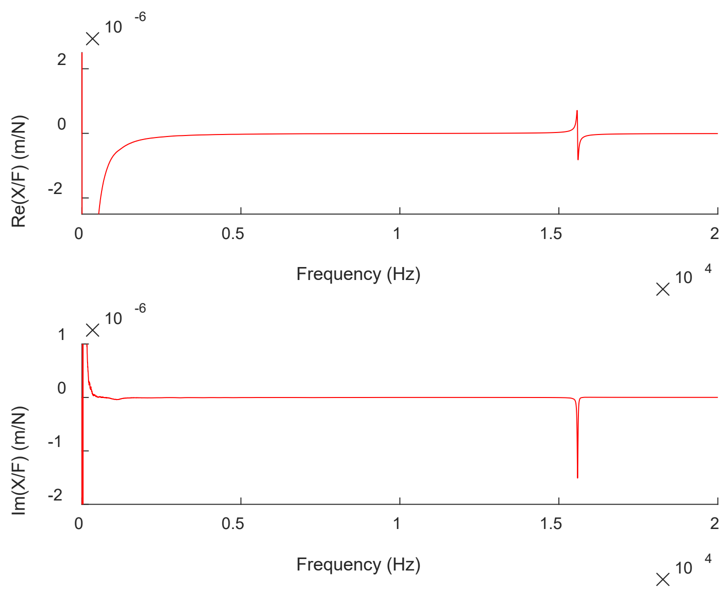

Figure 4-17. The measured free-free boundary conditions FRF for the tool shank.

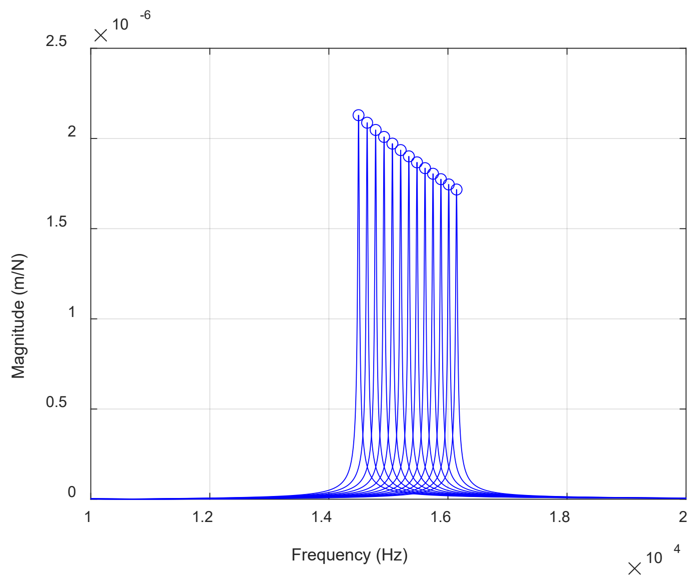

Figure 4-18. Receptances were calculated for a range of elastic modulus values from 500 GPa to 620 GPa.

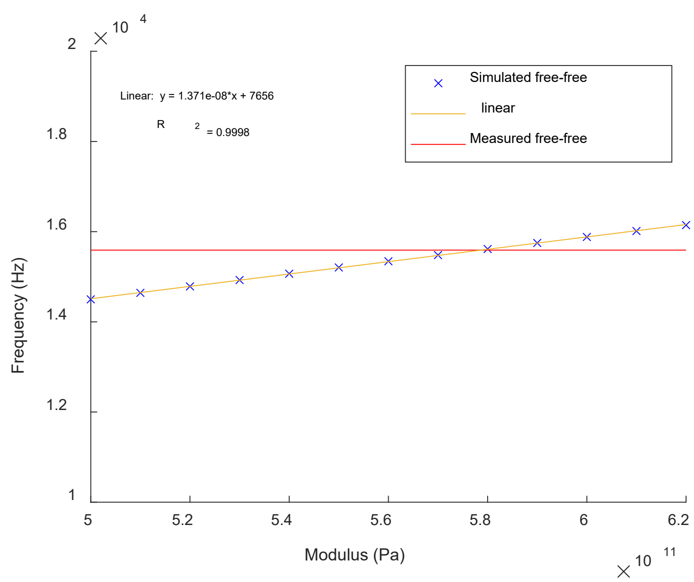

Figure 4-19. The linear best fit of the resulting natural frequency from the range of simulated elastic modulus values was compared to the measured free-free natural frequency and used to determine the tool modulus.

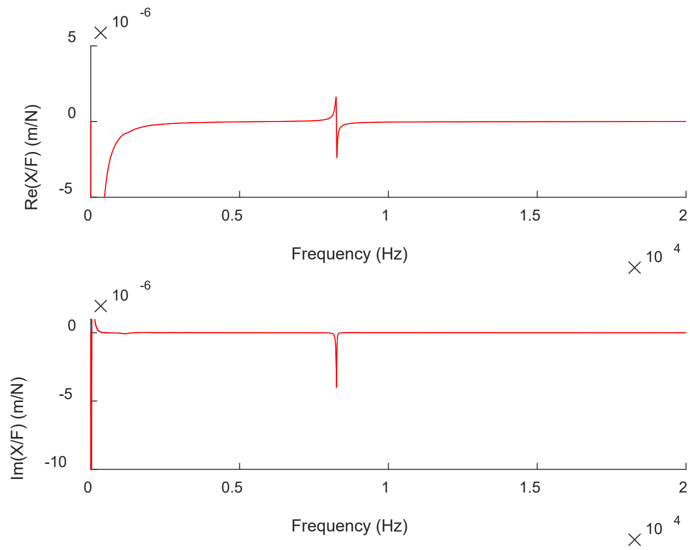

Figure 4-20. The measured free-free FRF for the fluted portion of the endmill.

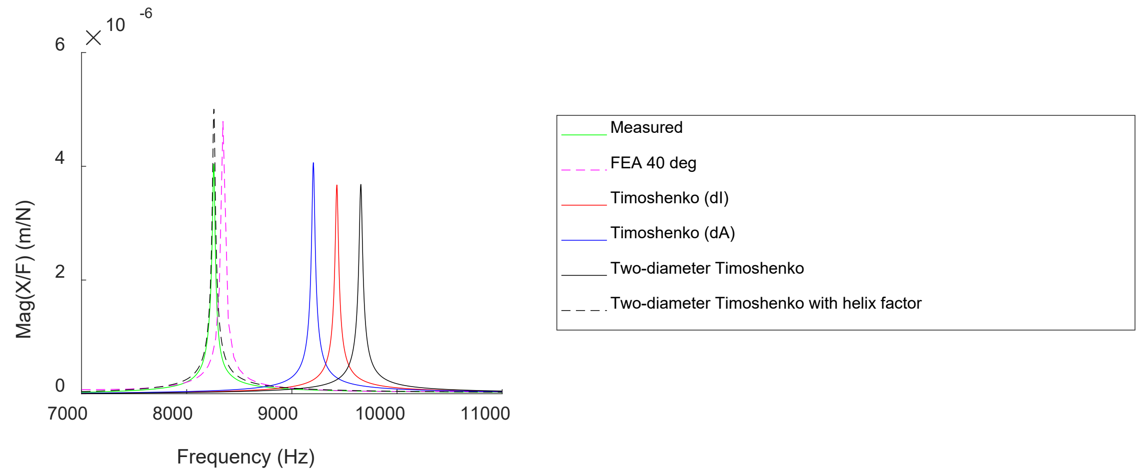

Figure 4-21. The measured receptance of the fluted section was compared to the predicted results from FEA, the single-diameter Timoshenko beam model results from area (magenta), single-diameter Timoshenko beam model results from second moment of area (red), the two-diameter Timoshenko beam model results without helix factor (solid black), and the two-diameter Timoshenko beam model results with helix factor (dashed black).

Table 4-7. Natural frequency and stiffness values for the receptances found via measurement, FEA, and Timoshenko beam models.

	Measured	**FEA**	**Single-diameter d_I**	**Single-diameter d_A**	**Two-diameter (no helix factor)**	**Two-diameter (with helix factor)**
Frequency (Hz)	8256.54	8407.4	9427.7	9204.2	9655.9	8259.3
% difference	-	1.8	14.2	11.5	16.9	0.0
Stiffness (N/m)	7.51 x10^7	6.15 x10^7	8.01E x10^7	7.29 x10^7	7.99 x10^7	5.87 x10^7
% difference	-	-18.2	6.7	-99.9	6.4	-21.8

The elastic modulus was selected to match the measured and predicted first bending mode natural frequency for the tool shank. Free-free boundary conditions were approximated by suspending the shank with soft elastic supports, Figure 4-16. The supports were located at the node points (zero displacement location) for the first bending mode to minimize their effect on the measured response. The FRF was measured using a PCB 086E80 modal hammer and a PCB 352C23 low mass accelerometer. The measured FRF is shown in Figure 4-17. Next, the receptance was predicted for a range of modulus values [500-620] GPa using the Timoshenko beam model for the solid cylindrical shank, Figure 4-18. A linear fit was used to describe the change in frequency with modulus Figure 4-19 and compared to the measured natural frequency. The best fit modulus for the tool shank was 578.7 GPa.

Next, the receptance of the fluted portion of the tool was measured using the same boundary conditions applied to the tool shank. The resulting FRF is shown in Figure 4-20.

The helix factor for the 12.7 mm, four flute tool with a 40° helix angle was determined as outlined in the previous section and found to be 0.66. The measured receptance of the fluted section was compared to the predicted results from FEA, the single-diameter Timoshenko beam model results from area (magenta), single-diameter Timoshenko beam model results from second moment of area (red), the two-diameter Timoshenko beam model results without helix factor (solid black), and the two-diameter Timoshenko beam model results with helix factor (dashed black). The resulting magnitude plots in Figure 4-21 show that the two-diameter Timoshenko method significantly outperforms the single-diameter methods, but that all prediction methods underpredict stiffness (i.e., the peaks are higher for the predicted FRFs). The natural frequencies and stiffness values for each of the methods are given in Table 4-7. The new two-diameter Timoshenko beam model with helix factor predicts the natural frequency of the twisted beam within 1%. The predicted stiffness from the two-diameter Timoshenko beam model with helix factor and FEA underpredict the measured stiffness by 21.8% and 18.1% respectively. The agreement of the two-diameter Timoshenko beam model with helix factor and FEA stiffness values to one another, however, indicates that additional stiffness effects may be present in the measured value due to the boundary conditions.

True Cross Section Comparison

In the previous section, a linear piecewise approximation of the four flute tool cross section was used. This study was expanded to use the exact cross section of the measured tool to evaluate effects of the linear approximation. The results are provided here.

To evaluate the true cross section, an image was taken of the tool at the EDM cut plane, and the photo was converted to a binary image, Figure 4-22. The x and y coordinates of points around the profile were determined using an image tracing function in MATLAB. The coordinates of the tool profile are shown in green in Figure 4-22. A comparison of the extracted cross section and the linear piecewise approximation is shown in Figure 4-23.

A comparison of the measured and predicted receptances is shown in Figure 4-24 and

Figure 4-25. The resulting natural frequencies and stiffness values are given in Table 4-8. Using the exact tool geometry improved the accuracy of the stiffness approximation by 4% versus the linear piecewise cross section approximation. This small difference in the two-diameter Timoshenko beam models indicates that reasonable accuracy for the receptance of the fluted portion of the tool can be achieved without using the exact tool cross section.

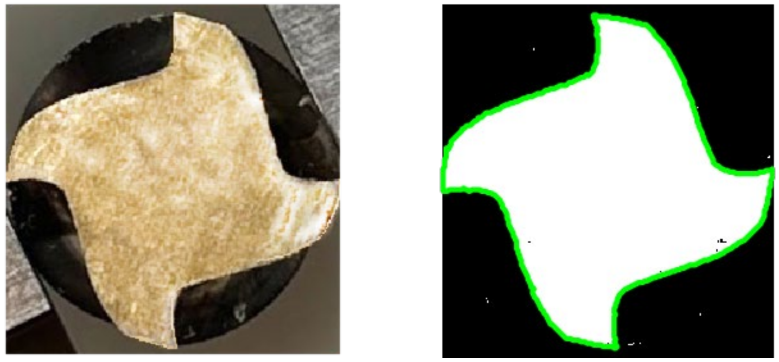

Figure 4-22. (Left) An image was taken of the tool cross section at the sectioned plane. (Right) The photo was converted to a binary image, and the points around the profile were identified using an image tracing function in MATLAB.

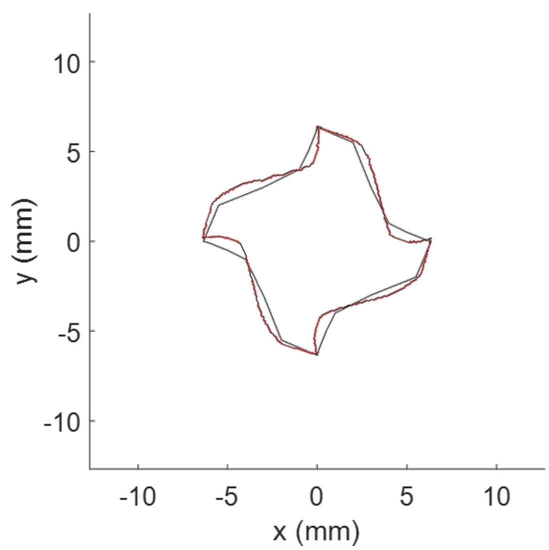

Figure 4-23. Comparison of the linear piecewise cross section approximation (black) and the actual profile (red) for a 12.7 mm diameter four flute tool.

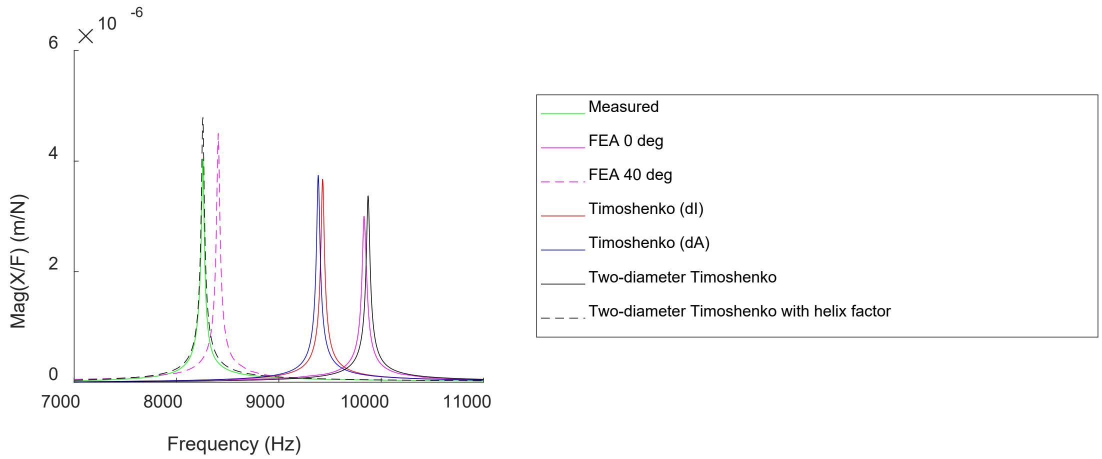

Figure 4-24. The measured and predicted FRFs using the single- and two-diameter Timoshenko beam models with and without the applied helix factor for the exact tool cross section.

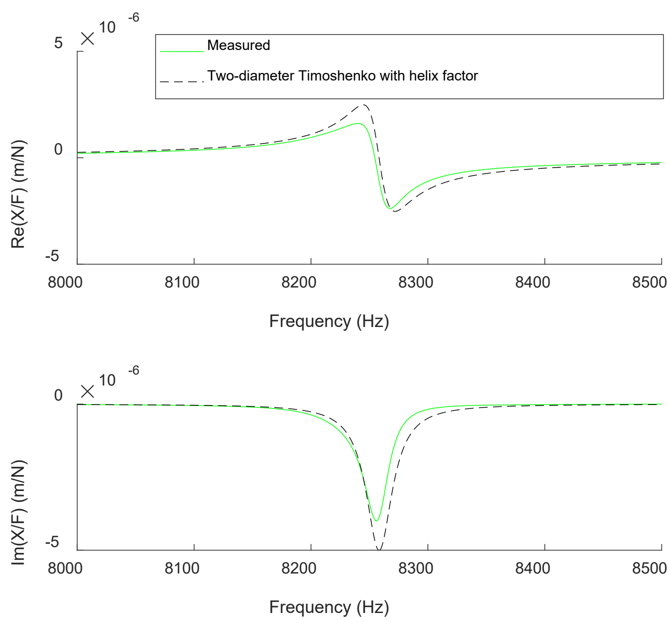

Figure 4-25. The measured and predicted FRFs using the two-diameter Timoshenko beam model with the helix factor. The model underpredicts the stiffness of the fluted geometry.

Table 4-8. Natural frequency and stiffness values for the receptances found via measurement, FEA, and Timoshenko beam models for the exact tool cross section.

	Measured	**FEA**	**Single-diameter d_I**	**Single-diameter d_A**	**Two-diameter (no helix factor)**	**Two-diameter (with helix factor)**
Frequency (Hz)	8256.54	8407.4	9626.7	9385.2	9872.9	8258.3
% difference	-	1.8	16.6	13.7	19.6	0.0
Stiffness (N/m)	$7.51 x 10^7$	$6.55 x 10^7$	$8.79 x 10^7$	$7.86 x 10^7$	$8.73 x 10^7$	$6.16 x 10^7$
% difference	-	-12.8	17.1	4.6	16.2	-17.9

Tool-Holder-Spindle-Machine Receptance

Set Screw Holders

Set screw holders are an economical tool holding solution which require little setup time and a single torque wrench, typically with a hex or Torx attachment. In this arrangement, a set screw mates with a Weldon flat which has been ground on the tool shank as shown in Figure 4-26. This positive mechanical engagement results in higher axial pullout resistance versus collet type holders. However, because the tool is being pushed against one side of the holder by the set screw, runout is typically higher than radial clamping designs such as collet, hydraulic, or heat-shrink holders [192]. For each setup, the tool was inserted into the holder and a set screw torque of 47.5 N-m was applied with a torque wrench. A Makino a51nx milling machine was used for all in-spindle testing.

Spindle-Machine Receptance

An artifact was selected, clamped in the tool spindle, and the receptances in the x and y directions were measured by impact testing using a modal hammer (PCB 086C04) and low mass accelerometer (PCB 352C23) as shown in Figure 4-27. For these tests, an artifact with a cylindrical, hollow extension beyond the flange was selected. The artifact dimensions are provided in Figure 4-28. The resulting receptance is shown in Figure 4-29.

Inverse RCSA was then used to remove the effects of the artifact from the measurement to isolate the spindle-machine dynamics. Because the geometry of the holder from the front of the flange to the retention knob is the same for all holders using a CAT-40 interface, only the cylindrical portion of the artifact is required to be removed (in simulation). Additionally, because the flange-taper geometry and contact stiffness/damping between the holder external taper and spindle internal taper are captured in the measured artifact-spindle-machine dynamics, additional coupling parameters for the holder-spindle interface do not need to be identified. The isolated spindle-machine receptance is shown in Figure 4-30.

Coupling Parameter Identification

For the tool-holder coupling parameter identification, the required stiffness and damping parameters for the RCSA algorithm were determined by inserting a solid carbide rod in the tool holder and inserting the combination in the selected spindle-machine. A carbide blank of each tested tool diameter [12.7, 15.875, 19.05] mm was assembled into the appropriate holder to form a tool-holder assembly. Each tool-holder configuration was clamped in the spindle of a Makino a51-nx and the tool tip receptances were measured as shown in Figure 4-31.

To model the tool tip receptance, each of the holders and embedded shanks were first modeled as a series of discretized Timoshenko beam elements as shown in Figure 4-32. The (steel) holder is shown in grey and the (carbide) rod shank is shown in red. The holder dimensions are given in Table 4-9, where the holder internal diameter for each section was set equal to the diameter of the inserted carbide rod. Each holder was modeled using fifteen Timoshenko elements which were then rigidly coupled using RCSA. The holder receptances were then rigidly coupled to the previously archived spindle-machine receptance to form a holder-spindle-machine receptance.

Second, this process was repeated for each of the carbide blanks to predict the tool receptance. The dimensions of the blanks are given in Table 4-10. The stickout (or extension) length for each rod was measured using calipers as shown in Figure 4-33.

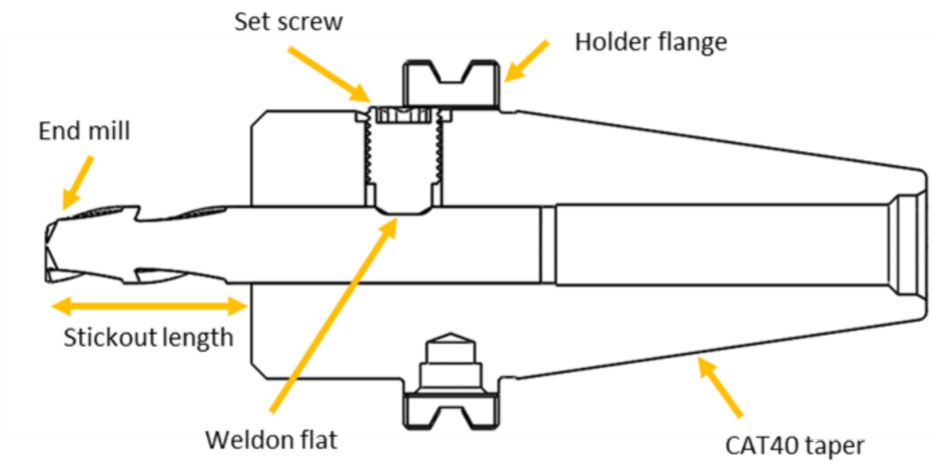

Figure 4-26. The cross-sectional view of a set screw holder. The set screw clamps against a Weldon flat, which is ground on the tool shank, to secure the tool in the holder.

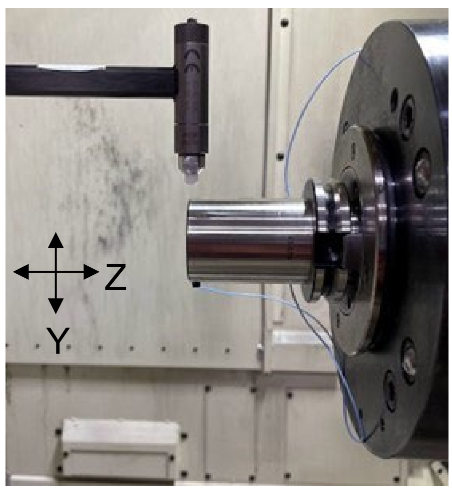

Figure 4-27. The artifact-spindle-machine receptances are measured for each machine spindle in the x and y directions. Inverse RCSA is used to remove the effects of the portion of the artifact extending past the flange to isolate the spindle-machine dynamics.

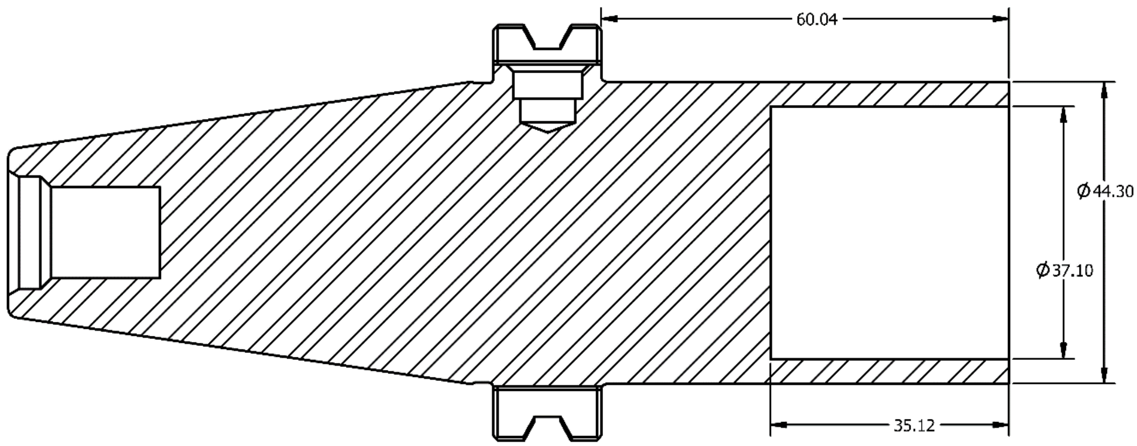

Figure 4-28. The dimensions (in mm) of the artifact.

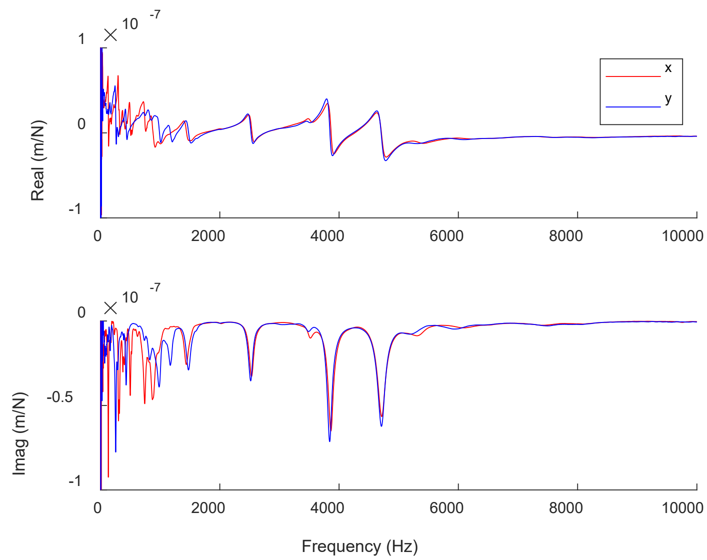

Figure 4-29. Direct receptances of the artifact-spindle-machine in the *x* and *y* directions.

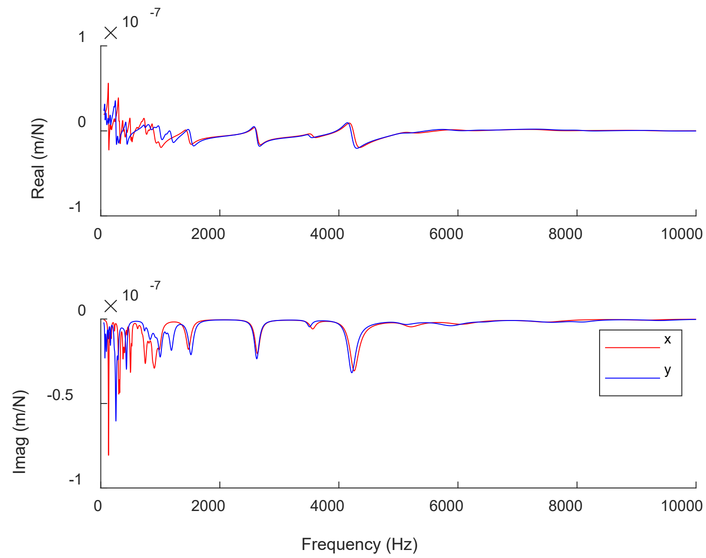

Figure 4-30. The isolated spindle-machine receptances in the *x* and *y* directions.

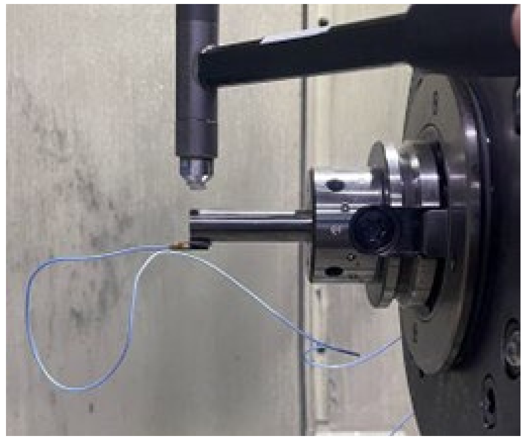

Figure 4-31. Tool-holder-spindle-machine receptances were measured by impact testing using a modal hammer and low mass accelerometer to determine the tool-holder coupling parameters.

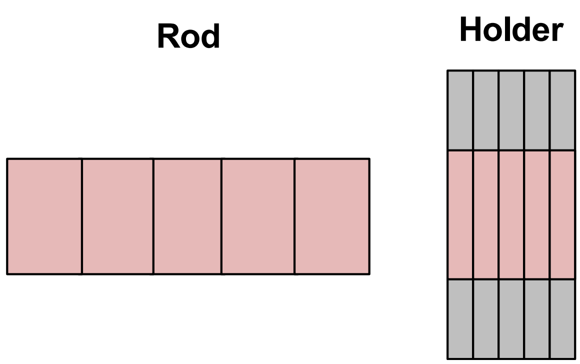

Figure 4-32. The holder and carbide rod are modeled independently as a series of Timoshenko beam elements. The steel holder is shown in grey, and the carbide rod is shown in red. These substructures are then coupled with a flexible connection.

Figure 4-33. Calipers were used to measure the stickout length of each carbide rod and tool.

Table 4-9. Tool holder segment dimensions.

Nominal holder size/ internal diameter (mm)	12.7	15.875	19.05
Length (mm)	25.4	25.4	25.4
Outer diameter (mm)	44.45	44.45	44.45

Table 4-10. Carbide rod dimensions.

Diameter (mm)	**Overall length (mm)**	**Stickout length (mm)**
12.7	102.80	44.30
15.875	115.60	52.38
19.05	128.37	66.64

Table 4-11. Connection parameters for each carbide rod-holder combination.

Diameter (mm)	**$k_{\theta f}$ (N/rad)**	**$c_{\theta f}$ (Ns/rad)**
12.7	2.68×10^6	0.25
15.875	4.88×10^6	1.75
19.05	5.95×10^6	8.5

Third, the tool and holder-spindle-machine were coupled using a flexible connection with connection parameters $k_{\theta f}$ and $c_{\theta f}$ as described in Chapter 3. These connection parameters were selected to provide a visual best fit between the RCSA predicted receptance and the measured receptance. The resulting fits are shown in Figure 4-34 through Figure 4-36 for the 12.7 mm, 15.875 mm, and 19.05 mm diameter rods respectively. The resulting connection parameters in both the x and y direction for each tool are given in Table 4-11.

Tool-Holder-Spindle-Machine Receptance Validation

To validate the new two-diameter Timoshenko beam model with helix factor, the tool-holder-spindle-machine receptances predicted using RCSA were compared to measured tool tip FRFs. Measurements were completed by impact testing using a modal hammer (PCB 086C04) and low mass accelerometer (PCB 352C23) adhered to the tool tip using wax. Tests were completed for: 1) a 12.7 mm diameter, four flute endmill; 2) a 15.875 mm, four flute endmill; and 3) a 19.05 mm, three flute endmill as show in Figure 4-37.

Nomenclature for the tool-holder assembly is shown in Figure 4-38. For each end mill geometry, the fluted portion of the tool was described using the two-diameter Timoshenko beam model. The relieved section and shank were described by the measured diameter. The stickout length was measured as shown in Figure 4-33 and the flute length was set to the manufacturer specifications. The helix factor was calculated as a function of the diameter, number of flutes, helix angle, and length to diameter ratio using the coefficients presented in Appendix B. The measured dimensions and calculated d_I, d_A, and helix factor, F, for each of the tested tools are presented in Table 4-12.

In the RCSA algorithm, tool segments are rigidly coupled to the adjacent section along the tool axis. Similarly, holder segments are rigidly coupled to adjacent holder segments along the holder axis. The identification of the linear stiffness and viscous damping coupling terms used to describe the interface between the tool and holder was discussed in Coupling Parameter Identification. To predict each tool-holder-spindle-machine receptance, the coupling terms for the same size tool shank diameter were selected (i.e., the coupling parameters identified for the 12.7 mm diameter carbide blank were used to predict the receptance of the 12.7 mm diameter tool).

The RCSA predicted receptances using the new two diameter model (blue) are compared to the measured tool tip FRFs for all three tools, Figure 4-39. The percent difference in predicted natural frequency is less than 2% in all cases. However the disagreement in the dynamic stiffness (peak height) for the 12.7 mm and 19.05 mm diameter tools is larger. This is attributed to the presence of spindle modes near the natural frequency of the tool which causes dynamic interactions similar to a dynamic absorber.

The measured tool tip receptance and two-diameter Timoshenko beam model results were then compared to the area and second moment of area single-diameter Timoshenko beam model results. Figure 4-40 through Figure 4-42 show that for all three tested cases, the two-diameter Timoshenko beam model predicts the natural frequency within 2% and most closely matches the stiffness.

Milling Stability

In this section, the application of the proposed two-diameter Timoshenko beam model to predict the tool tip receptance and, subsequently, the milling stability is evaluated. The tool tip receptance predicted by RCSA was used to generate a stability map using the Fourier series approach for a 15.9 mm diameter tool with four flutes and a 52.30 mm stickout length. First, the tool tip receptance was predicted as described in the section titled Helix Angle and Length to Diameter Ratio. Second, the tool-workpiece cutting force coefficients were measured. Third, a grid of cutting tests was completed for various spindle speed and axial depth of cut combinations to compare with the predicted stability map.

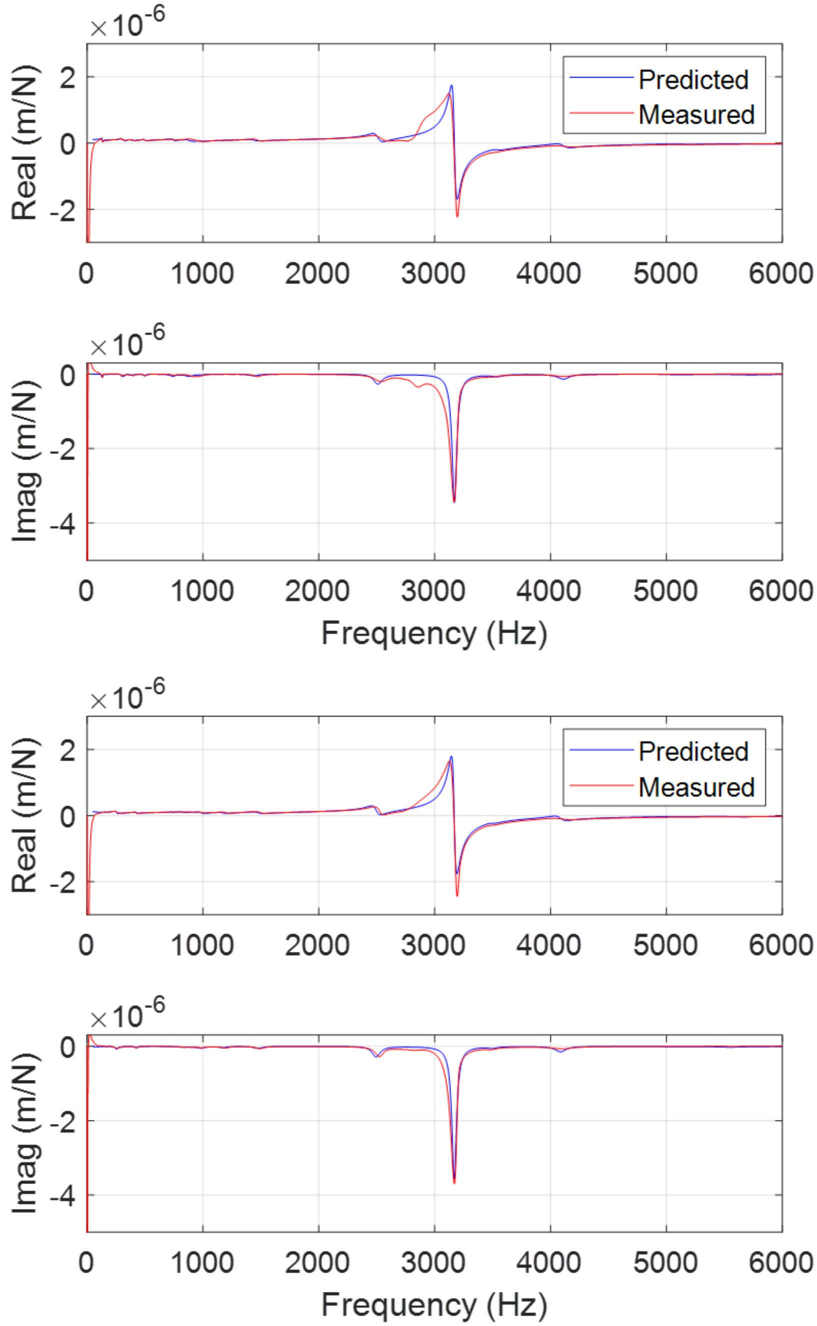

Figure 4-34. RCSA fit for 12.7 mm diameter carbide rod. Top: *x* direction. Bottom: *y* direction.

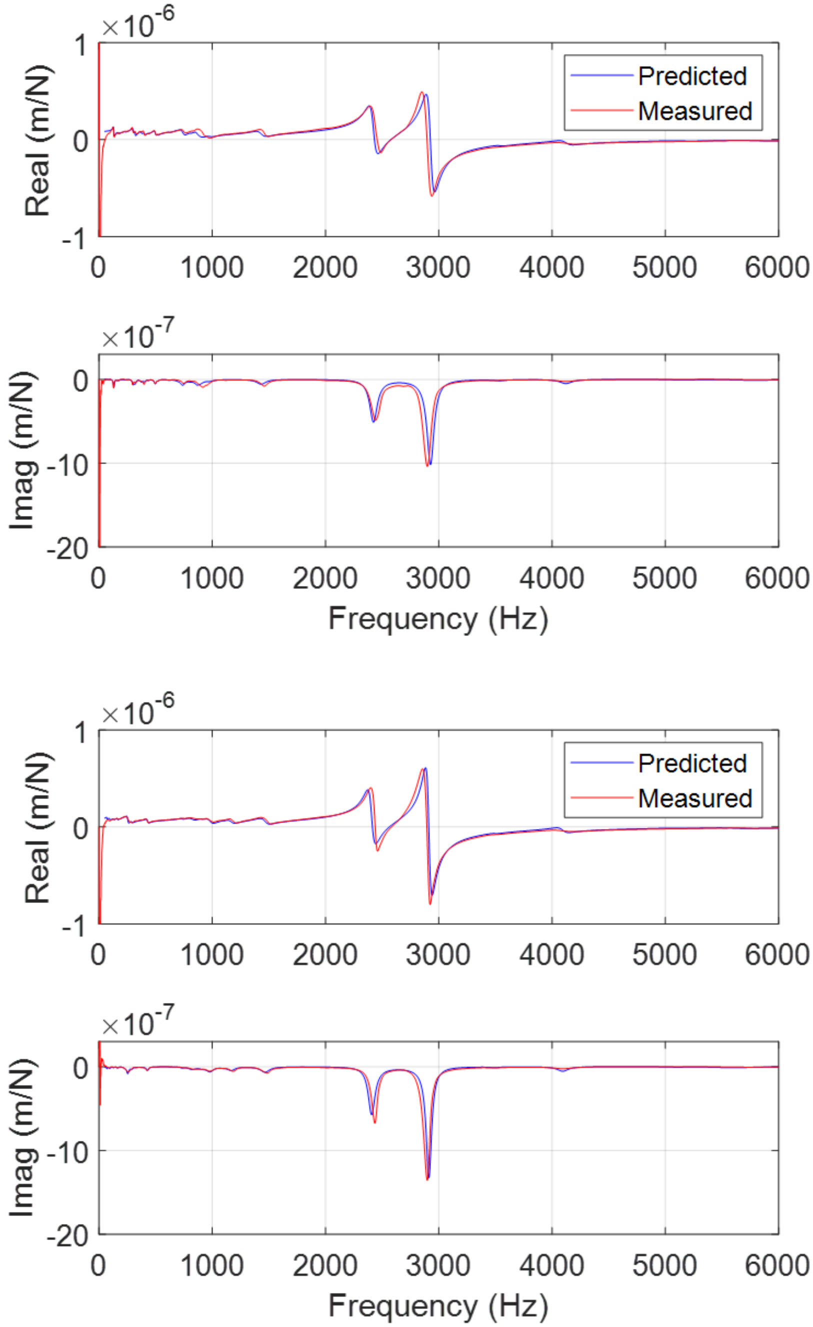

Figure 4-35. RCSA fit for 15.875 mm diameter carbide rod. Top: *x* direction. Bottom: *y* direction.

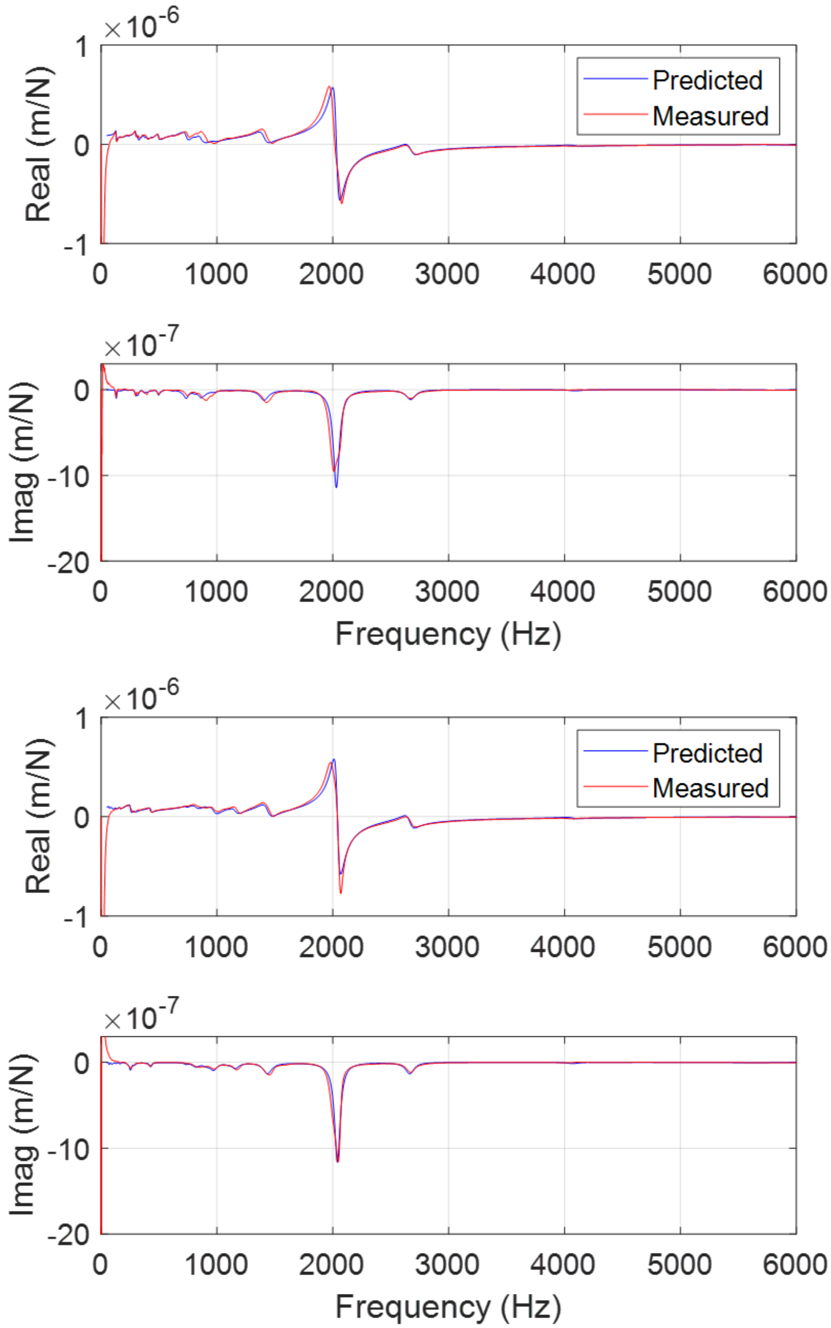

Figure 4-36. RCSA fit for 19.05 mm diameter carbide rod. Top: *x* direction. Bottom: *y* direction.

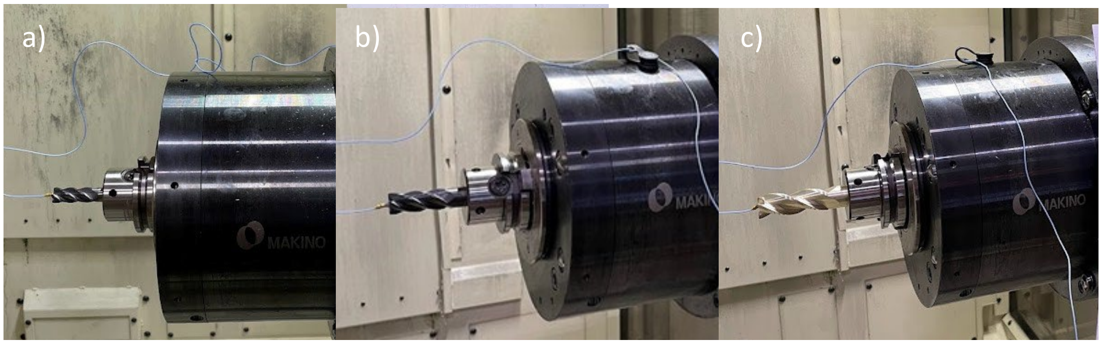

Figure 4-37. The tool tip receptance of a) 12.7 mm, b) 15.875 mm, and c) 19.05 mm diameter endmills were measured by impact testing.

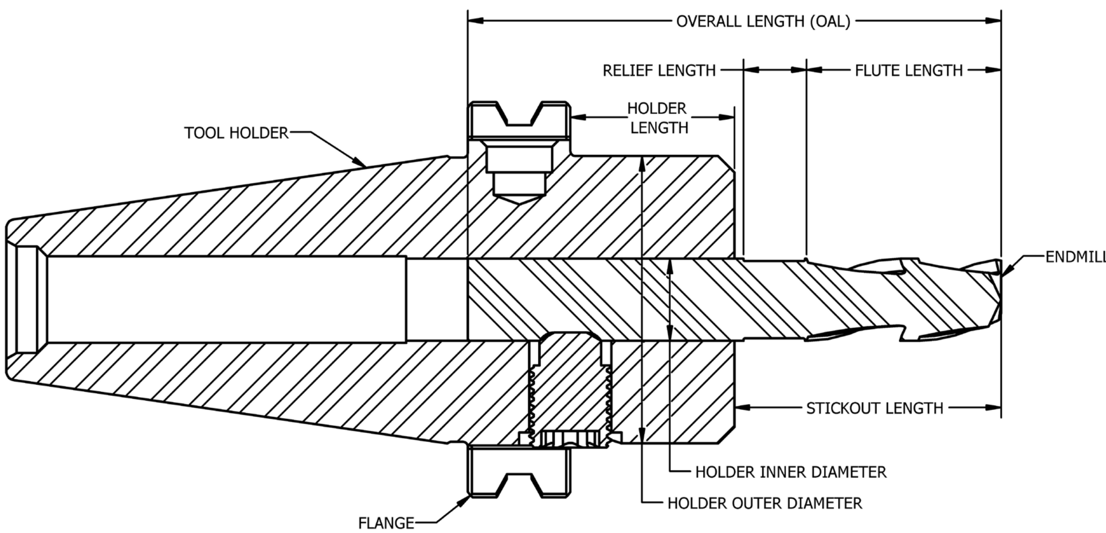

Figure 4-38. Nomenclature for tool holder and endmill measurements.

Table 4-12. Dimensions and modeling inputs for the 12.7 mm, 15.875 mm, and 19.05 mm endmills.

Nominal diameter (mm)	Flutes	Helix angle (deg)	Stickout length (mm)	Flute length (mm)	Relief length (mm)	Relief diameter (mm)	d_I (mm)	d_A (mm)	F (-)
12.7	4	38	44.44	31.75	9.53	12.10	10.14	9.88	0.93
15.875	4	38	52.30	38.10	12.70	15.18	12.68	12.35	0.93
19.05	3	37	66.05	50.80	15.88	18.19	13.57	12.97	0.95

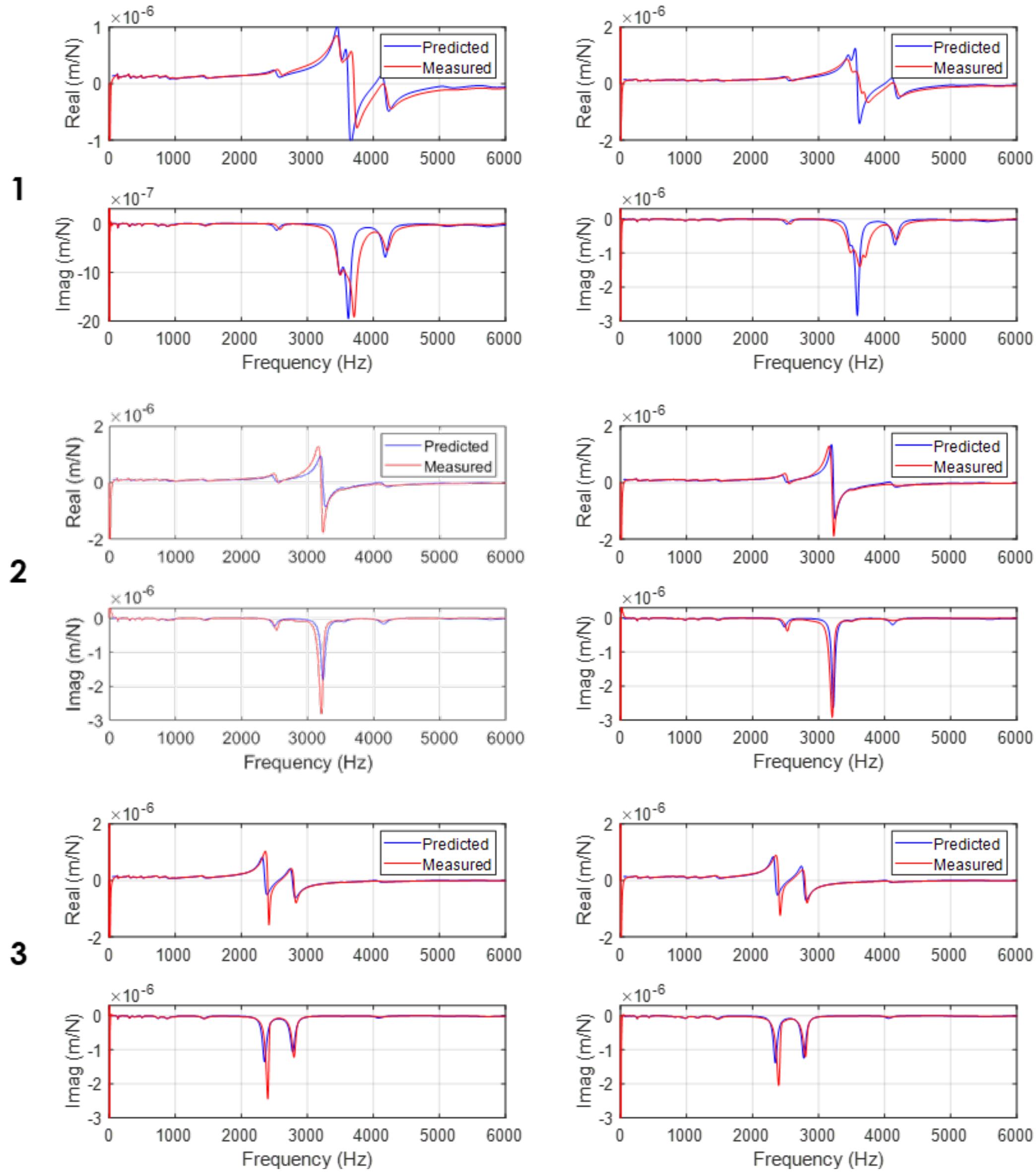

Figure 4-39. The predicted tool tip receptances using RCSA and the new two-diameter Timoshenko beam model with helix factor are compared to impact testing measurements collected for 12.7 mm (row 1), 15.875 mm (row 2), and 19.05 mm (row 3) diameter endmills in the *x* (left column) and *y* (right column) directions.

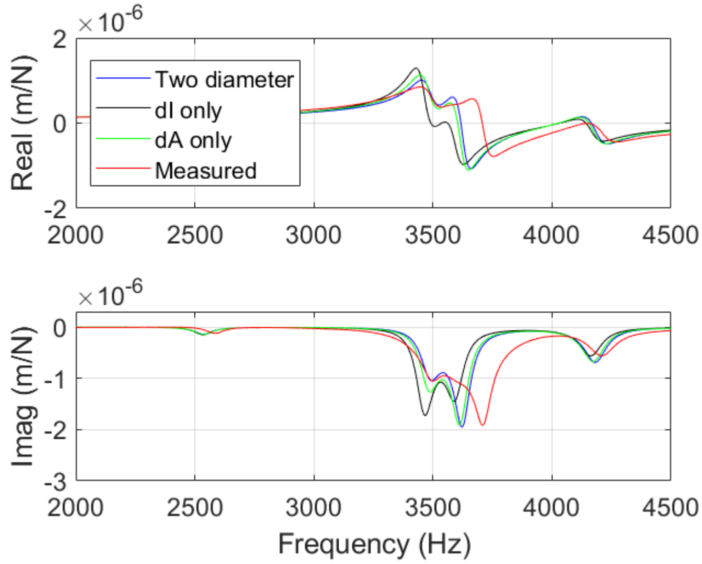

Figure 4-40. Comparison of the tool-holder-spindle-machine receptance predicted by RCSA and measured tool tip FRF for a 12.7 mm diameter, four flute endmill.

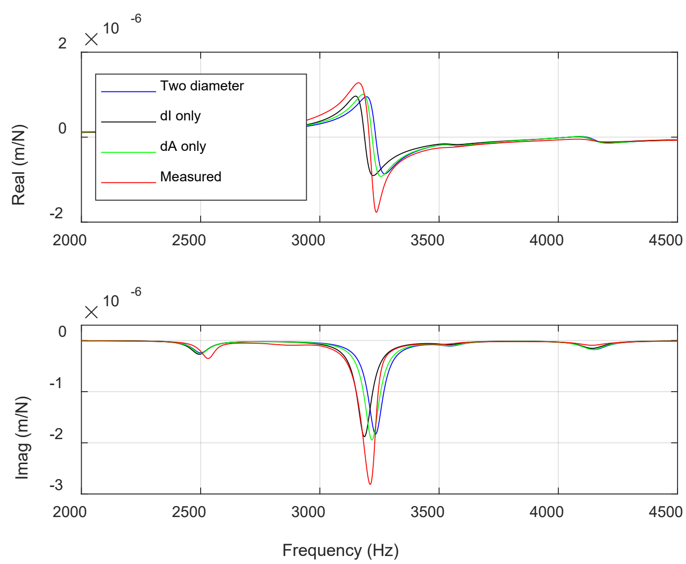

Figure 4-41. Comparison of the tool-holder-spindle-machine receptance predicted by RCSA and measured tool tip FRF for a 15.875 mm diameter, four flute endmill.

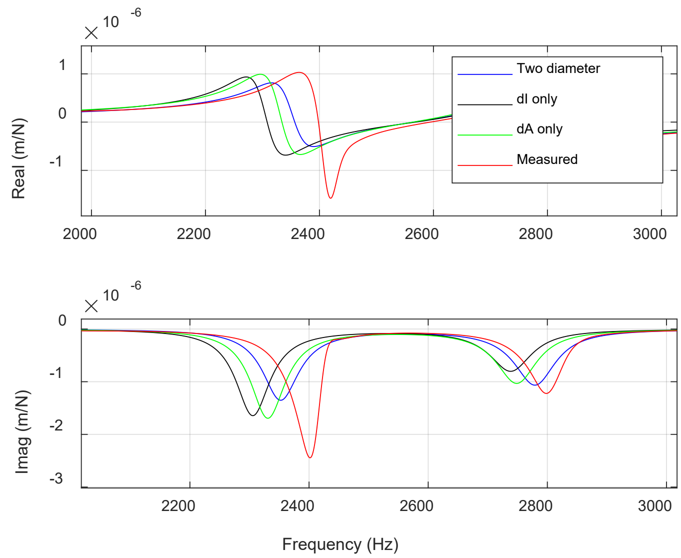

Figure 4-42. Comparison of the tool-holder-spindle-machine receptance predicted by RCSA and measured tool tip FRF for a 19.05 mm diameter, four flute endmill.

Experimental Determination of Cutting Force Coefficients

To predict the stability map, both the tool tip receptances and cutting force model are required. The cutting force coefficients are tool-workpiece specific. Therefore, the normal, tangential, and axial cutting force coefficients as well as the edge coefficients were measured. For continuity, tests for stability and determination of cutting force coefficients were completed using the same workpiece.

Tests to measure cutting force coefficients were completed on a Kistler 9257B cutting force dynamometer at 50% radial immersion as shown in Figure 4-43 and Figure 4-44. Forces were collected in the x (feed), y, and z directions. Five feed per tooth values [0.050 0.075 0.100 0.125 0.150] mm/tooth were selected, and three repeats were collected at each feed per tooth value. A spindle speed- axial depth combination was selected such that all cuts were stable. Tests were completed at 8000 rpm with an axial depth of cut of 5.1 mm. Cuts were performed in a down milling (climb milling) orientation.

To extract the six cutting force coefficients, the average of the force signal in each direction was calculated over the range of selected feedrates. The linear regression method described in Chapter 3 was then used to determine the coefficients k_n, k_t, k_a, k_{ne}, k_{te}, and k_{ae} using the slope and intercept of the best fit lines to the feed per tooth-mean force data.

For the x, y, and z axis forces measured by the force dynamometer, the average of three cuts was used to calculate the force in each direction and the resulting cutting force coefficients as shown in Figure 4-45. Results for the cutting force coefficients are given in Table 4-13.

To determine an uncertainty in the cutting force coefficients, one of the three tests was sampled at random for each feedrate and the linear regression was completed. The slope and intercept were then used to calculate the coefficients. This process was repeated for 150 iterations and the mean and standard deviation for the coefficients for the distributions were calculated. The 95% confidence interval (two standard deviations) is reported in Table 4-13, where σ is one standard deviation of the coefficient over all iterations.

The cutting force coefficients were used in a time domain simulation [3] and compared to the measured forces to verify the linear fit. Inputs to the time domain simulation include the tool diameter, corner radius, number of teeth, helix angle and runout, in addition to the spindle speed and feedrate. Runout was measured as [0 -8.89 -15.24 -5.08] µm using a dial indicator as shown in Figure 4-46. For all cutting tests, the forces were filtered to remove the effects of the dynamometer dynamics on the measured force [193]. Results for the four flute, 15.875 mm diameter endmill with a spindle speed of 8000 rpm and feedrate of 0.05 mm/tooth and 0.15mm/tooth are shown in Figure 4-47 and Figure 4-48 respectively . TDS is the time domain simulation, $F_{x/y}$ is the raw force signal in the *x/y* direction, and $F_{x/y}$ filtered is the filtered force signal in the *x/y* direction.

Stability Validation

Stability testing was conducted on a Makino a51nx with an aluminum 6061-T6 workpiece. A feed per tooth of 0.1 mm and 50% radial immersion was commanded, and a grid of spindle speed-axial depth of cut combinations were tested. The range of spindle speeds was 8000 rpm to14000 rpm in 1000 rpm increments. The starting axial depth of cut was 1 mm and was increased by 1 mm until an unstable cut was completed.

To determine stability, the cutting sound was measured using a microphone located next to the machine door, Figure 4-49. The fast Fourier transform (FFT) of the audio signal was used to transform from the time domain to the frequency domain. The tooth passing frequency for each test was calculated by:

$$f_{tooth} = \frac{\Omega N_t}{60} \tag{4.5}$$

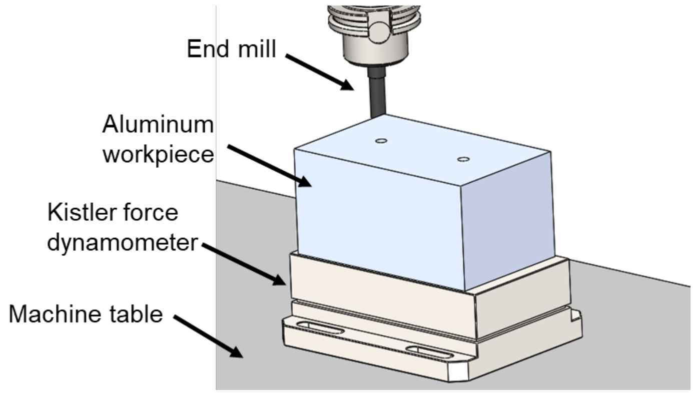

Figure 4-43. Machine setup for cutting force measurements using Kistler 9257B cutting force dynamometer.

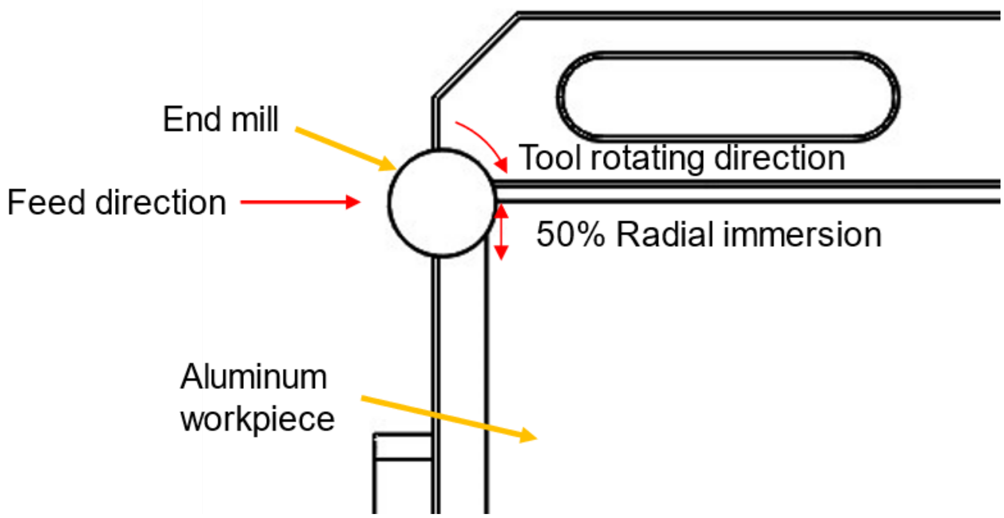

Figure 4-44. Cutting force coefficients were collected at 50% radial immersion in a down milling direction for all cuts.

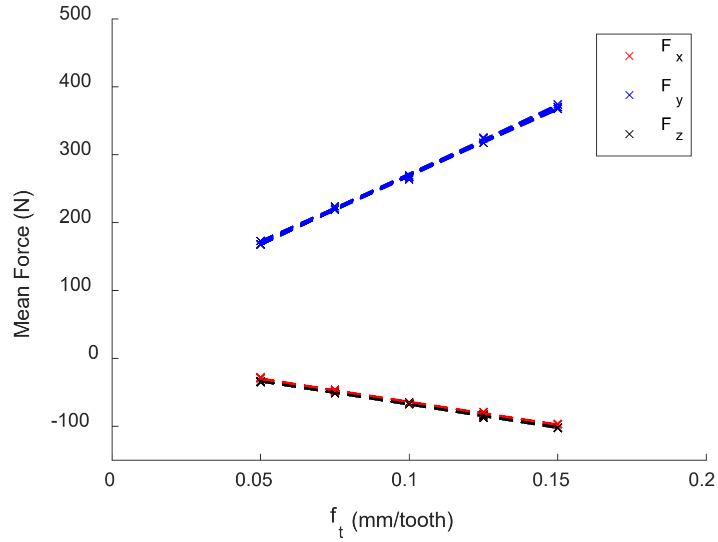

Figure 4-45. The mean force and linear fit for a 15.875 mm endmill tested over five feedrates at 8000 rpm.

Figure 4-46. Runout of the tool was measured using a dial indicator.

Table 4-13. Measured cutting force coefficients and uncertainty.

	k_n (N/mm^2)	k_t (N/mm^2)	k_a (N/mm^2)	k_{ne} (N/mm)	k_{te} (N/mm)	k_{ae} (N/mm)
Measured	168.89	684.81	210.80	11.25	10.04	0.08
2σ	16.53	16.78	7.02	1.30	0.85	0.47

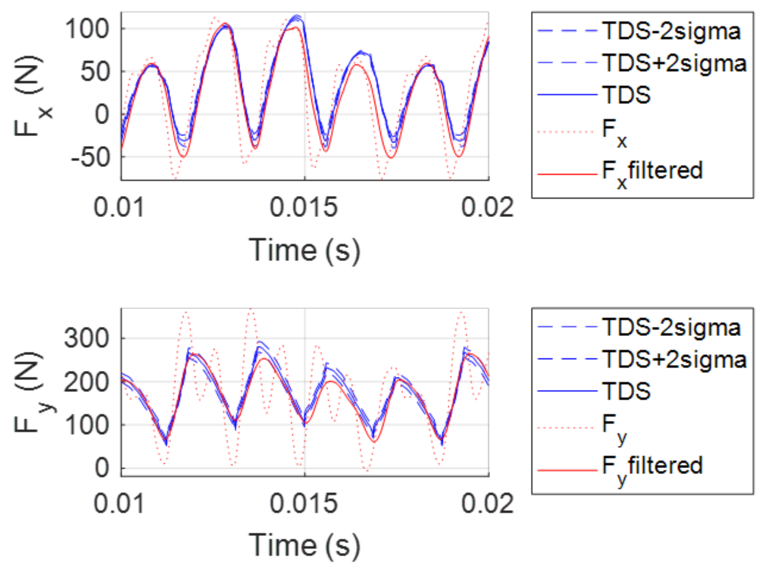

Figure 4-47. Time domain simulation versus measured forces for a 15.875 mm endmill with a spindle speed of 8000 rpm and feedrate of 0.05 mm/tooth.

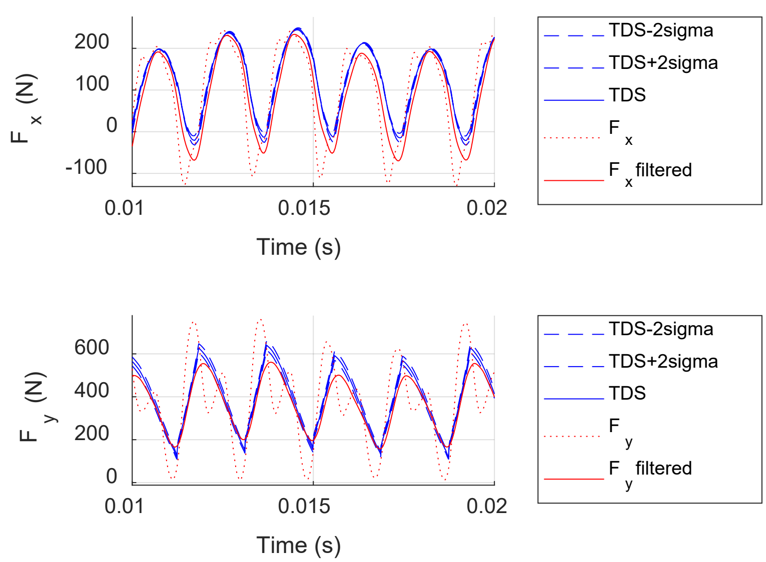

Figure 4-48. Time domain simulation versus measured forces for a 15.875 mm endmill with a spindle speed of 8000 rpm and feedrate of 0.15 mm/tooth.

where f_{tooth} is the tooth passing frequency in Hertz, Ω is the spindle speed in revolutions per minute (rpm), and N_t is the number of flutes on the tool. In the case of a stable cut, frequency content should be present only at the tooth passing frequency and its integer multiples. In an unstable cut, peaks in the frequency plot occur at a chatter frequency which is not a multiple of the tooth passing frequency, in general. Examples of stable and unstable results are shown in Figure 4-51 and

Figure 4-52. The resulting stability grid is shown in Figure 4-53.

A stability map was first generated using the measured tool tip FRF, Figure 4-54. Propagating the 2σ uncertainty in cutting force coefficients yielded little variation in the predicted stability boundary.

Stability maps were generated using the receptance from impact testing of the tool (red), and RCSA models using the two-diameter Timoshenko beam model with helix angle factor (blue), beam model using a single-diameter derived from the second moment of area (black), and beam model using a single-diameter derived from cross-sectional area (green), Figure 4-55. When compared to the measured stability grid, as shown in Figure 4-56, the two-diameter Timoshenko beam model approach most closely matches the stability boundary. All predicted stability maps are slightly shifted with respect to the tests collected at 10,000 rpm.

Figure 4-49. For each stability test, the cutting sound was recorded and was stability determined by frequency content.

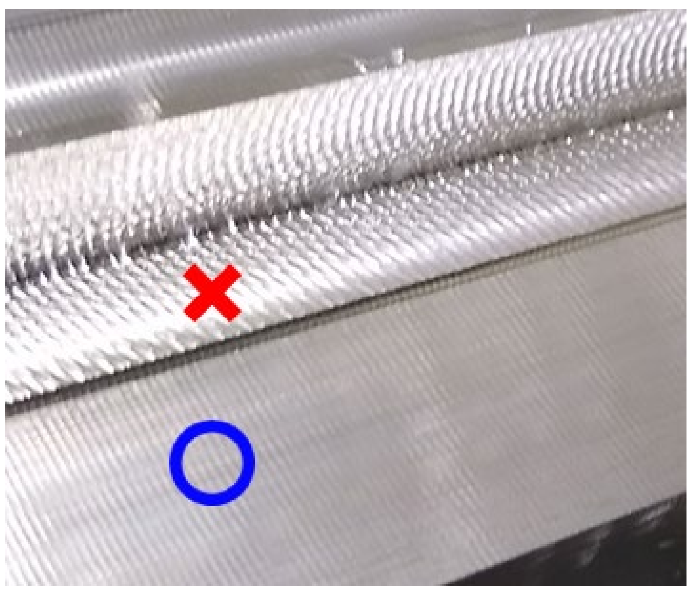

Figure 4-50. Examples of the surface left behind due to unstable (red X) and stable (blue O) combinations of spindle speed and axial depth of cut.

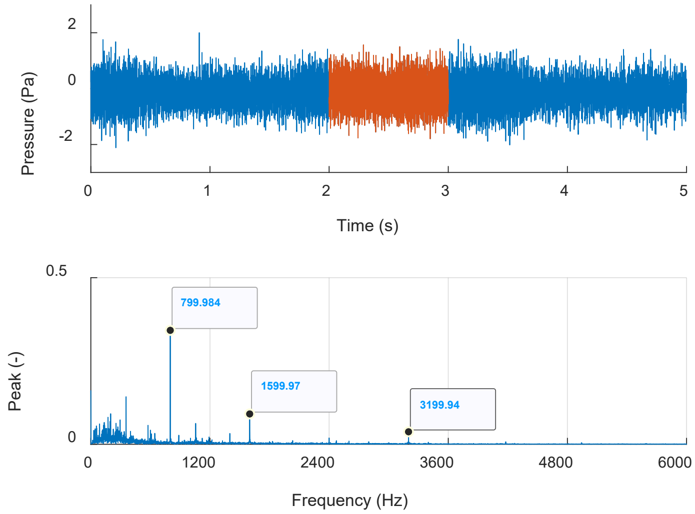

Figure 4-51. A stable cut using a 15.875 mm diameter four flute end mill at 12000 rpm and 3 mm axial depth of cut. The tooth passing frequency is 800 Hz.

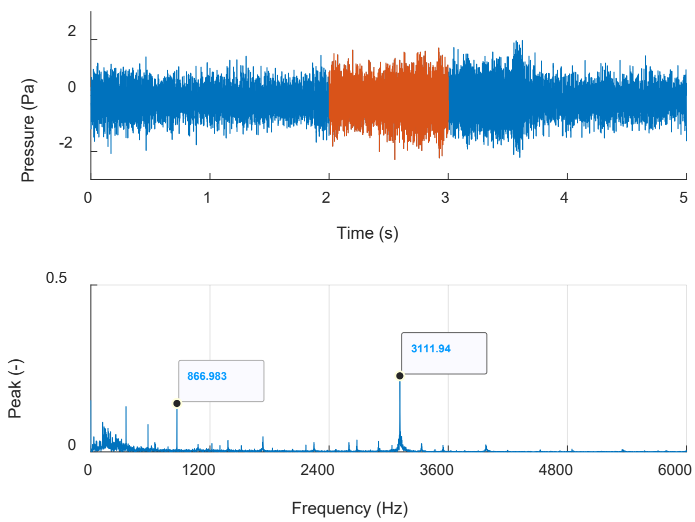

Figure 4-52. An unstable cut using a 15.875 mm diameter four flute end mill at 13000 rpm and 3 mm axial depth of cut. The tooth passing frequency is 867 Hz. Content present at 3112 Hz indicates chatter as this is not an integer multiple of 867 Hz.

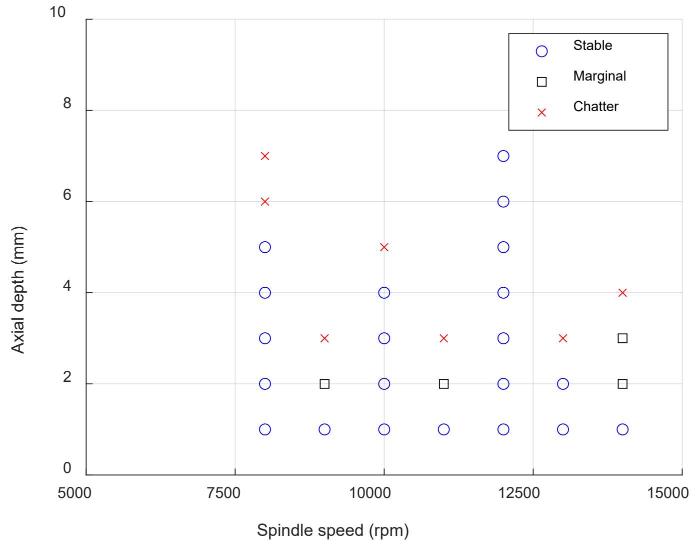

Figure 4-53. Stability results for 15.875 mm diameter four flute endmill with 50% radial immersion.

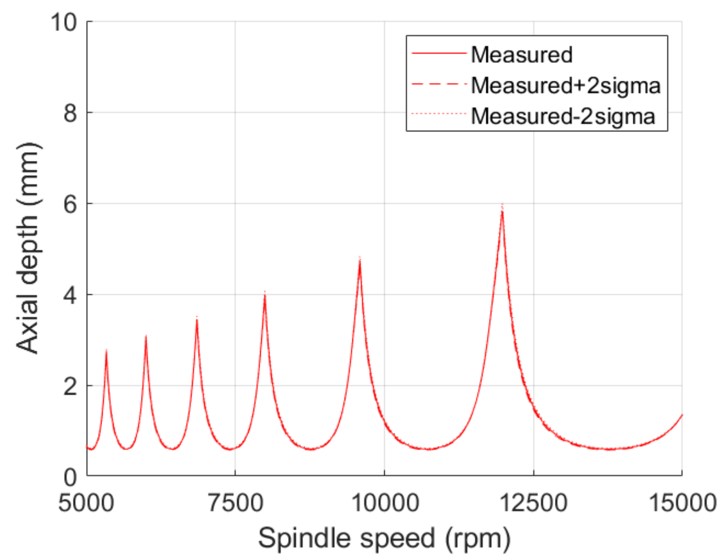

Figure 4-54. The stability map predicted using the measured tool tip receptance with uncertainty in the measured cutting force coefficients.

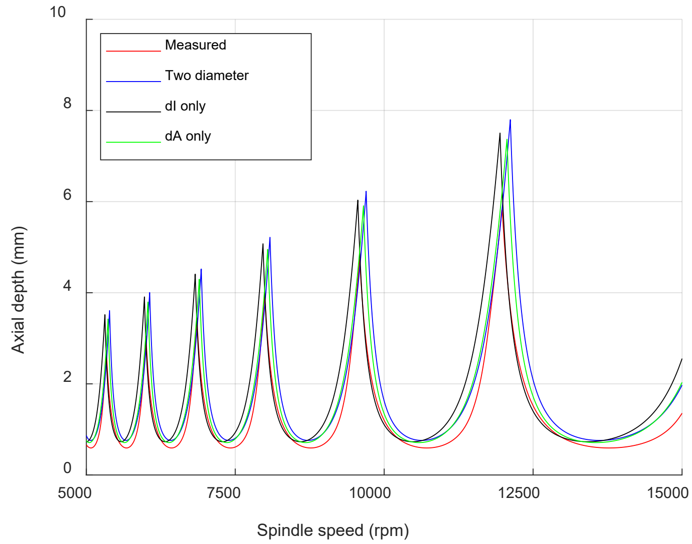

Figure 4-55. The stability lobe map predicted using the measured and predicted tool tip receptances for the two-diameter and single-diameter Timoshenko beam models.

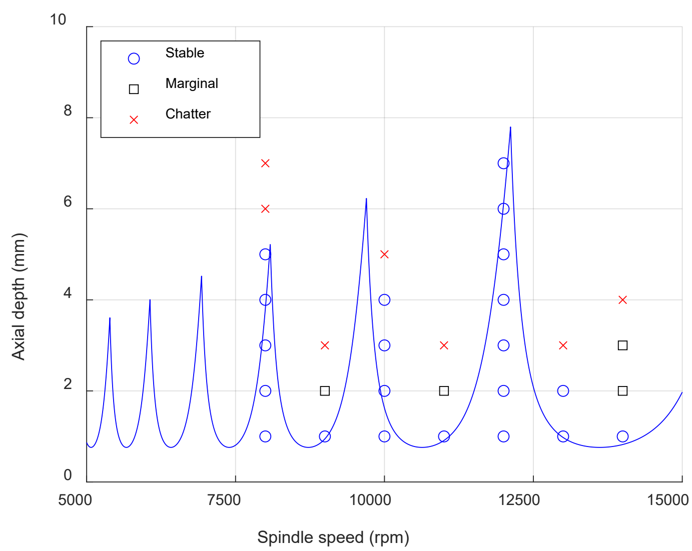

Figure 4-56. The stability map predicted from the two-diameter Timoshenko beam model for the tool tip receptance prediction. The milling test results are also shown.

CHAPTER FIVE
CONCLUSIONS AND FUTURE WORK

Receptance coupling substructure analysis (RCSA) using the two-diameter Timoshenko beam model provides a computationally inexpensive, modeling-based method for predicted the receptances for the fluted portions of helical endmills and, subsequently, the tool tip receptance of the tool-holder-spindle-machine combination. This process reduces the need for expensive and time-consuming measurements to be made at the machine for individual tool-holder-spindle-machine combinations. RCSA enables stability maps to be predicted and therefore the improved selection of milling parameters for increased material removal rates. The development of the two-diameter Timoshenko beam model and integration of a helix factor improve the accuracy of the RCSA method.

This low-cost technology has applications in both small machine shops, where the time, capital, and expertise to conduct an impact test is limited or nonexistent, and large manufacturing environments, where tens of tools may be used to produce a single component or machining cells are used to produce large batches of parts. In either case, increased efficiency in the use of the machine tool, provided by the selection of optimized parameters, results in cost savings for the manufacturer.

As demonstrated in this work, the key inputs to the RCSA model are:

- The spindle-machine receptance, which is determined from an artifact measurement for each machine tool.
- The tool holder receptance, which is modeled using a series of (single-diameter) Timoshenko beam elements.
- The endmill receptance
- Coupling coefficients that are used to represent the non-rigid connection between the endmill (tool) and tool holder.

The aim of this dissertation was to demonstrate a new two-diameter Timoshenko beam model to predict the receptance of the fluted portion of the tool. A model was presented which accounts for the stiffness and mass of the tool by considering the second moment of area and area using the tool cross section. The influence of the helix angle and length to diameter ratio were incorporated in the model.

The increased accuracy of the two-diameter Timoshenko beam model compared to the single-diameter Timoshenko beam model was demonstrated for a variety of flute counts, diameters, and lengths. A dependence on tool helix angle was incorporated for the first time. The predicted receptance from the two-diameter Timoshenko beam model was used to accurately predict the tool-holder-spindle-machine receptances using RCSA for three different tool assemblies. Finally, the proposed method was used to accurately describe the milling stability boundary.

Future Work

Wide scale adoption and application of milling parameter selection by RCSA may be possible through integration of the algorithm within existing computer aided manufacturing (CAM) programs. In commercial CAM software, libraries of tools are generated which contain geometric information about the tool holder, diameter, length, number of flutes, and helix angles. The machine tool on which a program will be executed is also selected in the software. Currently, however, the tool-holder-spindle-machine combination is considered rigid. RCSA provides a method to incorporate the structural dynamics, in addition to the geometry, into parameter selection at the CAM stage in the production cycle.

Future efforts will include establishing a catalog of coupling parameters used to describe the flexible connection between the tool and holder. When combined with the new the two-diameter Timoshenko beam model and method to measure and archive spindle-machine receptances, a robust RCSA solution will be provided that can assist the CAM programmer at the point of need.

REFERENCES

[1] J. Tlusty, W. Zaton, and F. Ismail, “Stability Lobes in Milling,” *CIRP Ann.*, vol. 32, no. 1, pp. 309–313, Jan. 1983, doi: 10.1016/S0007-8506(07)63411-8.

[2] Y. Altintas and E. Budak, “Analytical Prediction of Stability Lobes in Milling,” *CIRP Ann.*, vol. 44, no. 1, pp. 357–362, Jan. 1995, doi: 10.1016/S0007-8506(07)62342-7.

[3] T. L. Schmitz and K. S. Smith, *Machining Dynamics*, 2nd ed. Cham: Springer International Publishing, 2019. doi: 10.1007/978-3-319-93707-6.

[4] M. V. Junior, E. A. Baptista, L. Araki, S. Smith, and T. Schmitz, “The role of tool presetting in milling stability uncertainty,” *Procedia Manuf.*, vol. 26, pp. 164–172, Jan. 2018, doi: 10.1016/J.PROMFG.2018.07.023.

[5] T. L. Schmitz, T. J. Burns, J. C. Ziegert, B. Dutterer, and W. R. Winfough, “Tool length-dependent stability surfaces,” *Mach. Sci. Technol.*, vol. 8, no. 3, 2004, doi: 10.1081/MST-200038989.

[6] T. J. Burns and T. L. Schmitz, “Receptance coupling study of tool-length dependent dynamic absorber effect,” in *American Society of Mechanical Engineers, Manufacturing Engineering Division, MED*, 2004, vol. 15. doi: 10.1115/IMECE2004-60081.

[7] T. L. Schmitz and R. R. Donaldson, “Predicting high-speed machining dynamics by substructure analysis,” *CIRP Ann. - Manuf. Technol.*, vol. 49, no. 1, 2000, doi: 10.1016/S0007-8506(07)62951-5.

[8] Y. Altintas, G. Stepan, E. Budak, T. Schmitz, and Z. M. Kilic, “Chatter Stability of Machining Operations,” *J. Manuf. Sci. Eng. Trans. ASME*, vol. 142, no. 11, 2020, doi: 10.1115/1.4047391.

[9] Y. Altintas, *Manufacturing Automation: Metal Cutting Mechanics, Machine Tool Vibrations, and CNC Design*. Cambridge, UK: Cambridge Universtiy Press, 2000.

[10] R. E. D. Bishop and D. C. Johnson, *The Mechanics of Vibration*. 1960.

[11] T. Schmitz, E. Betters, E. Budak, E. Yüksel, S. Park, and Y. Altintas, “Review and status of tool tip frequency response function prediction using receptance coupling,” *Precis. Eng.*, vol. 79, pp. 60–77, 2023, doi: 10.1016/j.precisioneng.2022.09.008.

[12] T. L. Schmitz and K. S. Smith, *Mechanical Vibrations: Modeling and Measurement*, 2nd ed. New York: Springer, 2012. doi: 10.1007/978-1-4614-0460-6_9.

[13] W. Weaver Jr, S. P. Timoshenko, and D. H. Young, *Vibration Problems in Engineering*, 5th ed. New York: John Wiley and Sons, 1990.

[14] T. Schmitz, M. Davies, and M. Kennedy, “High-speed machining frequency response prediction for process optimization,” in *2nd International Seminar on Improving Machine Tool Performance*, 2000, pp. 3–5.

[15] T. L. Schmitz and G. S. Duncan, “Three-component receptance coupling substructure analysis for tool point dynamics prediction,” *J. Manuf. Sci. Eng. Trans. ASME*, vol. 127, no. 4, 2005, doi: 10.1115/1.2039102.

[16] S. S. Sattinger, “Method for experimentally determining rotational mobilities of structures,” *Shock Vib. Bull.;(United States)*, vol. 50, 1980.
[17] D. J. Ewins, *Modal testing: theory, practice and application*. John Wiley \& Sons, 2009.
[18] T. L. Schmitz, M. A. Davies, K. Medicus, and J. Snyder, “Improving High-Speed Machining Material Removal Rates by Rapid Dynamic Analysis,” *CIRP Ann.*, vol. 50, no. 1, pp. 263–268, Jan. 2001, doi: 10.1016/S0007-8506(07)62119-2.
[19] T. L. Schmitz, M. A. Davies, and M. D. Kennedy, “Tool point frequency response prediction for high-speed machining by rcsa,” *J. Manuf. Sci. Eng. Trans. ASME*, vol. 123, no. 4, 2001, doi: 10.1115/1.1392994.
[20] J. Zhu, J. Wang, T. Zhang, and X. Li, “An Improved Tool Point Frequency Response Function Prediction Method Based on RCSA,” *China Mech. Eng.*, vol. 26, no. 3, p. 285, 2015.
[21] B. Qi, Y. Sun, and Z. Li, “Tool point frequency response function prediction using RCSA based on Timoshenko beam model,” *Int. J. Adv. Manuf. Technol.*, vol. 92, no. 5–8, pp. 2787–2799, Sep. 2017, doi: 10.1007/s00170-017-0236-y.
[22] S. Filiz, C. H. Cheng, K. B. Powell, T. L. Schmitz, and O. B. Ozdoganlar, “An improved tool-holder model for RCSA tool-point frequency response prediction,” *Precis. Eng.*, vol. 33, no. 1, 2009, doi: 10.1016/j.precisioneng.2008.03.003.
[23] J. Zhang, T. Schmitz, W. Zhao, and B. Lu, “Receptance coupling for tool point dynamics prediction on machine tools,” *Chinese J. Mech. Eng. (English Ed.*, vol. 24, no. 3, pp. 340–345, May 2011, doi: 10.3901/CJME.2011.03.340.
[24] M. Namazi, “MECHANICS AND DYNAMICS OF THE TOOL HOLDER-SPINDLE INTERFACE,” The University of British Columbia, Vancouver, 2006.
[25] M. Namazi, Y. Altintas, T. Abe, and N. Rajapakse, “Modeling and identification of tool holder-spindle interface dynamics,” *Int. J. Mach. Tools Manuf.*, vol. 47, no. 9, pp. 1333–1341, Jul. 2007, doi: 10.1016/j.ijmachtools.2006.08.003.
[26] I. Mancisidor, M. Zatarain, J. Munoa, and Z. Dombovari, “Receptance Coupling for Tool Point Dynamics Prediction,” 2011. [Online]. Available: https://hal.archives-ouvertes.fr/hal-01352695
[27] I. Mancisidor, M. Zatarain, J. Munoa, and Z. Dombovari, “Fixed boundaries receptance coupling substructure analysis for tool point dynamics prediction,” in *Advanced Materials Research*, 2011, vol. 223, pp. 622–631. doi: 10.4028/www.scientific.net/AMR.223.622.
[28] I. Mancisidor, A. Urkiola, R. Barcena, J. Munoa, Z. Dombovari, and M. Zatarain, “Receptance coupling for tool point dynamic prediction by fixed boundaries approach,” *Int. J. Mach. Tools Manuf.*, vol. 78, pp. 18–29, Mar. 2014, doi: 10.1016/J.IJMACHTOOLS.2013.12.002.
[29] E. Budak, A. Ertürk, and H. N. Özgüven, “A modeling approach for analysis and improvement of spindle-holder-tool assembly dynamics,” *CIRP Ann. - Manuf. Technol.*, vol. 55, no. 1, 2006, doi: 10.1016/S0007-8506(07)60437-5.

[30] C.-H. Cheng, T. L. Schmitz, N. Arakere, and G. S. Duncan, “An Approach for Micro End Mill Frequency Response Predictions,” in *Manufacturing Engineering and Materials Handling, Parts A and B*, Feb. 2005, pp. 1139–1145. doi: 10.1115/IMECE2005-81215.
[31] A. Ertürk, E. Budak, and H. N. Özgüven, “Selection of design and operational parameters in spindle-holder-tool assemblies for maximum chatter stability by using a new analytical model,” *Int. J. Mach. Tools Manuf.*, vol. 47, no. 9, pp. 1401–1409, Jul. 2007, doi: 10.1016/j.ijmachtools.2006.08.016.
[32] O. Özşahin, H. N. Özgüven, and E. Budak, “Analytical modeling of asymmetric multi-segment rotor – bearing systems with Timoshenko beam model including gyroscopic moments,” *Comput. Struct.*, vol. 144, pp. 119–126, Nov. 2014, doi: 10.1016/J.COMPSTRUC.2014.08.001.
[33] J. Zhang, J. Li, Z. Xie, C. Du, L. Gui, and W. Zhao, “Rapid dynamics prediction of tool point for bi-rotary head five-axis machine tool,” *Precis. Eng.*, vol. 48, pp. 203–215, Apr. 2017, doi: 10.1016/J.PRECISIONENG.2016.12.003.
[34] A. Honeycutt and T. Schmitz, “Receptance coupling model for variable dynamics in fixed-free thin rib machining,” 2018, vol. 26, pp. 173–180. doi: 10.1016/j.promfg.2018.07.024.
[35] R. Yan, X. Tang, F. Peng, Y. Li, and H. Li, “RCSA-based method for tool frequency response function identification under operational conditions without using noncontact sensor,” *J. Manuf. Sci. Eng. Trans. ASME*, vol. 139, no. 6, Jun. 2017, doi: 10.1115/1.4035418.
[36] L. Xiaohong, J. Zhenyuan, Z. Haixing, L. Shengqian, F. Yixuan, and S. Y. Liang, “Tool Point Frequency Response Prediction for Micromilling by Receptance Coupling Substructure Analysis,” *J. Manuf. Sci. Eng. Trans. ASME*, vol. 139, no. 7, Jul. 2017, doi: 10.1115/1.4035491.
[37] G. S. Duncan and T. L. Schmitz, “An improved RCSA model for tool point frequency response prediction,” *Proc. 23rd Int. Modal Anal. Conf.*, vol. 30, 2005.
[38] G. S. Duncan, “MILLING DYNAMICS PREDICTION AND UNCERTAINTY ANALYSIS USING RECEPTANCE COUPLING SUBSTRUCTURE ANALYSIS,” University of Florida, Gainesville, 2006.
[39] T. L. Schmitz and G. S. Duncan, “Receptance coupling for dynamics prediction of assemblies with coincident neutral axes,” *J. Sound Vib.*, vol. 289, no. 4–5, pp. 1045–1065, Feb. 2006, doi: 10.1016/J.JSV.2005.03.006.
[40] T. Schmitz and B. Dutterer, “MACHINE TOOL GENOME PROJECT CASE STUDY,” in *ASPE*, 2012.
[41] T. L. Schmitz, “Machine Tool Genome Project: Tool point dynamics prediction for improved milling productivity.”
[42] K. L. Wen and H. J. Qi, “Predicting Tool Point FRF by RCSA in High Speed Milling,” *Adv. Mater. Res.*, vol. 1006–1007, pp. 398–402, Aug. 2014, doi: 10.4028/www.scientific.net/AMR.1006-1007.398.

[43] Y. Yang, M. Wan, Y. C. Ma, and W. H. Zhang, "An improved method for tool point dynamics analysis using a bi-distributed joint interface model," *Int. J. Mech. Sci.*, vol. 105, pp. 239–252, Jan. 2016, doi: 10.1016/j.ijmecsci.2015.11.014.
[44] S. S. Park, Y. Altintas, and M. Movahhedy, "Receptance coupling for end mills," *Int. J. Mach. Tools Manuf.*, vol. 43, no. 9, 2003, doi: 10.1016/S0890-6955(03)00088-9.
[45] T. J. Burns and T. L. Schmitz, "A study of linear joint and tool models in spindle-holder-tool receptance coupling," in *Proceedings of the ASME International Design Engineering Technical Conferences and Computers and Information in Engineering Conference - DETC2005*, 2005, vol. 6 B. doi: 10.1115/detc2005-85275.
[46] U. V. Kumar and T. L. Schmitz, "Spindle dynamics identification for Receptance Coupling Substructure Analysis," *Precis. Eng.*, vol. 36, no. 3, 2012, doi: 10.1016/j.precisioneng.2012.01.007.
[47] B. Uttara Vijay Kumar, "IMPROVED SPINDLE DYNAMICS IDENTIFICATION TECHNIQUE FOR RECEPTANCE COUPLING SUBSTRUCTURE ANALYSIS," University of Florida, Gainesville, 2012.
[48] P. Albertelli, M. Goletti, and M. Monno, "A new receptance coupling substructure analysis methodology to improve chatter free cutting conditions prediction," *Int. J. Mach. Tools Manuf.*, vol. 72, pp. 16–24, Sep. 2013, doi: 10.1016/J.IJMACHTOOLS.2013.05.003.
[49] P. Albertelli, M. Goletti, and M. Monno, "An Improved Receptance Coupling Substructure Analysis to Predict Chatter Free High Speed Cutting Conditions," *Procedia CIRP*, vol. 12, pp. 19–24, Jan. 2013, doi: 10.1016/J.PROCIR.2013.09.005.
[50] W. D'Ambrogio and A. Fregolent, "Substructure decoupling without using rotational DoFs: Fact or fiction?," *Mech. Syst. Signal Process.*, vol. 72–73, pp. 499–512, May 2016, doi: 10.1016/j.ymssp.2015.11.029.
[51] F. Montevecchi, N. Grossi, A. Scippa, and G. Campatelli, "Two-points-based receptance coupling method for tool-tip dynamics prediction," *Mach. Sci. Technol.*, vol. 21, no. 1, pp. 136–156, Jan. 2017, doi: 10.1080/10910344.2016.1260435.
[52] J. Liao, D. Yu, J. Zhang, P. Feng, and Z. Wu, "An efficient experimental approach to identify tool point FRF by improved receptance coupling technique," *Int. J. Adv. Manuf. Technol.*, vol. 94, no. 1–4, pp. 1451–1460, Jan. 2018, doi: 10.1007/s00170-017-0957-y.
[53] T. J. Gibbons, E. Öztürk, and N. D. Sims, "Rotational degree-of-freedom synthesis: An optimised finite difference method for non-exact data," *J. Sound Vib.*, vol. 412, pp. 207–221, Jan. 2018, doi: 10.1016/J.JSV.2017.09.031.
[54] X.-J. Xuan, Z.-H. Haung, K.-D. Wu, and J.-P. Hung, "Prediction of the Frequency Response Function of a Tool Holder-Tool Assembly Based on …," 2018. [Online]. Available: www.etasr.com
[55] Y. Ji, Q. Bi, S. Zhang, and Y. Wang, "A new receptance coupling substructure analysis methodology to predict tool tip dynamics," *Int. J. Mach. Tools Manuf.*, vol.

126, pp. 18–26, Mar. 2018, doi: 10.1016/J.IJMACHTOOLS.2017.12.002.
[56] M. Mehrpouya, M. Sanati, and S. S. Park, "Identification of joint dynamics in 3D structures through the inverse receptance coupling method," *Int. J. Mech. Sci.*, vol. 105, pp. 135–145, Jan. 2016, doi: 10.1016/J.IJMECSCI.2015.11.007.
[57] C. Brecher, P. Chavan, M. Fey, and M. Daniels, "A modal parameter approach for receptance coupling of tools," *MM Sci. J.*, vol. 2016, no. OCTOBER, pp. 1032–1034, Oct. 2016, doi: 10.17973/MMSJ.2016_10_201616.
[58] F. Montevecchi, N. Grossi, A. Scippa, and G. Campatelli, "Improved RCSA technique for efficient tool-tip dynamics prediction," *Precis. Eng.*, vol. 44, pp. 152–162, Apr. 2016, doi: 10.1016/J.PRECISIONENG.2015.11.004.
[59] E. B. Kivanc and E. Budak, "Modeling Statics and Dynamics of Milling System Components," in *Proceedings of the 36th CIRP International Seminar on Manufacturing Systems*, 2003, pp. 433–440.
[60] E. B. Kivanc and E. Budak, "Structural modeling of end mills for form error and stability analysis," *Int. J. Mach. Tools Manuf.*, vol. 44, no. 11, pp. 1151–1161, Sep. 2004, doi: 10.1016/J.IJMACHTOOLS.2004.04.002.
[61] L. Zhongqun, L. Shuo, and C. Yizhuang, "Receptance Coupling for End Mill Using 2-Section Step Beam Vibration Model," in *2009 Second International Conference on Intelligent Computation Technology and Automation*, 2009, pp. 160–163. doi: 10.1109/ICICTA.2009.276.
[62] B. Uttara Vijay Kumar, "COMPARISON OF EQUIVALENT DIAMETER END MILL MODELS FOR DYNAMICS PREDICTION BY RECEPTANCE COUPLING SUBSTRUCTURE ANALYSIS," University of Florida, Gainesville, 2009.
[63] M. A. Koplow, A. Bhattacharyya, and B. P. Mann, "Closed form solutions for the dynamic response of Euler-Bernoulli beams with step changes in cross section," *J. Sound Vib.*, vol. 295, no. 1–2, pp. 214–225, Aug. 2006, doi: 10.1016/j.jsv.2006.01.008.
[64] L. T. Tunc, "Prediction of tool tip dynamics for generalized milling cutters using the 3D model of the tool body," *Int. J. Adv. Manuf. Technol.*, vol. 95, no. 5–8, 2018, doi: 10.1007/s00170-017-1286-x.
[65] O. Özşahin and Y. Altintas, "Prediction of frequency response function (FRF) of asymmetric tools from the analytical coupling of spindle and beam models of holder and tool," *Int. J. Mach. Tools Manuf.*, vol. 92, pp. 31–40, May 2015, doi: 10.1016/J.IJMACHTOOLS.2015.03.001.
[66] B. Bediz, U. Kumar, T. L. Schmitz, and O. Burak Ozdoganlar, "Modeling and experimentation for three-dimensional dynamics of endmills," *Int. J. Mach. Tools Manuf.*, vol. 53, no. 1, pp. 39–50, Feb. 2012, doi: 10.1016/j.ijmachtools.2011.09.005.
[67] E. B. Kivanc and E. Budak, "DEVELOPMENT OF ANALYTICAL ENDMILL DEFLECTION AND DYNAMIC MODELS," *ASME Int. Mech. Eng. Congr. Expo.*,

vol. 37203, pp. 85–94, 2003.

[68] A. Ertürk, H. N. Özgüven, and E. Budak, “Effect analysis of bearing and interface dynamics on tool point FRF for chatter stability in machine tools by using a new analytical model for spindle-tool assemblies,” *Int. J. Mach. Tools Manuf.*, vol. 47, no. 1, 2007, doi: 10.1016/j.ijmachtools.2006.03.001.

[69] M. M. Rezaei, M. R. Movahhedy, M. T. Ahmadian, and H. Moradi, “Development of Inverse Receptance Coupling Method for Prediction of Milling Dynamics,” 2010. [Online]. Available: http://asmedigitalcollection.asme.org/ESDA/proceedings-pdf/ESDA2010/49194/339/2719491/339_1.pdf

[70] M. M. Rezaei, M. R. Movahhedy, H. Moradi, and M. T. Ahmadian, “Extending the inverse receptance coupling method for prediction of tool-holder joint dynamics in milling,” *J. Manuf. Process.*, vol. 14, no. 3, pp. 199–207, Aug. 2012, doi: 10.1016/J.JMAPRO.2011.11.003.

[71] M. Faraji Ghanati and R. Madoliat, “New continuous dynamic coupling for three component modeling of tool-holder-spindle structure of machine tools with modified effected tool damping,” *J. Manuf. Sci. Eng. Trans. ASME*, vol. 134, no. 2, 2012, doi: 10.1115/1.4006094.

[72] N. Grossi, F. Montevecchi, A. Scippa, and G. Campatelli, “3D Finite Element Modeling of Holder-Tool Assembly for Stability Prediction in Milling,” *Procedia CIRP*, vol. 31, pp. 527–532, Jan. 2015, doi: 10.1016/J.PROCIR.2015.03.031.

[73] J. Zhu, D. He, F. Tian, and Q. Zhao, “A New Prediction Method of Tool Point Frequency Response Function for Milling Cutters,” *China Mech. Eng.*, vol. 27, no. 20, p. 2765, 2016.

[74] W. Matthias, O. Özşahin, Y. Altintas, and B. Denkena, “Receptance coupling based algorithm for the identification of contact parameters at holder–tool interface,” *CIRP J. Manuf. Sci. Technol.*, vol. 13, pp. 37–45, May 2016, doi: 10.1016/J.CIRPJ.2016.02.005.

[75] S. S. Park and J. Chae, “Joint identification of modular tools using a novel receptance coupling method,” *Int. J. Adv. Manuf. Technol.*, vol. 35, no. 11–12, pp. 1251–1262, Feb. 2008, doi: 10.1007/s00170-006-0826-6.

[76] H. Ahmadian and M. Nourmohammadi, “Tool point dynamics prediction by a three-component model utilizing distributed joint interfaces,” *Int. J. Mach. Tools Manuf.*, vol. 50, no. 11, pp. 998–1005, Nov. 2010, doi: 10.1016/j.ijmachtools.2010.07.003.

[77] T. Schmitz, A. Honeycutt, M. Gomez, M. Stokes, and E. Betters, “Multi-point coupling for tool point receptance prediction,” *J. Manuf. Process.*, vol. 43, 2019, doi: 10.1016/j.jmapro.2019.03.043.

[78] C. H. Cheng, T. L. Schmitz, and G. S. Duncan, “Rotating tool point frequency response prediction using RCSA,” *Mach. Sci. Technol.*, vol. 11, no. 3, pp. 433–446, Jul. 2007, doi: 10.1080/10910340701539866.

[79] N. Grossi, L. Sallese, F. Montevecchi, A. Scippa, and G. Campatelli, “Speed-varying Machine Tool Dynamics Identification Through Chatter Detection and

Receptance Coupling," in *Procedia CIRP*, 2016, vol. 55, pp. 77–82. doi: 10.1016/j.procir.2016.08.022.

[80] J. S. Agapiou, "A methodology to measure joint stiffness parameters for toolholder-spindle interfaces," *J. Manuf. Syst.*, vol. 24, no. 1, pp. 13–20, Jan. 2005, doi: 10.1016/S0278-6125(05)80003-2.

[81] O. Özşahin, A. Ertürk, H. N. Özgüven, and E. Budak, "A closed-form approach for identification of dynamical contact parameters in spindle–holder–tool assemblies," *Int. J. Mach. Tools Manuf.*, vol. 49, no. 1, pp. 25–35, Jan. 2009, doi: 10.1016/J.IJMACHTOOLS.2008.08.007.

[82] L. J. Zhai, X. L. Song, and L. G. Cai, "Identification of toolholder-spindle joint based on receptance coupling substructure analysis," in *Applied Mechanics and Materials*, 2013, vol. 345, pp. 539–542. doi: 10.4028/www.scientific.net/AMM.345.539.

[83] S. Wan, J. Hong, F. Du, B. Fang, and X. Li, "Modelling and characteristic investigation of spindle-holder assembly under clamping and centrifugal forces," *J. Mech. Sci. Technol.*, vol. 33, no. 5, pp. 2397–2405, May 2019, doi: 10.1007/s12206-019-0438-3.

[84] O. Özşahin, E. Budak, and H. N. Özgüven, "Identification of bearing dynamics under operational conditions for chatter stability prediction in high speed machining operations," *Precis. Eng.*, vol. 42, pp. 53–65, Oct. 2015, doi: 10.1016/J.PRECISIONENG.2015.03.010.

[85] D. C. Cong, J. Hwang, J. Shim, S. K. Ro, and T. Schmitz, "Effects of a drawbar design and force on multipurpose aerostatic spindle dynamics," *Int. J. Mach. Tools Manuf.*, vol. 144, p. 103424, Sep. 2019, doi: 10.1016/J.IJMACHTOOLS.2019.103424.

[86] T. L. Schmitz and T. J. Burns, "Receptance Coupling for High-Speed Machining Dynamics Prediction," in *Proceedings of IMAC-XXI: A Conference and Exposition on Structural Dynamics*, 2003.

[87] E. Budak, "Analytical models for high performance milling. Part II: Process dynamics and stability," *Int. J. Mach. Tools Manuf.*, vol. 46, no. 12–13, pp. 1489–1499, Oct. 2006, doi: 10.1016/j.ijmachtools.2005.09.010.

[88] B. A. Mascardelli, S. S. Park, and T. Freiheit, "Substructure coupling of microend mills to aid in the suppression of chatter," *J. Manuf. Sci. Eng. Trans. ASME*, vol. 130, no. 1, pp. 0110101–01101012, Feb. 2008, doi: 10.1115/1.2816104.

[89] V. Ostad Ali Akbari, M. Postel, M. Kuffa, and K. Wegener, "Improving stability predictions in milling by incorporation of toolholder sound emissions," *CIRP J. Manuf. Sci. Technol.*, vol. 37, pp. 359–369, May 2022, doi: 10.1016/J.CIRPJ.2022.02.012.

[90] M. Mehrpouya, E. Graham, and S. S. Park, "FRF based joint dynamics modeling and identification," *Mech. Syst. Signal Process.*, vol. 39, no. 1–2, pp. 265–279, Aug. 2013, doi: 10.1016/j.ymssp.2013.03.022.

[91] M. Mehrpouya, E. Graham, and S. S. Park, "Identification of multiple joint dynamics using the inverse receptance coupling method," *JVC/Journal Vib. Control*, vol. 21, no. 16, pp. 3431–3449, Dec. 2015, doi: 10.1177/1077546314523306.

[92] Z. Li, Z. Wang, X. Shi, and W. Li, "RCSA-based prediction of chatter stability for milling process with large axial depth of cut," *Int. J. Adv. Manuf. Technol.*, vol. 96, no. 1–4, pp. 833–843, Apr. 2018, doi: 10.1007/s00170-018-1615-8.

[93] A. Ertürk, H. N. Özgüven, and E. Budak, "Analytical modeling of spindle–tool dynamics on machine tools using Timoshenko beam model and receptance coupling for the prediction of tool point FRF," *Int. J. Mach. Tools Manuf.*, vol. 46, no. 15, pp. 1901–1912, Dec. 2006, doi: 10.1016/J.IJMACHTOOLS.2006.01.032.

[94] T. L. Schmitz, K. Powell, D. Won, G. Scott Duncan, W. Gregory Sawyer, and J. C. Ziegert, "Shrink fit tool holder connection stiffness/damping modeling for frequency response prediction in milling," *Int. J. Mach. Tools Manuf.*, vol. 47, no. 9, 2007, doi: 10.1016/j.ijmachtools.2006.08.009.

[95] W. Xiao, K. Mao, M. Zhu, B. Li, S. Lei, and X. Pan, "Modelling the spindle-holder taper joint in machine tools: A tapered zero-thickness finite element method," *J. Sound Vib.*, vol. 333, no. 22, pp. 5836–5850, Oct. 2014, doi: 10.1016/j.jsv.2014.06.023.

[96] J.-P. Hung, W.-Z. Lin, K.-D. Wu, and W.-C. Shih, "Analyzing the Dynamic Characteristics of Milling Tool Using Finite Element Method and Receptance Coupling Method," 2019. [Online]. Available: www.etasr.com

[97] C. Brecher, P. Chavan, and M. Fey, "Efficient joint identification and fluted segment modelling of shrink-fit tool assemblies by updating extended tool models," *Prod. Eng.*, vol. 15, no. 1, pp. 21–33, Feb. 2021, doi: 10.1007/s11740-020-00999-0.

[98] K. Ahmadi and H. Ahmadian, "Modelling machine tool dynamics using a distributed parameter tool-holder joint interface," *Int. J. Mach. Tools Manuf.*, vol. 47, no. 12–13, 2007, doi: 10.1016/j.ijmachtools.2007.03.004.

[99] Y. Yang, M. Wan, Y. C. Ma, and W. H. Zhang, "A new method using double distributed joint interface model for three-dimensional dynamics prediction of spindle-holder-tool system," *Int. J. Adv. Manuf. Technol.*, vol. 95, no. 5–8, pp. 2729–2745, Mar. 2018, doi: 10.1007/s00170-017-1394-7.

[100] O. Özşahin, M. Ritou, E. Budak, C. Rabréau, and S. Le Loch, "Identification of spindle dynamics by receptance coupling for non-contact excitation system," *Procedia CIRP*, vol. 82, pp. 273–278, Jan. 2019, doi: 10.1016/J.PROCIR.2019.04.038.

[101] M. R. Movahhedy and J. M. Gerami, "Prediction of spindle dynamics in milling by sub-structure coupling," *Int. J. Mach. Tools Manuf.*, vol. 46, no. 3–4, pp. 243–251, Mar. 2006, doi: 10.1016/j.ijmachtools.2005.05.026.

[102] D.-H. Lee and W.-S. Hwang, "An identification method for joint structural parameters using an FRF-based substructuring method and an optimization

technique," 2007.
[103] O. Ozsahin, H. N. Özgüven, E. Budak, O. Özşahin, H. N. Özgüven, and E. Budak, "Estimation of Dynamic Contact Parameters for Machine Tool Spindle-Holder-Tool Assemblies Using Artificial Neural Networks," *Proc. 3rd Int. Conf. Manuf. Eng.*, pp. 131–144, 2008, [Online]. Available: https://www.researchgate.net/publication/233859351
[104] E. Wang, B. Wu, Y. Hu, S. Yang, and Y. Cheng, "Dynamic parameter identification of tool-spindle interface based on RCSA and particle swarm optimization," *Shock Vib.*, vol. 20, no. 1, pp. 69–78, 2013, doi: 10.3233/SAV-2012-0728.
[105] M. Pour and H. Ghorbani, "Improving FEM model of low immersion milling process using multi-objective optimization of tool elastic support dynamic properties," *Int. J. Adv. Manuf. Technol.*, vol. 92, no. 5–8, pp. 2279–2297, Sep. 2017, doi: 10.1007/s00170-017-0261-x.
[106] Đ. Čiča, M. Zeljković, and S. Tešić, "Dynamical contact parameter identification of spindle-holder-tool assemblies using soft computing techniques," *Facta Univ. Ser. Mech. Eng.*, vol. 18, no. 4, pp. 565–577, 2020, doi: 10.22190/FUME191014012C.
[107] V. Ganguly and T. L. Schmitz, "Spindle dynamics identification using particle swarm optimization," *J. Manuf. Process.*, vol. 15, no. 4, pp. 444–451, Oct. 2013, doi: 10.1016/j.jmapro.2013.05.008.
[108] G. S. Duncan, M. F. Tummond, and T. L. Schmitz, "An investigation of the dynamic absorber effect in high-speed machining," *Int. J. Mach. Tools Manuf.*, vol. 45, no. 4–5, pp. 497–507, Apr. 2005, doi: 10.1016/J.IJMACHTOOLS.2004.09.005.
[109] H. Ding, Y. Ding, and L. M. Zhu, "On time-domain methods for milling stability analysis," *Chinese Science Bulletin*, vol. 57, no. 33. Science in China Press, pp. 4336–4345, Nov. 01, 2012. doi: 10.1007/s11434-012-5499-y.
[110] J. Munoa *et al.*, "Chatter suppression techniques in metal cutting," *CIRP Ann. - Manuf. Technol.*, vol. 65, no. 2, pp. 785–808, 2016, doi: 10.1016/j.cirp.2016.06.004.
[111] R. E. Vasquez, "On the use of structural dynamics in virtual manufacturing," *Int. J. Interact. Des. Manuf.*, vol. 11, no. 1, pp. 103–114, Feb. 2017, doi: 10.1007/s12008-014-0240-5.
[112] M. Postel, O. Özsahin, and Y. Altintas, "High speed tooltip FRF predictions of arbitrary tool-holder combinations based on operational spindle identification," *Int. J. Mach. Tools Manuf.*, vol. 129, 2018, doi: 10.1016/j.ijmachtools.2018.03.004.
[113] G. Yu, L. Wang, J. Wu, and Y. Gao, "Milling stability prediction of a hybrid machine tool considering low-frequency dynamic characteristics," *Mech. Syst. Signal Process.*, vol. 135, p. 106364, Jan. 2020, doi: 10.1016/J.YMSSP.2019.106364.
[114] M. Postel, B. Bugdayci, and K. Wegener, "Ensemble transfer learning for refining stability predictions in milling using experimental stability states," *Int. J. Adv. Manuf. Technol.*, vol. 107, no. 9–10, pp. 4123–4139, Apr. 2020, doi: 10.1007/s00170-020-05322-w.

[115] T. Schmitz, "Modal interactions for spindle, holders, and tools," *Procedia Manuf.*, vol. 48, pp. 457–465, Jan. 2020, doi: 10.1016/J.PROMFG.2020.05.069.
[116] N. Greis, M. Nogueira, S. Bhattacharya, and T. Schmitz, "Physics-Guided Machine Learning for Self-Aware Machining."
[117] E. Ozturk, U. Kumar, S. Turner, and T. Schmitz, "Investigation of spindle bearing preload on dynamics and stability limit in milling," *CIRP Ann.*, vol. 61, no. 1, pp. 343–346, Jan. 2012, doi: 10.1016/J.CIRP.2012.03.134.
[118] Y. Ji, Q. Bi, L. Yu, F. Ren, and Y. Wang, "A Robust RCSA-Based Method for the In Situ Measurement of Rotating Tool-Tip Frequency Response Functions," *J. Manuf. Sci. Eng.*, vol. 142, no. 8, Aug. 2020, doi: 10.1115/1.4046989.
[119] T. L. Schmitz, M. Tummond, G. S. Duncan, C. Zahner, and J. P. Snyder, "DEVELOPMENT OF AN INTERNET-BASED PLATFORM FOR HIGH-SPEED MILLING PROCESS PARAMETER SELECTION."
[120] A. Banerjee, E. V. Bordatchev, and H. Y. Feng, "Determination of minimum limiting axial depth of cut for 2d pocket machining based on receptance coupling," *Mach. Sci. Technol.*, vol. 13, no. 2, pp. 177–195, Apr. 2009, doi: 10.1080/10910340902979762.
[121] D. Xu, R. Kang, and Q. Liu, "Research on NC machine tool dynamic characteristic considering processing dynamics," in *Proceedings - 2010 International Conference on Intelligent System Design and Engineering Application, ISDEA 2010*, 2010, vol. 2, pp. 227–231. doi: 10.1109/ISDEA.2010.176.
[122] M. Law, Y. Altintas, and A. Srikantha Phani, "Rapid evaluation and optimization of machine tools with position-dependent stability," *Int. J. Mach. Tools Manuf.*, vol. 68, pp. 81–90, 2013, doi: 10.1016/j.ijmachtools.2013.02.003.
[123] M. Law, H. Rentzsch, and S. Ihlenfeldt, "Evaluating Mobile Machine Tool Dynamics by Substructure Synthesis," *Adv. Mater. Res.*, vol. 1018, pp. 373–380, Sep. 2014, doi: 10.4028/www.scientific.net/AMR.1018.373.
[124] D. Wang *et al.*, "Surface location error prediction and stability analysis of micro-milling with variation of tool overhang length," *Int. J. Adv. Manuf. Technol.*, vol. 99, no. 1–4, pp. 919–936, Oct. 2018, doi: 10.1007/s00170-018-2446-3.
[125] M. Law, H. Rentzsch, and S. Ihlenfeldt, "Development of a Dynamic Substructuring Framework to Facilitate in Situ Machining Solutions Using Mobile Machine Tools," *Procedia Manuf.*, vol. 1, pp. 756–767, Jan. 2015, doi: 10.1016/J.PROMFG.2015.09.054.
[126] Y. Yang, W. H. Zhang, Y. C. Ma, and M. Wan, "Generalized method for the analysis of bending, torsional and axial receptances of tool-holder-spindle assembly," *Int. J. Mach. Tools Manuf.*, vol. 99, 2015, doi: 10.1016/j.ijmachtools.2015.08.004.
[127] M. Law, H. Rentzsch, S. Ihlenfeldt, and M. Putz, "Application of Substructure Decoupling Techniques to Predict Mobile Machine Tool Dynamics: Numerical Investigations," *Procedia CIRP*, vol. 46, pp. 537–540, Jan. 2016, doi: 10.1016/J.PROCIR.2016.04.126.

[128] M. Law, H. Rentzsch, and S. Ihlenfeldt, “Predicting mobile machine tool dynamics by experimental dynamic substructuring,” *Int. J. Mach. Tools Manuf.*, vol. 108, pp. 127–134, Sep. 2016, doi: 10.1016/J.IJMACHTOOLS.2016.06.006.
[129] J. S. Dhupia, B. Powalka, A. Galip Ulsoy, and R. Katz, “Effect of a nonlinear joint on the dynamic performance of a machine tool,” *J. Manuf. Sci. Eng. Trans. ASME*, vol. 129, no. 5, pp. 943–950, Oct. 2007, doi: 10.1115/1.2752830.
[130] M. Law and S. Ihlenfeldt, “A frequency-based substructuring approach to efficiently model position-dependent dynamics in machine tools,” *Proc. Inst. Mech. Eng. Part K J. Multi-body Dyn.*, vol. 229, no. 3, pp. 304–317, Sep. 2015, doi: 10.1177/1464419314562264.
[131] S. Nagesh and M. Law, “Machine tool design with preferentially asymmetrical structures to improve dynamics and productivity,” in *Procedia CIRP*, 2019, vol. 79, pp. 592–595. doi: 10.1016/j.procir.2019.02.086.
[132] C. Chen, F. Peng, R. Yan, X. Tang, Y. Li, and Z. Fan, “Rapid prediction of posture-dependent FRF of the tool tip in robotic milling,” *Robot. Comput. Integr. Manuf.*, vol. 64, p. 101906, Aug. 2020, doi: 10.1016/J.RCIM.2019.101906.
[133] D. Bilgili, E. Budak, and Y. Altintas, “Multibody dynamic modeling of five-axis machine tools with improved efficiency,” *Mech. Syst. Signal Process.*, vol. 171, p. 108945, May 2022, doi: 10.1016/J.YMSSP.2022.108945.
[134] M. Kato, D. Kono, and Y. Kakinuma, “Dynamical characteristic validation of motorized CFRP spindle unit based on receptance coupling,” *Mech. Syst. Signal Process.*, vol. 173, p. 109028, Jul. 2022, doi: 10.1016/J.YMSSP.2022.109028.
[135] L. Wu, G. Wang, H. Liu, and T. Huang, “An improved algorithm to predict the pose-dependent cutting stability in robot milling,” *Int. J. Adv. Manuf. Technol.*, Feb. 2022, doi: 10.1007/s00170-022-08924-8.
[136] T. L. Schmitz, “Investigation of Retention Knob Geometry on Machining Dynamics,” *Procedia Manuf.*, vol. 1, pp. 578–583, Jan. 2015, doi: 10.1016/J.PROMFG.2015.09.034.
[137] A. Bansal and M. Law, “A receptance coupling approach to optimally tune and place absorbers on boring bars for chatter suppression,” in *Procedia CIRP*, 2018, vol. 77, pp. 167–170. doi: 10.1016/j.procir.2018.08.267.
[138] A. Yadav, D. Talaviya, A. Bansal, and M. Law, “Design of chatter-resistant damped boring bars using a receptance coupling approach,” *J. Manuf. Mater. Process.*, vol. 4, no. 2, Jun. 2020, doi: 10.3390/jmmp4020053.
[139] T. J. Gibbons, E. Ozturk, L. Xu, and N. D. Sims, “Chatter avoidance via structural modification of tool-holder geometry,” *Int. J. Mach. Tools Manuf.*, vol. 150, p. 103514, Mar. 2020, doi: 10.1016/J.IJMACHTOOLS.2019.103514.
[140] G. Karataş, O. Özşahin, H. N. Özgüven, and E. Budak, “Design optimization of tool holder extension for enhanced chatter stability by using component mode tuning method,” *Procedia CIRP*, vol. 101, pp. 294–297, 2021, doi: 10.1016/j.procir.2021.02.033.

[141] N. Bertelsen, R. A. Alphinas, and K. B. Ørskov, “A tool tuning approximation method: Exploration of the system dynamics and its impact on milling stability when amending tool stickout,” in *ESAFORM 2021 - 24th International Conference on Material Forming*, 2021. doi: 10.25518/esaform21.918.
[142] W. Ma, Y. Yang, and X. Jin, “Chatter suppression in micro-milling using shank-mounted Two-DOF tuned mass damper,” *Precis. Eng.*, vol. 72, pp. 144–157, Nov. 2021, doi: 10.1016/J.PRECISIONENG.2021.04.017.
[143] W. Ma, J. Yu, Y. Yang, and Y. Wang, “Optimization and tuning of passive tuned mass damper embedded in milling tool for chatter mitigation,” *J. Manuf. Mater. Process.*, vol. 5, no. 1, Mar. 2021, doi: 10.3390/jmmp5010002.
[144] L. N. Liu, Z. Y. Shi, Z. Q. Liu, and H. Song, “Modal analysis of high-speed face milling system based on composite structure system analysis method,” in *Materials Science Forum*, 2014, vol. 800, pp. 408–413.
[145] A. Astarloa, M. H. Fernandes, I. Mancisidor, J. Munoa, and Z. Dombovari, “Prediction of the dynamic stiffness of boring bars,” *IOP Conf. Ser. Mater. Sci. Eng.*, vol. 1193, no. 1, p. 012007, Oct. 2021, doi: 10.1088/1757-899X/1193/1/012007.
[146] Y. Mohammadi, M. Azvar, and E. Budak, “Suppressing vibration modes of spindle-holder-tool assembly through FRF modification for enhanced chatter stability,” *CIRP Ann.*, vol. 67, no. 1, pp. 397–400, Jan. 2018, doi: 10.1016/J.CIRP.2018.03.003.
[147] S. S. Park and Y. Altintas, “Dynamic compensation of spindle integrated force sensors with Kalman filter,” *J. Dyn. Syst. Meas. Control. Trans. ASME*, vol. 126, no. 3, pp. 443–452, Sep. 2004, doi: 10.1115/1.1789531.
[148] Y. Altintas and S. S. Park, “Dynamic Compensation of Spindle-Integrated Force Sensors,” *CIRP Ann.*, vol. 53, no. 1, pp. 305–308, 2004, [Online]. Available: http://www.mech.ubc.ca/-ma1
[149] T. L. Schmitz, “IMPROVED SENSOR DATA UTILITY THROUGH RECEPTANCE COUPLING MODELING,” *ASME Int. Mech. Eng. Congr. Expo.*, vol. 47055, pp. 411–417, 2004, [Online]. Available: https://proceedings.asmedigitalcollection.asme.org
[150] S. S. Park, “Identification of Spindle Integrated Force Sensor’s Transfer Function for Modular End Mills,” *J. Manuf. Sci. Eng.*, vol. 128, no. 1, pp. 146–153, Aug. 2006, doi: 10.1115/1.2137749.
[151] X. Wang, Y. Guo, and T. Chen, “Measurement research of motorized spindle dynamic stiffness under high speed rotating,” *Shock Vib.*, vol. 2015, 2015, doi: 10.1155/2015/284126.
[152] K. Kiran, H. Satyanarayana, and T. Schmitz, “Compensation of frequency response function measurements by inverse RCSA,” *Int. J. Mach. Tools Manuf.*, vol. 121, 2017, doi: 10.1016/j.ijmachtools.2017.04.004.
[153] H. Satyanarayana, “COMPENSATION OF FREQUENCY RESPONSE

FUNCTION MEASUREMENTS BY INVERSE RCSA," 2017.
[154] C. Wang, B. Qiao, X. Zhang, H. Cao, and X. Chen, "TPA and RCSA based frequency response function modelling for cutting forces compensation," *J. Sound Vib.*, vol. 456, pp. 272–288, Sep. 2019, doi: 10.1016/J.JSV.2019.05.043.
[155] H. Mostaghimi, C. I. Park, G. Kang, S. S. Park, and D. Y. Lee, "Reconstruction of cutting forces through fusion of accelerometer and spindle current signals," *J. Manuf. Process.*, vol. 68, pp. 990–1003, Aug. 2021, doi: 10.1016/j.jmapro.2021.06.007.
[156] Y. Ji, Y. Chen, S. Zhang, Q. Bi, and Y. Wang, "Multi-Point Substructure Coupling Method to Compensate Multi-Accelerometer Masses in Measuring Rotation-Related Frequency Response Functions," *J. Manuf. Sci. Eng.*, vol. 144, no. 1, Jan. 2022, doi: 10.1115/1.4051534.
[157] O. Özşahin, H. N. Özgüven, and E. Budak, "Analysis and compensation of mass loading effect of accelerometers on tool point FRF measurements for chatter stability predictions," *Int. J. Mach. Tools Manuf.*, vol. 50, no. 6, pp. 585–589, Jun. 2010, doi: 10.1016/J.IJMACHTOOLS.2010.02.002.
[158] M. Malekian, S. S. Park, and M. B. G. Jun, "Modeling of dynamic micro-milling cutting forces," *Int. J. Mach. Tools Manuf.*, vol. 49, no. 7–8, pp. 586–598, Jun. 2009, doi: 10.1016/j.ijmachtools.2009.02.006.
[159] X. Lu, Z. Jia, S. Liu, K. Yang, Y. Feng, and S. Y. Liang, "Chatter stability of micro-milling by considering the centrifugal force and gyroscopic effect of the spindle," *J. Manuf. Sci. Eng. Trans. ASME*, vol. 141, no. 11, Nov. 2019, doi: 10.1115/1.4044520.
[160] S. S. Park and R. Rahnama, "Robust chatter stability in micro-milling operations," *CIRP Ann. - Manuf. Technol.*, vol. 59, no. 1, pp. 391–394, 2010, doi: 10.1016/j.cirp.2010.03.023.
[161] M. Jasiewicz and B. Powałka, "Prediction of turning stability using receptance coupling," in *AIP Conference Proceedings*, Jan. 2018, vol. 1922. doi: 10.1063/1.5019090.
[162] H. Li, G. Xue, Y. Zhou, H. Li, and B. Wen, "Receptance coupling for frequency response prediction of cylindrical workpiece in CNC lathe," vol. 17, no. 4, 2015.
[163] M. Jasiewicz and B. Powalka, "Identification of a Lathe Spindle Dynamics Using Extended Inverse Receptance Coupling," *J. Dyn. Syst. Meas. Control. Trans. ASME*, vol. 140, no. 12, Dec. 2018, doi: 10.1115/1.4040968.
[164] A. Barrios, S. Mata, A. Fernandez, J. Munoa, C. Sun, and E. Ozturk, "Frequency response prediction for robot assisted machining," *MM Sci. J.*, vol. 2019, no. November, pp. 3099–3106, 2019, doi: 10.17973/MMSJ.2019_11_2019057.
[165] K. Kiran and M. C. Kayacan, "Effect of material removal on workpiece dynamics in milling: Modeling and measurement," *Precis. Eng.*, vol. 60, pp. 506–519, Nov. 2019, doi: 10.1016/j.precisioneng.2019.09.003.
[166] T. L. Schmitz and A. Honeycutt, "Analytical solutions for fixed-free beam dynamics

in thin rib machining," *J. Manuf. Process.*, vol. 30, pp. 41–50, Dec. 2017, doi: 10.1016/J.JMAPRO.2017.09.002.

[167] Y. Danylchenko *et al.*, "Dynamic characteristics of 'tool-workpiece' elastic system in the low stiffness parts milling process," in *Mechatronic Systems 2: Applications in Material Handling Processes and Robotics*, Routledge, 2021, pp. 225–236.

[168] X. Jin and N. G. Koya, "Prediction of coupled torsional–axial vibrations of drilling tool with clamping boundary conditions," *CIRP J. Manuf. Sci. Technol.*, vol. 13, pp. 24–36, May 2016, doi: 10.1016/J.CIRPJ.2016.02.001.

[169] V. Ostad Ali Akbari and K. Ahmadi, "Substructure analysis of vibration-assisted drilling systems," *Int. J. Adv. Manuf. Technol.*, vol. 113, no. 9–10, 2021, doi: 10.1007/s00170-021-06777-1.

[170] A. J. Kiefer, "INTEGRATING ELECTROMECHANICAL ACTUATOR HARDWARE," North Carolina State University, Raleigh, 2004.

[171] M. Malekian, D. Trieu, J. S. Owoc, S. S. Park, and C. J. Hunter, "Investigation of the intervertebral disc and fused joint dynamics through experimental modal analysis and the receptance coupling method," *J. Biomech. Eng.*, vol. 132, no. 4, Apr. 2010, doi: 10.1115/1.4001114.

[172] Y. Ding, L. Li, A. Krause, and O. Riemer, "Frequency response prediction of spindle-workpiece assemblies for ultra-precision diamond turning based on substructure analysis," 2012.

[173] J. Su and B. Wang, "Research Progress of Synthesis and Modification Methods Based on Dynamic Substructures," *Shock and Vibration*, vol. 2020. Hindawi Limited, 2020. doi: 10.1155/2020/6475716.

[174] X. Li, J. Zhu, F. Tian, and Z. Huang, "An improved rapid prediction method of the milling tool point frequency response function," *Int. J. Adv. Manuf. Technol.*, vol. 110, no. 3–4, pp. 841–852, Sep. 2020, doi: 10.1007/s00170-020-05929-z.

[175] J. H. SHAIK, J. S. AS, T. S. RAO, K. R. Kotaiah, and B. R. Kumar, "Identification of practical spindle-tool interface parameters using an optimization based statistical approach," *Sādhanā*, vol. 46, no. 111, 2021, doi: 10.1007/s12046-021-01635-y.

[176] L. Morelli, N. Grossi, G. Campatelli, and A. Scippa, "Surface location error prediction in 2.5-axis peripheral milling considering tool dynamic stiffness variation," *Precis. Eng.*, vol. 76, pp. 95–109, Jul. 2022, doi: 10.1016/J.PRECISIONENG.2022.03.008.

[177] T. L. Schmitz, "Torsional and axial frequency response prediction by RCSA," *Precis. Eng.*, vol. 34, no. 2, pp. 345–356, Apr. 2010, doi: 10.1016/j.precisioneng.2009.08.005.

[178] M. Mehrpouya and S. S. Park, "Prediction of atomic force microscope probe dynamics through the receptance coupling method," *Rev. Sci. Instrum.*, vol. 82, no. 12, Dec. 2011, doi: 10.1063/1.3664787.

[179] S. Ema and R. Davies, "Cutting performance of end mills with different helix angles," *Int. J. Mach. Tools Manuf.*, vol. 29, no. 2, pp. 217–227, 1989, doi:

10.1016/0890-6955(89)90033-3.
[180] M. Plodzien, J. Burek, L. Zylka, and P. Sulkowicz, “The influence of end mill helix angle on high performance milling process,” *J. Mech. Sci. Technol.*, vol. 34, no. 2, pp. 817–827, 2020, doi: 10.1007/s12206-020-0131-6.
[181] D. D. Rosard, “Natural Frequencies of Twisted Cantilever Beams,” *J. Appl. Mech.*, vol. 20, no. 2, pp. 241–244, 1953, doi: 10.1115/1.4010656.
[182] R. C. Di Prima and G. H. Handelman, “Vibrations of twisted beams,” *Q. Appl. Math.*, vol. 12, no. 3, pp. 241–259, 1954, doi: 10.1090/qam/64619.
[183] B. Dawson, N. G. Ghosh, and W. Carnegie, “Effect of Slenderness Ratio on the Natural Frequencies of Pre-Twisted Cantilever Beams of Uniform Rectangular Cross-Section,” *J. Mech. Eng. Sci.*, vol. 13, no. 1, pp. 51–59, Feb. 1971, doi: 10.1243/JMES_JOUR_1971_013_008_02.
[184] W. Carnegie and J. Thomas, “The Coupled Bending—Bending Vibration of Pre-Twisted Tapered Blading,” *J. Eng. Ind.*, vol. 94, no. 1, pp. 255–266, Feb. 1972, doi: 10.1115/1.3428120.
[185] C. K. Chen and S. H. Ho, “Transverse vibration of a rotating twisted Timoshenko beams under axial loading using differential transform,” *Int. J. Mech. Sci.*, vol. 41, no. 11, pp. 1339–1356, 1999, doi: 10.1016/S0020-7403(98)00095-2.
[186] J. R. Banerjee, “Free vibration analysis of a twisted beam using the dynamic stiffness method,” *Int. J. Solids Struct.*, vol. 38, no. 38–39, pp. 6703–6722, 2001, doi: 10.1016/S0020-7683(01)00119-6.
[187] S. K. Sinha and K. E. Turner, “Natural frequencies of a pre-twisted blade in a centrifugal force field,” *J. Sound Vib.*, vol. 330, no. 11, pp. 2655–2681, 2011, doi: 10.1016/j.jsv.2010.12.017.
[188] M. N. V. Ramesh and N. Mohan Rao, “Free vibration analysis of pre-twisted rotating FGM beams,” *Int. J. Mech. Mater. Des.*, vol. 9, no. 4, pp. 367–383, 2013, doi: 10.1007/s10999-013-9226-x.
[189] J. R. Hutchinson, “Shear coefficients for timoshenko beam theory,” *J. Appl. Mech. Trans. ASME*, vol. 68, no. 1, pp. 87–92, 2001, doi: 10.1115/1.1349417.
[190] Kennametal, “High-Performance Solid Carbide End Mills.” https://www.kennametal.com/us/en/products/metalworking-tools/milling/solid-end-milling/high-performance-solid-carbide-end-mills.html
[191] D. Systemes, “Meshing Options.” https://help.solidworks.com/2021/english/SolidWorks/cworks/c_meshing_options.htm?id=7236c6828ed74a489e328dd0244d038e#Pg0
[192] Big Daishowa- Americas, “Comparing Tool Holder Performance and Price,” 2019. https://www.bigdaishowa.com/en/blog/comparing-tool-holder-performance-and-price
[193] M. F. Gomez, “Displacement-based dynamometer for milling force measurement,” University of Tennessee Knoxville, 2021.

APPENDIX

Fitting Coefficients for Frequency and Helix Factor Curves

Table A-1. The coefficients corresponding to number of flutes and tool diameter to relate helix angle and length to diameter ratio to predicted natural frequency.

3 Flutes

Diameter	C_0	C_1	C_2	C_3	C_4	C_5
6.35	2.82E+05	-3.76E+02	-9.63E+04	-4.19E+00	8.72E+01	8.70E+03
9.53	1.88E+05	-2.51E+02	-6.43E+04	-2.79E+00	5.82E+01	5.81E+03
12.7	1.41E+05	-1.88E+02	-4.82E+04	-2.10E+00	4.37E+01	4.36E+03
15.9	1.13E+05	-1.50E+02	-3.86E+04	-1.68E+00	3.49E+01	3.49E+03
19.05	9.40E+04	-1.25E+02	-3.22E+04	-1.40E+00	2.91E+01	2.91E+03
25.4	7.05E+04	-9.40E+01	-2.41E+04	-1.05E+00	2.18E+01	2.18E+03

4 Flutes

Diameter	C_0	C_1	C_2	C_3	C_4	C_5
6.35	3.00E+05	-3.38E+02	-1.02E+05	-4.25E+00	8.16E+01	9.24E+03
9.53	2.00E+05	-2.26E+02	-6.83E+04	-2.85E+00	5.46E+01	6.17E+03
12.7	1.59E+05	-1.37E+02	-5.77E+04	-2.32E+00	3.18E+01	5.77E+03
15.9	1.20E+05	-1.36E+02	-4.10E+04	-1.71E+00	3.28E+01	3.70E+03
19.05	1.00E+05	-1.13E+02	-3.42E+04	-1.43E+00	2.74E+01	3.09E+03
25.4	7.51E+04	-8.50E+01	-2.56E+04	-1.07E+00	2.05E+01	2.31E+03

5 Flutes

Diameter	C_0	C_1	C_2	C_3	C_4	C_5
6.35	3.08E+05	-2.41E+02	-1.06E+05	-2.67E+00	5.59E+01	9.62E+03
9.53	2.05E+05	-1.61E+02	-7.06E+04	-1.79E+00	3.74E+01	6.42E+03
12.7	1.54E+05	-1.21E+02	-5.30E+04	-1.35E+00	2.81E+01	4.82E+03
15.9	1.23E+05	-9.70E+01	-4.24E+04	-1.08E+00	2.25E+01	3.85E+03
19.05	1.03E+05	-8.08E+01	-3.53E+04	-8.97E-01	1.87E+01	3.21E+03
25.4	7.70E+04	-6.06E+01	-2.65E+04	-6.74E-01	1.40E+01	2.41E+03

Table A-2 continued

6 Flutes						
Diameter	**C_0**	**C_1**	**C_2**	**C_3**	**C_4**	**C_5**
6.35	3.12E+05	-2.82E+02	-1.07E+05	-2.98E+00	6.42E+01	9.66E+03
9.53	2.08E+05	-1.89E+02	-7.11E+04	-2.00E+00	4.32E+01	6.44E+03
12.7	1.56E+05	-1.42E+02	-5.33E+04	-1.51E+00	3.24E+01	4.83E+03
15.9	1.25E+05	-1.14E+02	-4.27E+04	-1.21E+00	2.60E+01	3.87E+03
19.05	1.04E+05	-9.47E+01	-3.56E+04	-1.01E+00	2.17E+01	3.22E+03
25.4	7.80E+04	-7.11E+01	-2.67E+04	-7.56E-01	1.62E+01	2.42E+03

7 Flutes						
Diameter	**C_0**	**C_1**	**C_2**	**C_3**	**C_4**	**C_5**
6.35	3.11E+05	-2.84E+02	-1.06E+05	-2.78E+00	6.34E+01	9.65E+03
9.53	2.07E+05	-1.89E+02	-7.10E+04	-1.89E+00	4.25E+01	6.44E+03
12.7	1.56E+05	-1.42E+02	-5.32E+04	-1.42E+00	3.19E+01	4.83E+03
15.9	1.24E+05	-1.14E+02	-4.26E+04	-1.14E+00	2.56E+01	3.86E+03
19.05	1.04E+05	-9.50E+01	-3.55E+04	-9.48E-01	2.13E+01	3.22E+03
25.4	7.78E+04	-7.11E+01	-2.66E+04	-7.16E-01	1.60E+01	2.41E+03

Table A-3. The coefficients corresponding to number of flutes and tool diameter to relate natural frequency and length to diameter ratio to determine the appropriate helix factor.

3 Flutes

Diameter	H_0	H_1	H_2	H_3	H_4	H_5
6.35	-2.10E+00	-3.58E-06	4.23E-01	-2.12E-11	1.22E-05	-2.07E-02
9.53	-2.10E+00	-5.37E-06	4.23E-01	-4.77E-11	1.83E-05	-2.07E-02
12.7	-2.10E+00	-7.16E-06	4.23E-01	-8.47E-11	2.44E-05	-2.07E-02
15.9	-2.10E+00	-8.95E-06	4.23E-01	-1.32E-10	3.04E-05	-2.07E-02
19.05	-2.10E+00	-1.07E-05	4.23E-01	-1.90E-10	3.65E-05	-2.07E-02
25.4	-2.10E+00	-1.43E-05	4.23E-01	-3.39E-10	4.87E-05	-2.07E-02

4 Flutes

Diameter	H_0	H_1	H_2	H_3	H_4	H_5
6.35	-2.03E+00	-3.61E-06	3.91E-01	-1.63E-11	1.14E-05	-1.78E-02
9.53	-2.03E+00	-5.43E-06	3.91E-01	-3.67E-11	1.71E-05	-1.78E-02
12.7	-2.03E+00	-7.23E-06	3.91E-01	-6.51E-11	2.27E-05	-1.78E-02
15.9	-2.03E+00	-9.04E-06	3.91E-01	-1.02E-10	2.84E-05	-1.78E-02
19.05	-2.03E+00	-1.08E-05	3.91E-01	-1.47E-10	3.41E-05	-1.78E-02
25.4	-2.03E+00	-1.45E-05	3.91E-01	-2.61E-10	4.55E-05	-1.78E-02

5 Flutes

Diameter	H_0	H_1	H_2	H_3	H_4	H_5
6.35	-2.02E+00	-3.63E-06	3.85E-01	-1.55E-11	1.12E-05	-1.72E-02
9.53	-2.02E+00	-5.44E-06	3.85E-01	-3.50E-11	1.69E-05	-1.72E-02
12.7	-2.02E+00	-7.25E-06	3.85E-01	-6.22E-11	2.25E-05	-1.72E-02
15.9	-2.02E+00	-9.07E-06	3.85E-01	-9.71E-11	2.81E-05	-1.72E-02
19.05	-2.02E+00	-1.09E-05	3.85E-01	-1.40E-10	3.37E-05	-1.72E-02
25.4	-2.02E+00	-1.45E-05	3.85E-01	-2.49E-10	4.50E-05	-1.73E-02

6 Flutes

Diameter	H_0	H_1	H_2	H_3	H_4	H_5
6.35	-1.99E+00	-3.65E-06	3.73E-01	-1.41E-11	1.10E-05	-1.61E-02
9.53	-1.99E+00	-5.48E-06	3.73E-01	-3.17E-11	1.65E-05	-1.61E-02
12.7	-1.99E+00	-7.30E-06	3.73E-01	-5.64E-11	2.20E-05	-1.61E-02
15.9	-1.99E+00	-9.14E-06	3.73E-01	-8.80E-11	2.75E-05	-1.61E-02
19.05	-1.99E+00	-1.09E-05	3.73E-01	-1.27E-10	3.30E-05	-1.61E-02
25.4	-1.99E+00	-1.46E-05	3.73E-01	-2.26E-10	4.39E-05	-1.61E-02

Table A-4 continued

7 Flutes						
Diameter	**H_0**	**H_1**	**H_2**	**H_3**	**H_4**	**H_5**
6.35	-2.00E+00	-3.65E-06	3.75E-01	-1.44E-11	1.10E-05	-1.63E-02
9.53	-2.00E+00	-5.47E-06	3.75E-01	-3.23E-11	1.65E-05	-1.63E-02
12.7	-2.00E+00	-7.29E-06	3.75E-01	-5.74E-11	2.21E-05	-1.63E-02
15.9	-2.00E+00	-9.12E-06	3.75E-01	-8.97E-11	2.76E-05	-1.63E-02
19.05	-2.00E+00	-1.09E-05	3.75E-01	-1.29E-10	3.31E-05	-1.63E-02
25.4	-2.00E+00	-1.46E-05	3.75E-01	-2.30E-10	4.41E-05	-1.63E-02

VITA

Emma Betters received her BS in Mechanical Engineering from the University of Florida (UF) in 2017. During her undergraduate studies, she taught in the UF Design and Manufacturing Laboratory. Continuing her manufacturing education, she began her graduate studies in the Machine Tool Research Center (MTRC) at the University of North Carolina at Charlotte in 2018. In 2019, she relocated with advisor Dr. Tony Schmitz to the University of Tennessee, Knoxville (UTK) where she received her MS in 2022.

Emma began her role as an R&D Assistant Staff Member in the Intelligent Machine Tools Group at the Manufacturing Demonstration Facility at Oak Ridge National Laboratory (ORNL) in the fall of 2019. Her research interests are in machining dynamics, machine tool design, and manufacturing workforce development. Her work at UTK and ORNL has included: designing, constructing, and demonstrating a 3-axis CNC milling machine leveraging an additively manufactured mold and concrete filled composite base structure to illustrate alternatives to imported castings; manufacturing a device to electrostatically charge N95 material in support of COVID-19 PPE production efforts; modeling to predict the tool tip vibration response for the selection of stable machining conditions; and delivering on-machine instruction for America's Cutting Edge in-person CNC machining training.

Emma's professional recognitions include: 2023 SME 30 under 30, 2022 UT-Battelle Special Event Award, 2020 UT-Battelle Technology Transfer Award and 2020 UT-Battelle Director's Award for the rapid development and deployment of melt blowing and charging technology to enable domestic production of N95 media, and a 2019 ASPE Student Scholarship Award.